WITHOUT ENHANCEMENT

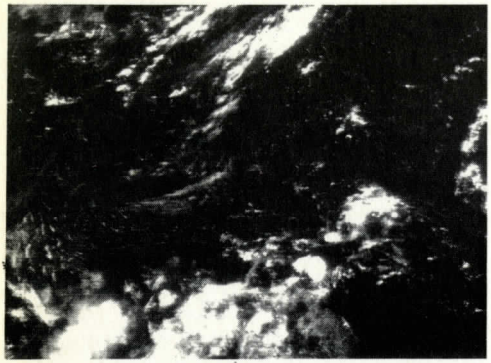

LOW-LEVEL ENHANCEMENT

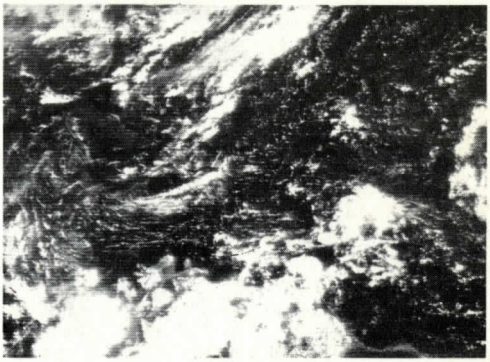

WITHOUT ENHANCEMENT

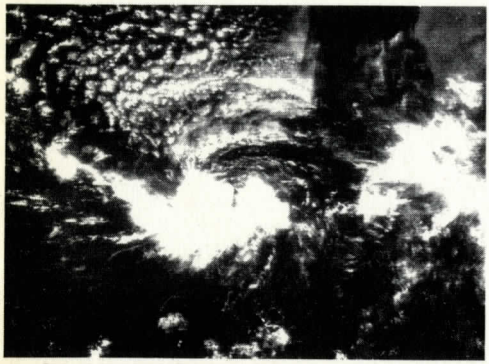

HIGH-LEVEL ENHANCEMENT

UW-Madison.
SSEC Publication No.69.11.S1.

Studies in Atmospheric Energetics Based on Aerospace Probings

Annual Report-1968

Space Science and Engineering Center
The University of Wisconsin

NOVEMBER, 1969

COVER PHOTOGRAPH

ATS-III spin scan camera data were recorded during BOMEX with increased frequency of observation on analog magnetic tape. The Space Science and Engineering Center has the capability of reproducing these analog tape data in photographic form through a precision display (facsimile) system. The cover photos indicate two means of enhancing portions of the brightness range of these pictures in order to emphasize certain cloud features.

The cover photos were obtained on July 26, 1969 at 1351 GMT. The top photos show the western Atlantic Ocean and Caribbean Sea. Cuba is visible in the upper left portion of the picture. The bottom photos show a tropical disturbance in the central Atlantic Ocean. Enhancement of the high brightness values tends to delineate the deep convective cells in the disturbance.

Space Science and Engineering Center
The University of Wisconsin
Madison, Wisconsin

STUDIES IN ATMOSPHERIC ENERGETICS BASED ON AEROSPACE PROBINGS

Annual Report on
ESSA Grant
E-230-68

1968

The research reported in this document has been supported by the National Environmental Satellite Center of the Environmental Science Services Administration.

November 1969
300-353

PRINCIPAL INVESTIGATOR

Verner E. Suomi

CONTRIBUTORS

J. Bennett
S. Cox
K. Hanson
A. Hasler
S. Kaniel
O. Karst
J. Kornfield
D. Martin
E. Remsberg
B. Schkoller
R. Schlesinger
T. Schwalenberg
U. Shafrir
D. Sikdar
V. Suomi
T. Vonder Haar
J. Weinman
J. Young

The University of Wisconsin

CONTENTS

Scanner's note:

This page is blank.

PREFACE

This report includes a series of papers which describe the use of Spin Scan Camera data in a quantitative way. The paper by Dr. Sikdar is perhaps the most outstanding example of what we can gain by treating images quantitatively. A second group of papers deals with the theoretical formulation of some of the phenomena which have been observed with the geostationary camera.

Finally, one paper is included which describes a technique and the hardware needed to accomplish the tasks. We are learning that techniques and devices are now setting the limit on what can be done in a quantitative way with the ATS images. Hopefully, our next report will include more progress in this important area.

It is a pleasure for me to acknowledge the many contributions of my associates. They are the individuals who really make this report possible.

Verner E. Suomi
Principal Investigator

Scanner's note:

This page is blank.

AN OBJECTIVE TECHNIQUE OF EVALUATING MESOSCALE CONVECTIVE HEAT TRANSPORT IN THE TROPICS FROM GEOSYNCHRONOUS SATELLITE CLOUD PHOTOGRAPHS

D. Sikdar and V. Suomi

ABSTRACT

Riehl and Malkus (1958) attempted to explain counter gradient heat transfer to the tropical troposphere by assuming the presence of selective buoyancy in the tropical convection regime. In the regime of selective buoyancy, cirrus outflow commonly occurs.

This paper aims at developing an objective technique for estimating the mass and energy exchange in convection systems corresponding to congestus and cumulonimbus intensities. This technique involves measuring the area change of the cirrus outflow on a sequence of satellite cloud photographs obtained at geostationary altitude. The data clearly show that: (1) The technique is able to isolate vigorous and moderate convection regimes on the ATS-I and ATS-III satellite cloud photographs; and (2) Our model estimates of mass and energy are consistent with ground-based measurements such as those of Braham (1952) and Brown (1967). Thus it is concluded that the geostationary satellite cloud photographs can be used to estimate convective mass and heat transport over the tropics.

INTRODUCTION

The net solar energy received by the earth-atmosphere complex is stored primarily in the upper layers of the tropical oceans. Heat gain in the lower latitudes and heat loss in the polar region are balanced by an energy flux from the tropics. This energy flux upward from the tropical oceans is accomplished by tropical convection systems on the meso and synoptic scales. Recent satellite pictures have shown that the tropical cloud systems over several hundred miles diameter form and dissipate often within a day or two.

The most important factor involved in the investigation of convective clouds in the tropics is the released latent heat, which is the major source of heat to the atmosphere. So far, due to lack of adequate conventional meteorological stations over the tropical oceans, very little is known about the magnitudes of these heat sources as a function of time. Convective cloud systems interact with large-scale circulations through the redistribution of heat sources and sinks. The primary objective of present-day meteorologists is to understand these interactions and to infer the physical processes involved in the meso-scale phenomena from the measuremements on the large-scale systems. So, in order to accomplish this goal, one needs to know the cloud population and the scales of convection with time.

ATS-I and ATS-III satellite cloud photographs are ideally suited to yield much information on cloud population and changes in cloudiness with time. The main purpose of this paper is to show that, subject to some reasonable assumptions, one can, indeed, estimate the heat sources from these time-lapse cloud photographs over the tropics, at various space and time scales, and can classify the convection (i.e., strong, moderate, or weak) accordingly.

CONVECTION MODELS IN THE TROPICS

In the tropics, convection systems can be classified into two broad classes: (1) shallow convection and (2) penetrative convection. Over the tropical oceans, shallow convection is associated with cumulus clouds whose tops do not penetrate the tropical inversion layer, while penetrative convection extends to the upper troposphere to at least 400 mb. As pointed out by Riehl and Malkus (1958), this penetrative convection may be the prime mechanism in the vertical transport of heat.

From an analysis of penetrative towers in Hurricane Daisy, Malkus (1960) concluded that penetrative towers of reasonable diameter, buoyancy, and entrainment rate readily reach the tropopause. In Hurricane Daisy all towers with initial diameters of 4 to 6 km reached 200 mb or higher. Based on Levine's (1959) vortex model, Malkus has further shown from theoretical considerations that an entrainment rate, $\frac{1}{M}\left(\frac{dM}{dz}\right)$, (where M is the mass entrainment), after Stommel (1947), of less than 0.1×10^{-5} cm^{-1} leads to insignificant dilution of clouds under saturation conditions. In a cloud element of thunderstorm size the entrainment rate is $0.05 \times 10^{-5} - 1.0 \times 10^{-5}$ cm^{-1}. One, therefore, concludes that the convective towers reaching deep into the upper troposphere in the tropics remain undiluted or nearly so. The clouds investigated in this research are much greater than 10 kms in diameter.

The convection model we propose in this paper is an open flow system consisting of three sections of flow: (1) inflow at the subcloud layer, (2) vertical motion in the cloud cross-section, and (3) outflow near the tropopause. The

assumption of a steady-state condition simplifies our flow model. A schematic diagram showing the flow systems is presented in Figure 1.

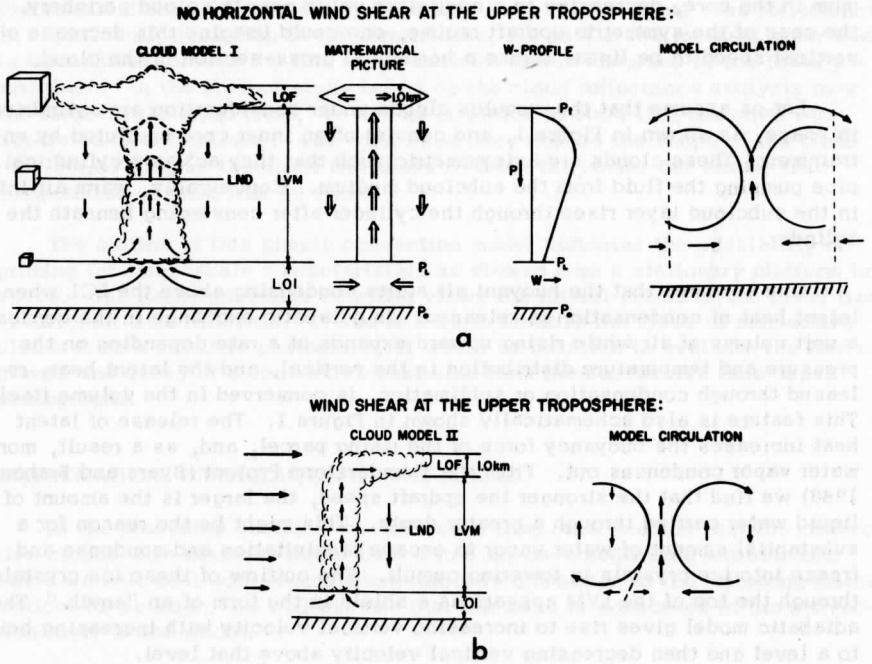

Figure 1. Schematic diagram for the proposed convection model. (LND = level of nondivergence; P = pressure; W = vertical velocity.)

The layer of inflow (LOI), as shown in Figure 1, is the layer between the sea surface and the lifting condensation level (LCL). In this layer, warm moisture-laden air is drawn into the cloud region because of the locally produced thermal convergence in the surface layer. This layer also contains a part of the down-draft descending below the LCL in the mature and dissipating stage of the convection. The thermal stratification and the moisture distribution in the warm air inflow virtually determine the degree of evaporation in the cold down-draft that enhances the sensible heat transfer from the subcloud layer. This process indirectly accelerates the upward motion by buoyancy readjustment in the subcloud layer, thereby transporting greater amount of mass, momentum, and heat upward.

The second layer is the convection layer (LVM) extending from the LCL to the "throat" (Bates, 1961) of the cloud near the cloud top where the buoyancy force is zero or slightly negative. In this layer the vertical motion is a maximum in the core, decreasing to a negligible value near the cloud periphery. In the case of the symmetric updraft regime, one could imagine this decrease of vertical speed to be linear across a horizontal cross-section of the cloud.

Let us assume that the cumulus clouds under consideration are cylindrical in shape, as shown in Figure 1, and consist of an inner core undiluted by entrainment. These clouds are axisymmetric such that they act as a cylindrical pipe pumping the fluid from the subcloud medium. Conceivably, warm air inflow in the subcloud layer rises through the cylinder after converging beneath the cylinder.

One assumes that the buoyant air starts condensing above the LCL when the latent heat of condensation is released. In adiabatic exchange in the vertical, a unit volume of air while rising upward expands at a rate depending on the pressure and temperature distribution in the vertical, and the latent heat, released through condensation or sublimation, is conserved in the volume itself. This feature is also schematically shown in Figure 1. The release of latent heat increases the buoyancy force of the rising parcel, and, as a result, more water vapor condenses out. From the Thunderstorm Project (Byers and Braham, 1949) we find that the stronger the updraft speed, the larger is the amount of liquid water carried through a greater depth. This might be the reason for a substantial amount of water vapor to escape precipitation and condense and freeze into ice crystals in towering cumuli. The outflow of these ice crystals through the top of the LVM appears as a shield in the form of an "anvil." The adiabatic model gives rise to increasing vertical velocity with increasing height to a level and then decreasing vertical velocity above that level.

The layer of outflow (LOF) extends from the throat of the convective tower to the base of the tropopause. It is assumed that faster rising cloud particles lose their momentum when they arrive near the throat of the tower and then come under the influence of local wind. This damping effect of the stable layer below the tropopause on the vertical motion field has long been recognized. The situation is similar to a jet of air particles impinging on a flat plate. The air reaching to the top of the storm comprises the source for divergence in the cloud plume at the top.

Figure 1a shows the model outflow in the absence of wind shear in the upper troposphere while Figure 1b presents the outflow in the presence of pronounced wind shear in the upper troposphere. The model circulations in these two cases are also presented.

In the former case, because of the high concentration of water droplets and ice crystals all through the cloud depth, the reflectance at the cloud top is expected to be very strong. In the latter case the cirrus shield is blown off from the cumulonimbus tower and is carried into a dry environment. The reflectance is significantly less than in the former case, for part of the incident solar energy is transmitted through the thin cloud material and is absorbed in the lower atmosphere. In the present study based on the cloud reflectance analysis over the large-scale cloud field, we had no occasion to show that the anvil was separated from the tower. The wind shear may change the shape of the cloud top, but,as long as the cloud thickness remains the same, our energy flux computation scheme will be valid.

The outline of this simple convection model indicates the possibility of probing into mesoscale characteristics as viewed from a stationary platform in space. The geosynchronous satellite views the lateral extent of the cloud field at different time intervals. If one is able to identify the types of convective clouds from a satellite photograph, it would be possible to evaluate the rate of growth and decay of a convective ensemble from the successive time-lapse photographs.

MATHEMATICAL FORMULATION OF THE MODEL

In the preceding section, we have seen from other studies that the convective clouds with diameter larger than 6 to 8 km have negligible entrainment. Since we will deal with clouds much larger in dimension in the following mathematical formulation, we will assume that the mass is conserved in the convection layer of the model.

Volume Flux

Using the equation of state, $PV = R^*T$, where R^* is the universal gas constant,and using the assumption that mass is conserved, one can relate the volume V_t of an air parcel at the level of divergence near the cloud top to its volume V_L at the subcloud layer, by

$$V_t = \left(\frac{P_L T_t}{P_t T_L} \right) V_L \qquad (1)$$

where suffixes t and L stand for the base of the outflow layer and top of the inflow layer, respectively, and T_t and T_L are the corresponding virtual temperatures.

In case of ideal flow through the cylinder, P_t represents the static pressure at the top and should be small. In the model, P_t is defined as the lowest pressure to which a buoyant cloud will mainly penetrate from the surface layer. In most of the tropical soundings investigated in this work from parcel consideration, P_t has been found to be close to 150 mb. Updraft air reaches an equilibrium at P_t and then spreads out in a layer probably not more than 1 km thick (Ludlum, 1966, and Borovikov, 1963). This flow model presumes that the cirrus outflow at the top of the cloud tower remains confined to a layer of thickness 1.0 km.

Taking the mean value for P_t, P_L, T_t, and T_L, the volume flux $\frac{dV_t}{dt}$ at the layer of outflow may be related to the volume flux at the layer of inflow, by the equation

$$\frac{dV_t}{dt} = \left(\frac{P_L T_t}{P_t T_L}\right) \frac{dV_L}{dt}$$

Writing $V_L = \frac{M_L}{\rho_L}$, we get

$$\frac{dV_t}{dt} = \left(\frac{P_L T_t}{P_t T_L}\right) \frac{d}{dt}\left(\frac{M_L}{\rho_L}\right) \tag{2}$$

where ρ_L is the density of air at the subcloud layer. For a steady flow at the subcloud layer, ρ_L may be assumed independent of time, in which case equation (2) may be written as

$$\frac{dV_t}{dt} = \left(\frac{P_L T_t}{P_t T_L \rho_L}\right) \frac{dM_L}{dt} \tag{3}$$

In equation (3), P_t, P_L, and T_t are evaluated from the mean upper air sounding in the vicinity of the cloud ensemble under investigation. The term dV_t/dt, however, is computed in an indirect method from the ATS-I satellite cloud photographs.

Mass Flux

The amount of mass transported vertically into the layer of outflow through the convective towers in time Δt is given by $\frac{\partial}{\partial z}(\rho w)\Delta t$. In this model, we have assumed a steady-state flow. In the light of the Boussinesq approximation in thermal convection (see Spiegel and Veronis, 1960), one can write the equation of continuity for the cloud particle at the LOF as follows:

$$\frac{\partial u_c}{\partial x} + \frac{\partial v_c}{\partial y} = -\frac{\partial w_c}{\partial c} \tag{4}$$

where subscript c refers to cloud particles. The quantity $\frac{\partial u_c}{\partial x} + \frac{\partial v_c}{\partial y} = \nabla_H \cdot \vec{V}_c$ can be related to increase or decrease of the area encompassed by the cloud particles and does not necessarily reflect on the actual horizontal flow divergence $\nabla_H \cdot \vec{V}$.[1]

Let us consider a cloud volume $V = dx \cdot dy \cdot dz$ at time t_o. After a small finite time Δt, the cloud particles bounding the area will have moved and the new volume will be

$$\left[dx + \left(\frac{\partial u_c}{\partial x}\right) dx\Delta t\right]\left[dy + \left(\frac{\partial v_c}{\partial y}\right) dy\Delta t\right] dz$$

$$= dx \cdot dy \cdot dz \left[1 + \left(\frac{\partial u_c}{\partial x} + \frac{\partial v_c}{\partial y}\right)\Delta t + \left(\frac{\partial u_c}{\partial x} \cdot \frac{\partial v_c}{\partial y}\right)\Delta t^2\right] \tag{5}$$

since dz is assumed constant.

The change in cloud volume is

$$\Delta V = dx \cdot dy \cdot dz \left[\left(\frac{\partial u_c}{\partial x} + \frac{\partial v_c}{\partial y}\right) t + \left(\frac{\partial u_c}{\partial x} \cdot \frac{\partial v_c}{\partial y}\right)\Delta t^2\right]$$

$$= V\left[\nabla_H \cdot \vec{V}_c + \frac{\partial u_c}{\partial x} \cdot \frac{\partial v_c}{\partial y}(\Delta t)\right]\Delta t \tag{6}$$

since $V = dx \cdot dy \cdot dz$,

$$\nabla_H \cdot \vec{V}_c = \frac{1}{V}\left(\frac{dV}{dt}\right) \tag{7}$$

in the limit Δt approaching zero.

---

[1] This cloud divergence can be considered analogous to the horizontal spread of smoke particles in the atmosphere from a smoke chimney which occurs even in the absence of flow divergence, such as in a constant flow field.

This equation means that a fractional change in volume flux of cloud particles around a point is equal to the radial divergence. Assuming dz is a constant, equation (7) may be written as

$$\nabla_H \cdot \vec{V}_c = \frac{1}{A_c}\left(\frac{dA_c}{dt}\right) \tag{8}$$

where $A_c = dx \cdot dy = \pi r^2$, and r is the equivalent radius of the cirrus shield. From equation (8), we get

$$\nabla_H \cdot \vec{V}_c = \frac{2}{r}\left(\frac{dr}{dt}\right) \tag{9}$$

Computation of Inflow and Outflow Rate

The anvil may be regarded as resulting from a circular disk expanding uniformly normal to its edge. The outflow rate from equation (7) in the layer of 1.0 km thickness (Ludlum, 1966; Borovikov, 1963; and Anderson, 1960) is given by

$$\frac{dV_t}{dt} = [(\pi r^2) \cdot dz \cdot (\nabla_H \cdot \vec{V}_c)]\,cm^3/sec \tag{10}$$

where dz = 1.0 km.

Combining equations (3) and (10), one obtains the mass inflow rate at the base of the cloud tower:

$$\frac{dM_L}{dt} = \frac{P_t T_L \rho_L}{P_L T_t}\,[(\pi r^2) \cdot dz \cdot (\nabla_H \cdot \vec{V}_c)] \tag{11}$$

where $\rho_L = 1.1 \times 10^{-3}$ g/cm^3.

The term $(\pi r^2)(\nabla_H \cdot \vec{V}_c)$ [or $\pi r^2 \frac{1}{A_c}\left(\frac{dA_c}{dt}\right)$] in equation (11) is computed from the measurements on the successive ATS-I satellite cloud photographs.

Computation of Latent Heat Flux

In this model it is assumed that the equivalent potential temperature at the LCL is constant for a saturated ascent and that all water vapor passes into the condensation phase in the course of its ascent through the cloud core. From the upper air sounding data, one can estimate the amount of moisture likely to

condense out in saturated adiabatic ascent. Let this be $W = (W_L - W_t)g/kg$. The latent heat flux is

$$E_c = L \cdot \Delta W \left(\frac{dM_L}{dt} \right) \text{ cal/sec} \qquad (12)$$

where $L = 597$ cal/gm at 0° C.

Compensating Motion in the Cloud Environment

The law of mass continuity requires that the mass lifted up to the upper troposphere through the convective cores should be compensated by the downward motions somewhere in the atmosphere. One can conceive of such motions existing in the near and far regions of the penetrative convection zones. The far region compensating motions merge with the sinking motion associated with the permanent high-pressure regimes while the near region compensating motion exists in the vicinity of the cirrus outflow.

The flow in deep convection has been shown schematically in Figure 1a and b. In these diagrams the arms of the descending circulation have been left open to show that in the large-scale flow field the descent continues in other systems and that there is no boundary on that side (see Green, Ludlum, and McIlveen, 1966). The re-entry of the far region descending air in the surface layer of the same latitude takes a period of up to 20 days or more. We will assume that most of the return flow occurs at a distance from the cloud.

It is probable that the near region compensating motion would evaporate some of the ice crystals in the cirrus shield and, as such, the area of the cirrus shield as viewed by a geosynchronous satellite would be less than expected. However, Darkow (1963) has shown that these ice crystals in the tropical upper troposphere have much longer life time than that of a convective cloud. In view of his findinigs it is presumed that there will be no significant error in the mass and heat flux estimates due to evaporation of ice crystals.

DATA SOURCE AND THE TECHNIQUE OF ANALYSIS

The grid matrix of the ATS-I cloud photographs consists of 8196 digital elements and 2018 scan lines. On this grid, we have information on brightness ranging from 0 to 256 digital numbers. The advantage of the digital display is that the outlines of small-scale convection are difficult to draw on the satellite photographs, but they can be distinguished very well on the digital display. The large-scale convective systems, however, can be analyzed from the enlarged photograph itself.

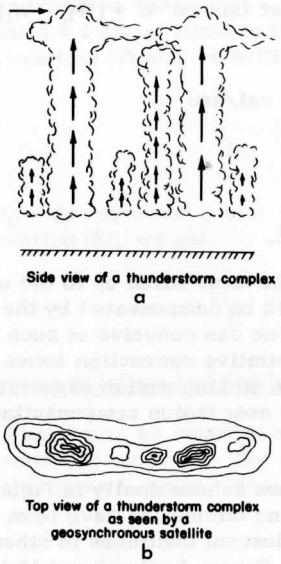

Figure 2. Schematic diagram of a convective complex as viewed by a geosynchronous satellite.

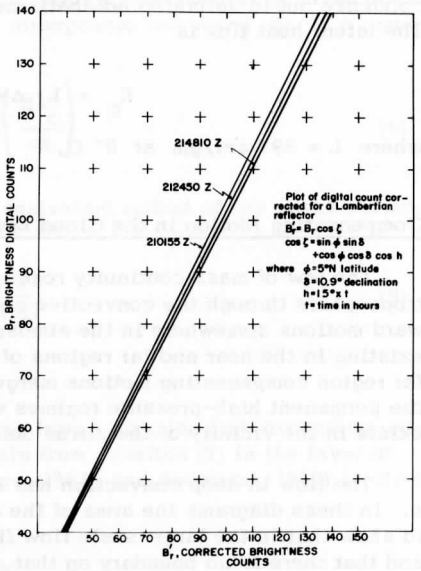

Figure 3. Plot of corrected brightness values at different solar zenith angles at the subsatellite point.

Figure 2 presents a schematic diagram showing the nature of the brightness distribution as would be expected of a deep convection viewed by a geosynchronous satellite. A cloud target would appear brighter when there is a high concentration of water droplets, and also, when the cloud top is high, there is a little attenuating atmosphere above it. Also, the brightness of a cloud top depends on the solar zenith angle. A cloud surface is not a Lambertian reflector, especially at large zenith angle of the sun (Bartman, 1967). However, for small zenith angle (+30° to -30°) of the sun, the top surface of a deep cloud may closely behave as a Lambertian reflector. Figure 3 is a plot of a set of brightness values as a function of time at 5° N, declination at 10.9° . The brightness value changes by only a few percent in the 2-hour period around local noon.

Our primary objective is to measure the cloud area change in large clouds on the successive ATS-I digital displays. The cloud area depends on the choice of the brightness level but is independent of the brightness gradient. Therefore,

one must be careful in selecting the brightness cut-off level and the period of observation. In order to avoid correcting brightness values, we have chosen satellite pictures close to local noon at the subsatellite point.

The digital information needed is cropped from the original digital tape using the B5500 computer and then displayed in a desired grid through the CDC 3600. Since the signal intensity varies from target to target, there is present a wide range of variations in the digital records. The presence or absence of a cloud over the sea surface can be recognized from the variations in the digital count. The calm sea surface will have maximum absorption of solar radiation in a cloudless atmosphere, and its albedo would be low enough to be distinguished from the cloud surface. A plot of digital signal across the cloud complex is helpful at this point (see Figure 4). By selecting proper digital levels in the cropped records, we can easily isolate the cloud area. Since the luminance of a particular cloud sample depends on the cloud properties such as droplet size spectrum, liquid water content, etc., the study of the brightness range and its gradient in the cloud population should reflect on these characteristics at least qualitatively. Here we assume that clouds of the same type have approximately the same material characteristics at the top surface.

Figure 4 shows the nature of the signal level across a convective ensemble. It is clear from this diagram that the signals higher than 75 digital counts probably correspond to the regions of deeper clouds in this convective ensemble. In this paper we will present two case studies, one showing the penetrative convection in a small-scale cloud complex (upper bordered region in Figure 5) and the other, convection in a large-scale complex (lower bordered region in Figure 5).

We have selected the day April 19, 1967, when small-scale cumulus activities are seen in the vicinity of the Line Islands (located in the upper bordered region in Figure 5). The mesoscale convective activities on the northwest sector of Palmyra (5° 53'N, 162° 05'W) are supported by aircraft reports as well as radar observations close to the period of satellite observation. Figure 6 presents the enlargement of the mesoscale regime, while Figure 7 refers to that of the large-scale cloud field on Figure 5 (not to scale). Figures 8 and 9 show the digital displays at 210155Z, 212450Z, and 214801Z corresponding to two regimes of convection as pointed out in Figure 5. Each rectangular grid box represents an area of 20 scan lines × 100 elements. The object of these presentations is to show the brightness contrast in these two convection regimes.

The areas of the clouds outlined by the digital number 50 in Figure 8 and by the digital count 75 in Figure 9 are measured by a planimeter. In the computation of the scale factors on these displays, the distances between the two scan lines and two elements have been taken at 2.3 nautical miles and 0.7 nautical miles, respectively. The first period in Table 1 refers to the time interval 210155Z - 212450Z, while the second period in Table 2 refers to 212450Z - 214801Z.

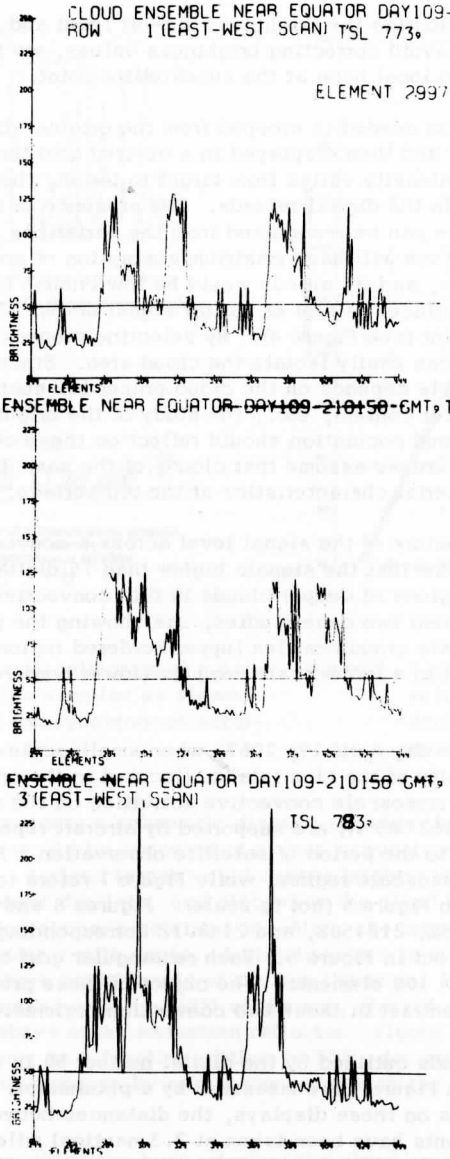

Figure 4. Plot of digital signal across a convective ensemble.

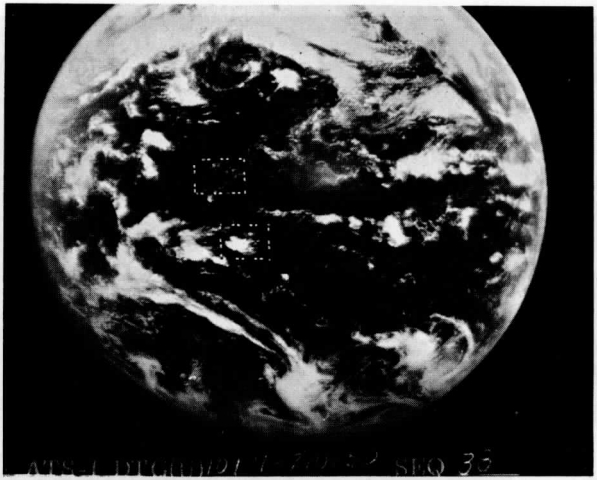

Figure 5. ATS-I satellite cloud photograph of April 19, 1967.

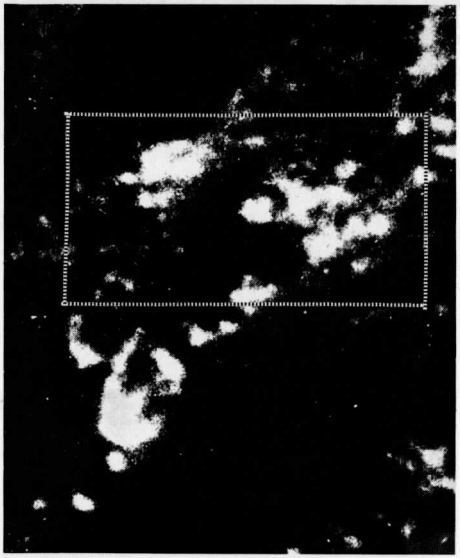

Figure 6. Enlargement of a section of cloud field around Palmyra (5°53'N, 162°02'W). (Not to scale.)

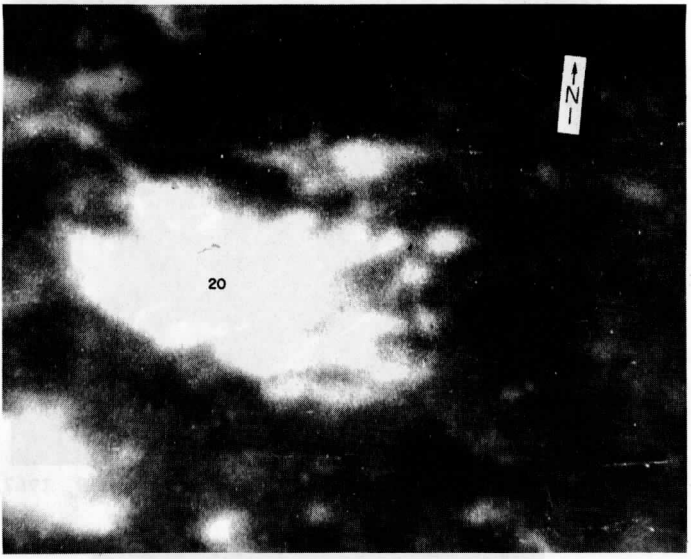

Figure 7. Enlargement of a section of cloud field at 10 °S on the ITCZ. (Not to scale.)

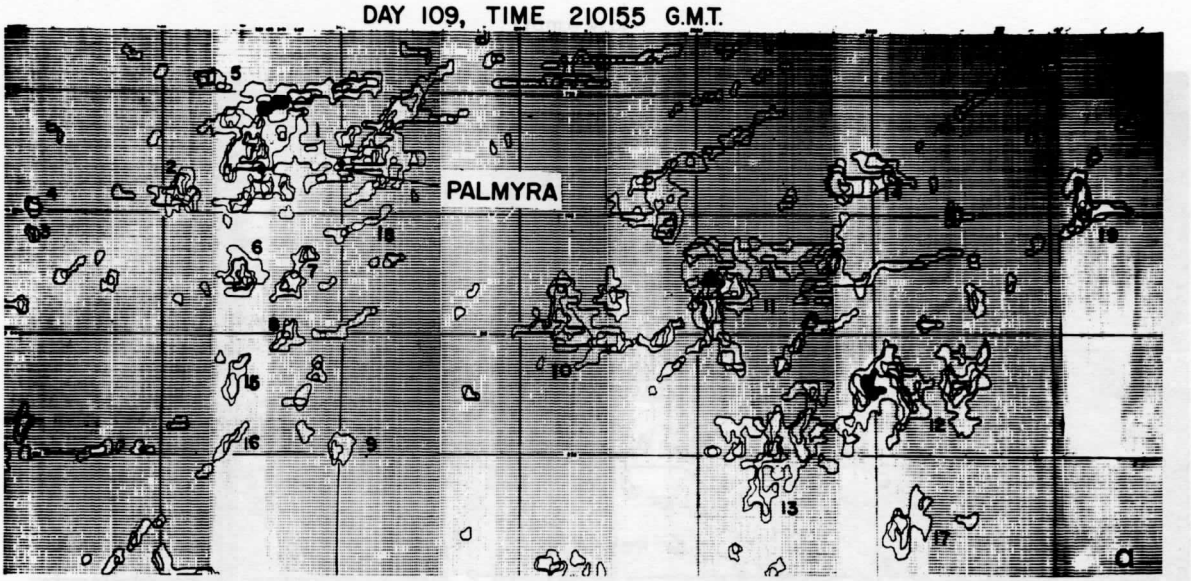

(a)

Figure 8. ATS digital displays corresponding to Figure 6. (Scale: Each small box = 20 lines × 100 elements.)

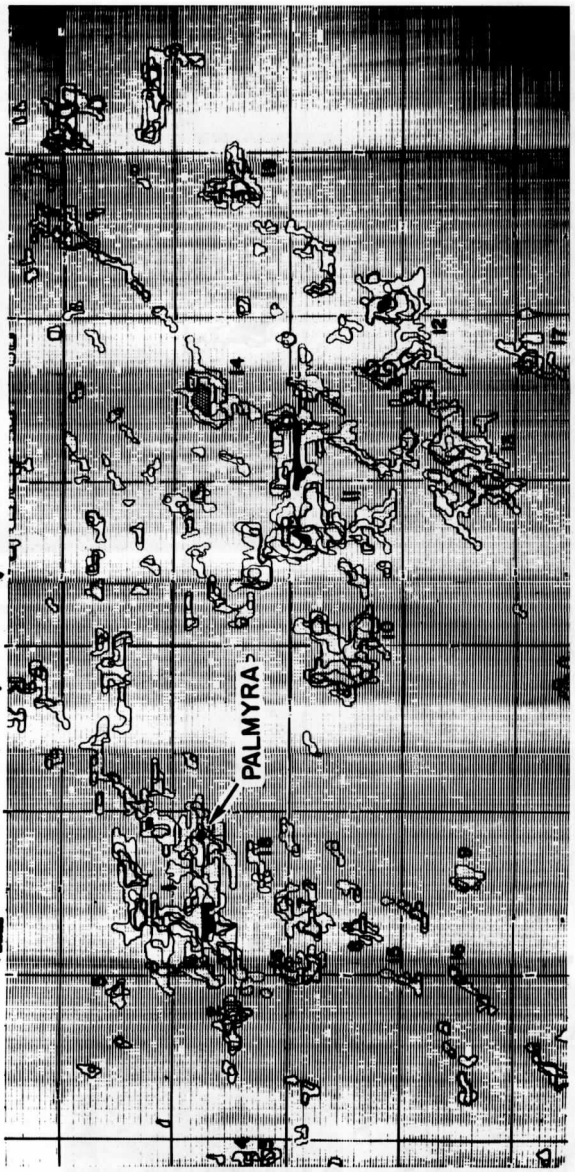

Figure 8(b)

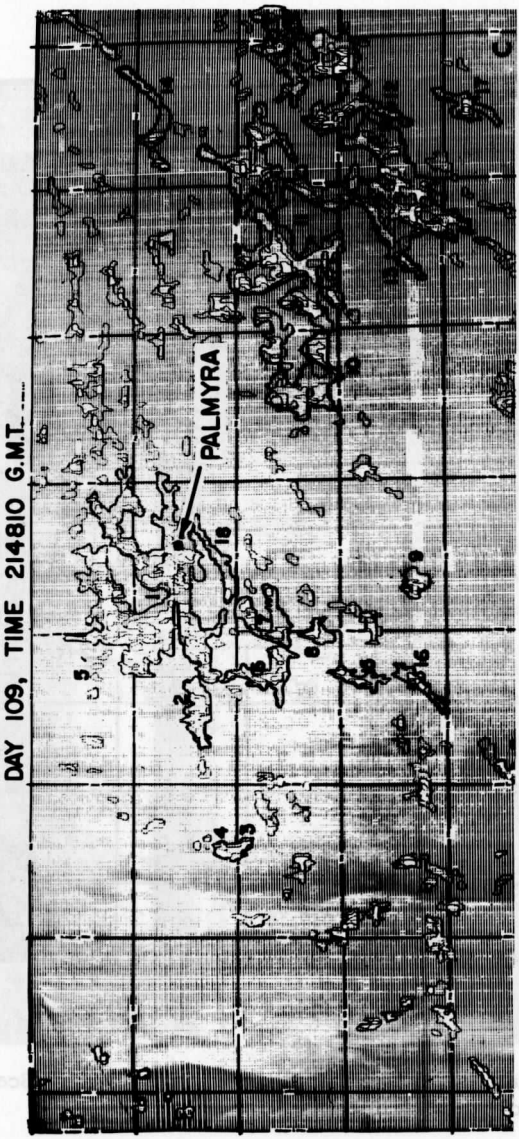

Figure 8(c)

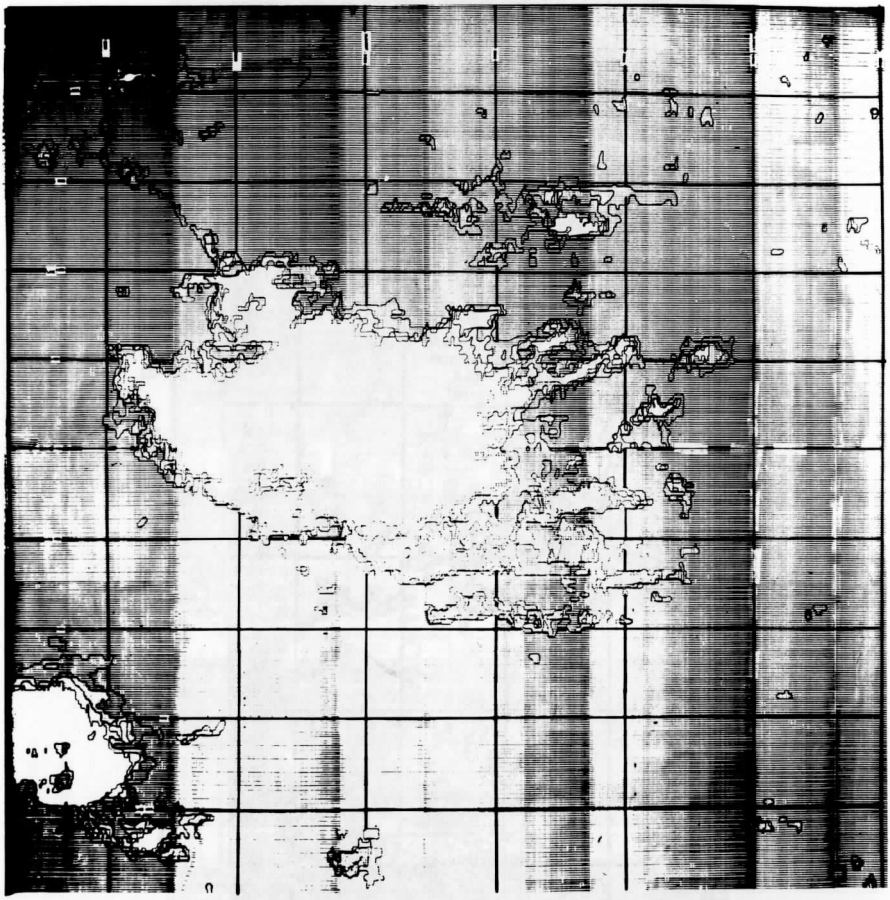

(a)

Figure 9. ATS digital displays corresponding to Figure 7. (Scale: Each small box equals 20 lines × 100 elements.)

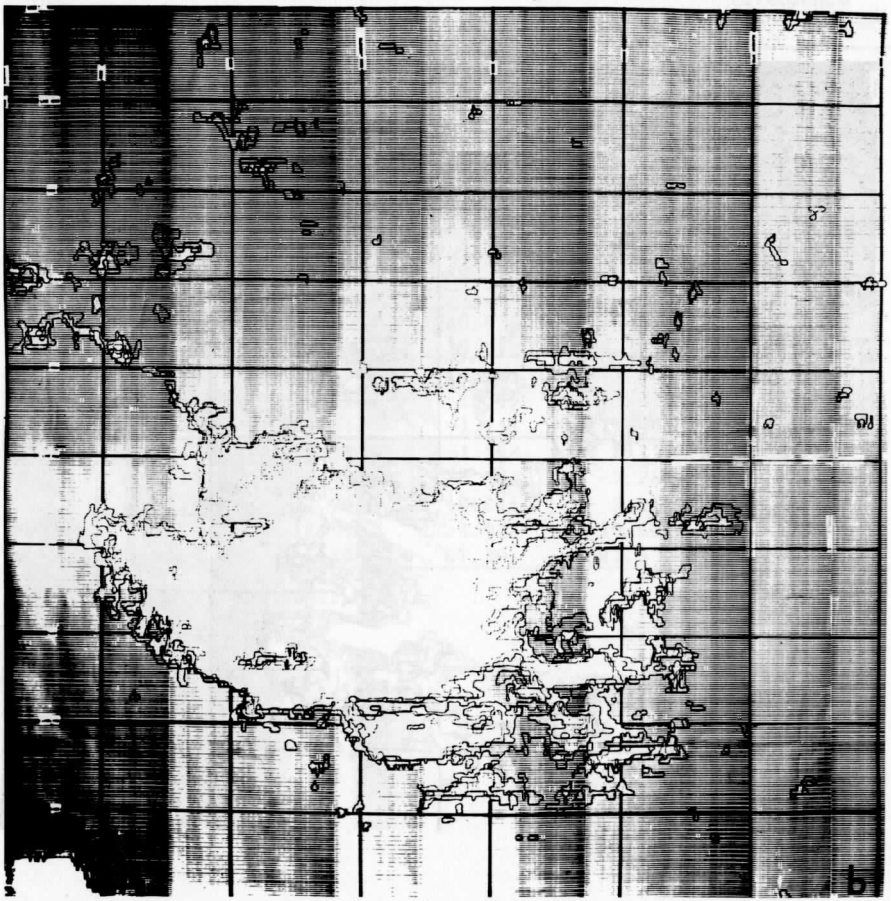

(b)

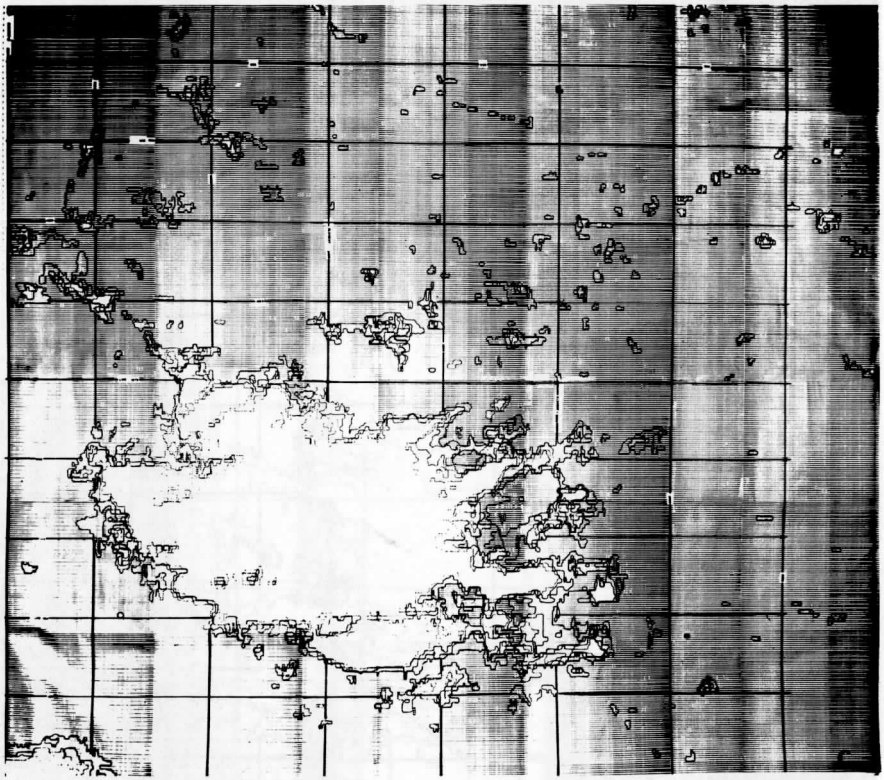

(c)

TABLE 1

Measurements on ATS-I Satellite Photographs
Day 109

Cloud Number	Area 1* (10^{12} cm^2)	Area 2** (10^{12} cm^2)	$A_2 - A_1$ (10^{12} cm^2)	Mean Area (10^{12} cm^2)	Cloud Divergence (10^{-4} per sec)
1	81.280	99.500	18.220	90.390	1.623
2	7.516	6.955	-0.561	7.236	-0.540
3	1.049	1.835	0.787	1.442	5.436
4	1.486	1.932	0.446	1.709	2.174
5	2.272	2.318	0.046	2.295	0.146
6	7.604	7.728	0.124	7.666	0.118
7	5.069	7.921	2.852	6.495	4.076
8	3.496	3.671	0.175	3.583	0.362
9	3.234	3.478	0.244	3.356	0.543
10	26.220	27.050	0.828	26.630	0.228
11	51.390	71.480	20.090	61.440	2.832
12-13	68.870	73.130	4.255	71.000	0.447
14	11.890	14.970	3.087	13.430	1.881
15	4.370	2.512	-1.858	3.441	-3.080
16	3.496	1.932	-1.564	2.714	-3.241
17	8.740	5.796	-2.944	7.268	-2.440
18	3.321	2.705	-0.616	3.013	1.343
19	9.614	11.590	1.978	10.600	1.490
20	637.8	725.10	87.30	681.5	0.991

*Refers to time 210155 GMT.

**Refers to time 212450 GMT.

TABLE 2

Measurements on ATS-I Satellite Photographs
Day 109

Cloud Number	Area 1* (10^{12} cm^2)	Area 2** (10^{12} cm^2)	$A_2 - A_1$ (10^{12} cm^2)	Mean Area (10^{12} cm^2)	Cloud Divergence (10^{-4} per sec)
1	99.500	107.300	7.753	103.400	0.564
2	6.955	11.490	4.536	9.223	4.725
3-4	3.767	3.830	0.063	3.799	0.121
5	2.318	2.298	-0.020	2.308	-0.062
6	7.728	9.576	1.848	8.652	1.732
7	7.921	9.097	1.176	8.509	1.075
8	3.671	3.830	0.160	3.751	0.315
9	3.478	3.926	0.449	3.702	0.934
10	27.050	32.560	5.510	29.800	1.476
11	71.480	84.270	12.780	77.880	1.294
12-13	73.130	98.630	25.510	85.880	2.527
14	14.970	12.450	-2.524	13.710	-1.221
15	2.512	4.213	1.702	3.363	4.909
16	1.932	4.788	2.856	3.360	10.710
17	5.796	6.129	0.333	5.962	0.416
18	2.705	6.320	3.615	4.512	9.680
19	11.590	11.490	-0.101	11.540	-0.063
20	725.10	760.60	35.50	742.9	0.354

*Refers to time 212450 GMT.

**Refers to time 214801 GMT.

INTERPRETATION OF ATS-I SATELLITE PHOTOGRAPHS

The first step in the interpretation of ATS-I satellite photographs is to identify the different cloud forms, their brightness values, pattern, structure, and size. The brightness factor plays an important role in the cloud interpretation.

Whitney (1963) points out certain identifying characteristics of the satellite-observed thunderstorm complexes, i. e., rounded, very bright appearance, large size, and frequent peripheral clear zones which help to isolate thunderstorm complexes from other cloud complexes.

In general, over the tropical oceans, penetrative convection is associated with cirrus plumes at its top. These cirrus plumes, when viewed by a geosynchronous satellite, represent anvil cloud material formed out of a thunderstorm complex and exhibit a pronounced brightness. The regions of maximum brightness in a cloud complex are considered to be the regions of deep convection, i. e., the zones of strong vertical motion. The zones of highest vertical motion in a cloud ensemble, in turn, relate the regions of maximum liquid water concentration (Byers and Braham, 1949), for it is in these zones that maximum amounts of water vapor pass into the condensed phase. The shallow convection, on the other hand, exhibits a poor brightness gradient. The key, however, is the growth of the cirrus anvil or plume. The expansion of the cirrus anvil absolutely identifies deep convection areas (see Figure 5). In Figure 8a, the strong brightness indicative of the cirrus shield at the top of the convection complex is distinctly noticeable against the low cloud background. In this picture, it is easily possible to outline the cirrus shield but difficult to isolate the zones of active convection in the complex,for the brightness gradient is not detected well by a human eye. However, it is possible to isolate them on the ATS-I digital displays. Once the satellite photographs are properly interpreted for the cirrus shield, it is possible to track the brightest cloud outlines on the two successive satellite pictures.

RESULTS

In the previous section we stated that the brightness gradient of a convective cloud plays an important role in deciding the character of convection associated with it. In this section we will use the Line Islands data (Zipser and Taylor, 1968) as the basis for a computation of heat and mass flux using our model and show that: (1) Our convection model is able to isolate vigorous and moderate-to-weak convective regimes on the ATS-1 satellite photographs; (2) Our values of mass and energy flux are consistent with ground-based estimates of Braham (1952) and Brown (1967); (3) A cloud complex is made of many individual cells; and (4) This measurement scheme is applicable to storms of moderate to high intensity.

One of the important purposes of the Line Islands experiments (Zipser and Taylor, 1968) was to correlate surface, ship, aircraft, and satellite observations. As a "cloud truth" we will discuss the observations in and around the vicinity of Palmyra (5° 53'N, 162°05'W), where we have surface radiosonde, radar, and aircraft observations as well as ATS-I satellite cloud pictures.

Thermodynamics of the Atmosphere over Palmyra on April 19, 1967

Figure 10 shows the mean upper air temperature and moisture sounding plotted in the Skew T diagram. The mean sounding is prepared from five soundings taken at 00, 06, 12, 1725, and 2000 GMT. The mean surface temperature is as high as 28.7° C, and the specific humidity at the surface is around 19 g/kg, becoming less than 0.1 g/kg at 200 mb. The LCL is at 950 mb, and the convective condensation level is only 10-15 mb higher.

From the radar photographs presented in Figure 11, it appears that there were more than 35 precipitation echoes present in the 100-mile radius around Palmyra (5° 53'N, 162°05'W). The position of Palmyra on the digital display could not be fixed precisely for want of navigational data relevant for mesoscale analysis. However, an approximate position has been indicated by a black dot on the digital displays. It is interesting to note from the radar photographs that there were as many as 20 precipitation echoes in cloud complex 1 (see Figure 8) in the first period. It is clear that where conventional observations show convective activity, the satellite photos show it also. The aircraft observations also indicated scattered cumulus congestus developing with tops above 6 to 7 km in the sector west of Palmyra close to the period of observations.

Figure 12 presents the mean heat content profile over Palmyra on April 19, 1967. Here the total heat content is defined as the sum of enthalpy (CpT), geopotential energy (gz), and the latent heat (Lq). This diagram shows the thermodynamic state of the atmosphere over Palmyra. The Q profile indicates two minima of magnitude, 78.3 cal/gm at 800 mb and 77.9 cal/gm at 600 mb. The level of first minima corresponds approximately to the level of trade inversion around 5° N. The level of second minima may be the highest level through which vertical mixing in the lower troposphere extends by eddy diffusion. The mechanism of eddy diffusion explains the heat and moisture transport from the boundary layer to the middle troposphere, but it fails to account for the counter-gradient heat transfer in the upper troposphere if the boundary layer is considered to be the primary heat source. Riehl and Malkus (1958) attempted to resolve this anomaly by assuming the existence of selective buoyancy mechanisms in the tropical convection regime. Cirrus outflow, which rarely occurs below 300 mb in the tropics, is evidence of this counter gradient heat transfer. Quantitative estimates of the heat transfer to the upper troposphere by this mechanism form the basic contribution of this paper.

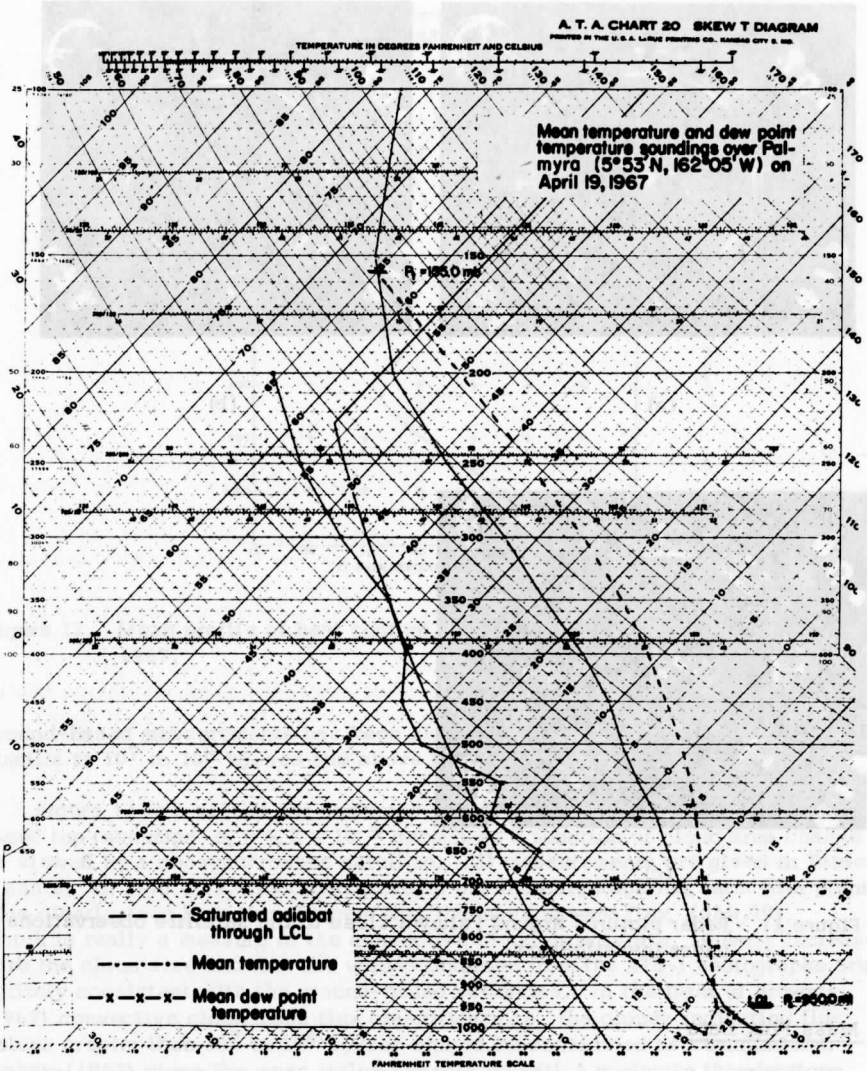

Figure 10. Mean upper air sounding over Palmyra on April 19, 1967.

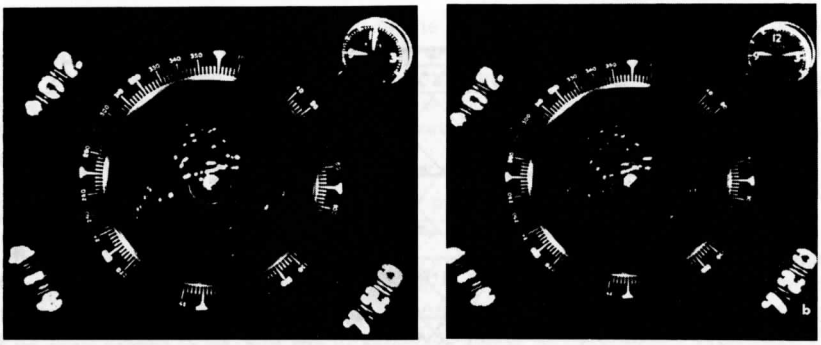

(a) (b)

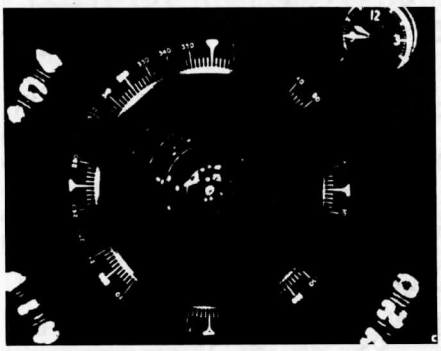

(c)

Figure 11. Radar pictures around Palmyra close to the satellite observations under investigation.

Mass Flux Data

Cloud physicists have observed that the growth rate of the convective cloud systems varies considerably from cumulus humilis to cumulonimbi. Brown (1967) has recently compiled all published data on convective cloud growth rates (Anderson, 1960, and Brown, 1966) and developed a power function to estimate the growth rate and available energy. The range of mass flux from

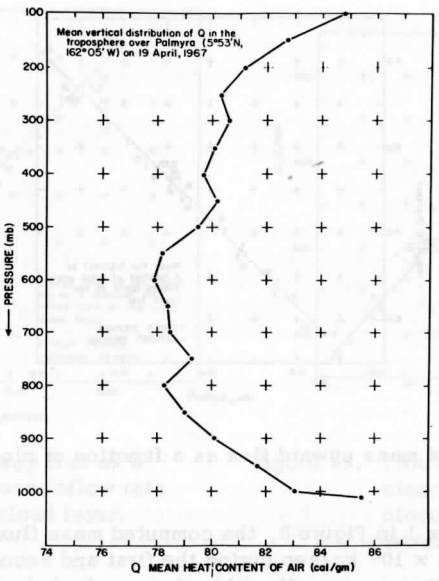

Figure 12. Mean profile of heat content of air (cal/gm) over Palmyra on April 19, 1967.

ground-based measurements has been shown to vary from 10^5 kg/sec for cumulus humilis to 10^7 to 10^8 kg/sec and above for cumulonimbus clouds.

Figure 13 is a plot of our computed values of mass upward fluxes at the cloud top (assumed $e_t = 0.2 \times 10^{-3}$ g/cm^3) as a function of cloud area change as viewed by a geosynchronous satellite. All measurements are given in Tables 1 and 2. In Figure 13, the cloud numbers are indicated against each data point. It is clearly seen from this diagram that the mass upward flux (dM_t/dt), which is really a measure of the convective cloud growth rate, linearly increases with the cloud size and that the values obtained from the ATS-I photographs are entirely consistent with the ground-based estimates. In the light of Brown's (1967) convective cloud mass flux classifications, the clouds indicating flux values greater than 10^7 to 10^8 kg/sec should be considered as cumulonimbi. Braham (1952) gives the mass influx associated with a moderate thunderstorm as 5.1×10^7 kg/sec between the levels 5000 to 10,000 ft. The mass flux range 10^6 to 10^8 kg/sec will refer to the category of cumulus congesti.

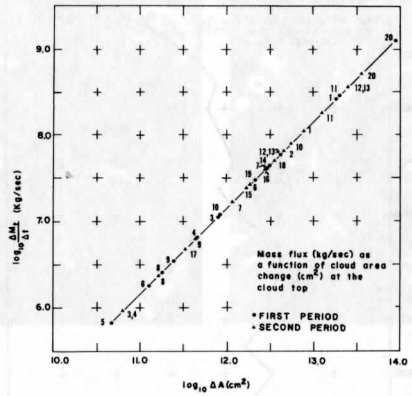

Figure 13. Plot of mass upward flux as a function of cloud area change.

In cloud complex 1 in Figure 8, the computed mass flux values are 3.57×10^8 kg/sec and 1.51×10^8 kg/sec during the first and second period, respectively. These magnitudes are well within the cumulonimbus scale. The decrease of mass flux in the second period is in close agreement with the decrease of precipitation echoes on the latter radar photographs (see Figure 11).

Thus it is clear that the cirrus outflow as seen by a geosynchronous satellite in a moderate-to-intense convection zone results from many individual cells embedded in the convective complex and that the model evaluates the average magnitudes of the fluxes.

Energy Flux Data and the Cloud Mass

Figure 14 presents the computed energy fluxes as a function of mass influx at the subcloud layer. These energy values refer to latent and sensible heat fluxes only. Figure 15 gives the convective cloud energy (ergs) as a function of cloud mass. The data on the cloud mass are evaluated using Brown's (1967) empirical equation

$$E_c = 1.4 \times 10^9 \, M_a^{1.14}$$

where E_c is energy (ergs) and M_a is the cloud mass in kilograms. The estimated cloud mass should refer to the clouds that extend to the upper troposphere and represent the average mass of the clouds participating in the cirrus outflow. According to Brown's (1967) convective cloud mass scale (see Figure 16), a single cumulonimbus should have cloud mass greater than 10^{11} kg, and in the

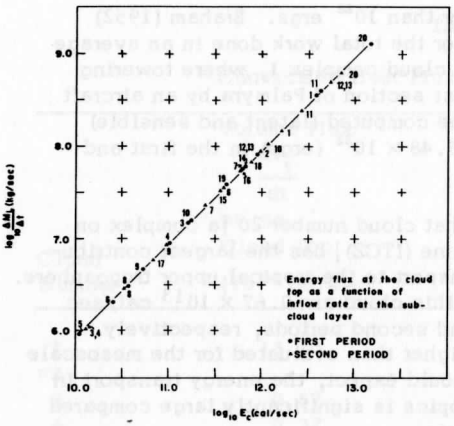

Figure 14. Plot of energy flux as a function mass inflow rate in the subcloud layer.

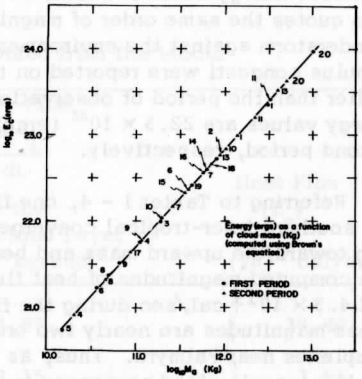

Figure 15. Plot of total energy of clouds as a function of cloud mass [computed from Brown's equation (1967)].

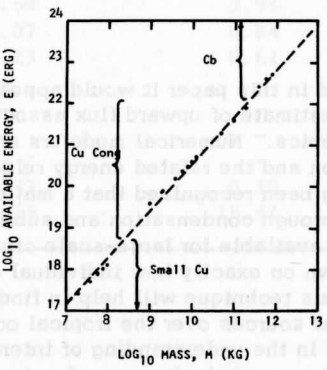

Figure 16. Available energy as a function of mass of convective cloud. Dashed line is least-squares fit to data points (Brown, 1967).

available energy scale it should be greater than 10^{22} ergs. Braham (1952) also quotes the same order of magnitude for the total work done in an average thunderstorm against the environment. In cloud complex 1, where towering cumulus congesti were reported on the west section of Palmyra by an aircraft earlier than the period of observations, the computed (latent and sensible) energy values are 22.3×10^{22} (ergs) and 9.48×10^{22} (ergs) in the first and second period, respectively.

Referring to Tables 1 - 4, one finds that cloud number 20 [a complex on the southern inter-tropical convergence zone (ITCZ)] has the largest contribution toward the upward mass and heat transport to the tropical upper troposphere. The computed magnitudes of heat flux for this cloud are 0.67×10^{13} cal/sec and 4.3×10^{13} cal/sec during the first and second periods, respectively. These magnitudes are nearly two orders higher than evaluated for the mesoscale complexes near Palmyra. Thus, as one would expect, the energy transport in the large-scale cloud processes in the tropics is significantly large compared to isolated mesoscale convective complexes.

It is, therefore, clear from the data presented that one can indeed estimate the average magnitudes of convective fluxes of mass and heat in the tropics from the ATS-I cloud photographs based on the model and classify the scales of convection accordingly.

CONCLUDING REMARKS

From the data presented in this paper it would appear that the technique is useful for the quantitative estimate of upward flux associated with a mesoscale convective regime in the tropics. Numerical modelers are interested in the character of mass circulation and the related energy release over wide scales of convections. It has long been recognized that a major part of this energy in the tropics is released through condensation and sublimation of water vapor, and this released energy is available for large-scale circulations in the tropics; however, very little is known on exactly how individual clouds contribute to large-scale circulation. This technique will help in finding the spatial distributions and magnitudes of heat sources over the tropical oceans, which would eventually be of importance in the understanding of interactions between the small-scale convective regimes and the large-scale atmospheric circulations.

This technique has been employed to evaluate the large-scale convective mass and heat transport over the mid-Pacific. The results will be communicated elsewhere soon.

TABLE 3

Convective Heat Flux Computed from the Model

Cloud Number	Volume Flux $\frac{dV_t}{dt}$ at the Cloud Top (10^{14} cc/sec)	Mass Flux $\frac{dM_L}{dt}$ from the Subcloud Layer (10^8 kg/sec)	Heat Flux (E_c) (10^{11} cal/sec)
1	13.20	3.57	38.40
*2	-	-	-
3	0.57	0.15	1.66
4	0.32	0.09	0.94
5	0.03	0.01	0.10
6	0.09	0.02	0.26
7	2.06	0.56	6.01
8	0.13	0.03	0.37
9	0.18	0.05	0.51
10	0.60	0.16	1.75
11	14.50	3.94	42.40
12-13	3.07	0.84	8.97
14	2.23	0.61	6.51
*15	-	-	-
*16	-	-	-
*17	-	-	-
*18	-	-	-
19	1.43	0.39	4.17
20	56.75	15.42	165.70

*Dissipating clouds.

TABLE 4

Convective Heat Flux Computed from the Model

Cloud Number	Volume Flux $\frac{dV_t}{dt}$ at the Cloud Top (10^{14} cc/sec)	Mass Flux $\frac{dM_L}{dt}$ from the Subcloud Layer (10^8 kg/sec)	Heat Flux (E_c) (10^{11} cal/sec)
1	5.56	1.51	16.20
2	3.25	0.88	9.50
3-4	0.05	0.01	0.13
*5	-	-	-
6	1.32	0.36	3.87
7	0.84	0.23	2.46
8	0.11	0.03	0.33
9	0.32	0.09	0.94
10	3.95	1.07	11.50
11	9.16	2.49	26.80
12-13	18.30	4.97	53.40
*14	-	-	-
15	1.22	0.33	3.56
16	2.05	0.56	5.98
17	0.24	0.06	0.70
18	2.59	0.70	7.57
*19	-	-	-
20	23.00	6.25	7.15

* Dissipating clouds.

TABLE 5

Using Brown's (1967) Energy Equation $M_A = \left(\frac{E_c}{1.4 \times 10^5}\right)^{1/1.14}$ (kg)

and our Heat Flux Data, E_c

Cloud Number	Energy (E_c) (10^{21} ergs)	Cloud Mass (M_A) (10^{11} kg)	Energy (E_c) (10^{21} ergs)	Cloud Mass (M_A) (10^{11} kg)
1	223.00	28.70	94.80	13.60
*2	-	-	55.50	8.47
3	9.62	1.82	-	-
4	5.45	1.11	0.77	0.20
5	0.56	0.15	-	-
6	1.52	0.36	22.60	3.85
7	34.90	5.64	14.40	2.59
8	2.14	0.49	1.95	0.45
9	2.98	0.65	5.48	1.11
10	10.10	1.91	67.40	10.00
11	246.00	31.30	156.00	21.00
12-13	52.00	8.01	312.00	38.50
14	37.70	6.04	-	-
*15	-	-	20.80	3.58
*16	-	-	34.90	5.64
*17	-	-	4.07	0.86
*18	-	-	44.20	6.94
19	24.20	4.09	-	-
20	960.50	94.80	392.10	432.60

* Dissipating clouds.

ACKNOWLEDGMENTS

The research reported in this paper was supported by the Weather Bureau Grant 27. The authors wish to express their thanks to Professor C. E. Anderson of The University of Wisconsin for discussion and Dr. S. K. Cox of the Space Science and Engineering Center, University of Wisconsin, for reading the manuscript during the preparation of this report.

REFERENCES

Anderson, C. E., 1960: "A study of the pulsating growth of cumulus clouds," Geophys. Res. Papers, No. 72, AFCRL, 136.

Bartman, F. L., 1967: "The reflectance and scattering of solar radiation by the earth," NASA Rept. No. NAS-54 (03), February.

Bates, F. C., 1961: "The Great Plains squall line thunderstorm: A model," Ph. D. dissertation, St. Louis Univ., Mo.

Borovikov, A. M., et al., 1963: Cloud Physics, U.S. Dept. Commerce, Washington, D.C.

Braham, R. R., Jr., 1952: "The water and energy budgets of the thunderstorm and their relation to thunderstorm development," J. Meteor., 9, 227-242.

Brown, R. A., 1966: "Three dimensional growth characteristics of an aerographic thunderstorm system," Satellite & Meso-meteor. Res. Proj. Paper No. 61, Dept. Geophysical Sciences, Univ. Chicago, 454.

Brown, R. A., 1967: "Mass and available energy in growing convective clouds," J. Atm. Sci., 24, 308-311.

Byers, H., and R. Braham, 1949: Thunderstorm, U.S. Dept. of Commerce, Washington, D.C.

Darkow, G., 1963: "A study of infrared radiation measurements in the vicinity of the sub-tropical tropopause," Ph. D. dissertation, Univ. Wisconsin.

Green, J.S.A., F. H. Ludlum, and J. F. R. McIlveen, 1966: "Isertropic relative flow analysis and the parcel theory," Quart. J. Meteor. Soc., 210.

Levine, J., 1959: "Spherical vortex theory of bubble like motion in cumulus clouds," Woods Hole Oceanographic Inst. Rept.

Ludlum, F. H., 1966: "Cumulus and Cumulonimbus Convection," Tellus, 18:4, 687-698.

Malkus, J. S., 1960: "Penetrative convection and an application of hurricane cumulonimbus towers," Contribution No. 1044, Woods Hole Oceanographic Institute.

Riehl, H., and J. S. Malkus, 1958: "On the heat balance in the equatorial trough zone," Geophysics, 6, 503-538.

Sikdar, D. N., and V. E. Suomi, 1968: "An objective technique of evaluating tropical mesoscale heat transfer from the ATS-I satellite photographs," Weather in Motion, Univ. Wisconsin Press, Madison (in press).

Spiegel, E. A., and G. Veronis, 1960: "On the Boussinesq approximation for a compressible fluid," Astrophys. J., 131, 442-447.

Whitney, L. F., 1963: "Severe storm clouds as seen from TIROS," J. Appl. Meteor., 2, 501-507.

Zipser, E. J., and R. C. Taylor, 1968: "A catalogue of meteorological data obtained during the Line Islands Experiment, February-April 1967," NCAR TN-35, Boulder, Colo.

Scanner's note:

This page is blank.

A CENSUS OF CLOUD SYSTEMS OVER THE TROPICAL PACIFIC

D. Martin and O. Karst

INTRODUCTION

ATS-I and ESSA-III satellite photographs were used to prepare a census of cloud systems over the tropical Pacific. The study area extended from 25° N to 25° S, 100° W to 160° E. It was divided into four equal-area regions having the equator and 150° W longitude line as common boundaries. The period of the study was from March 1967 to February 1968, inclusive, with these 12 months grouped into quarters to allow for possible seasonal variations in the data.

METHOD OF INVESTIGATION

Beginning with the first of March, each day's photographs were examined by region for organized cloud systems. All systems were given individual code numbers and tracked from day to day until they dissipated or moved out of the study area. Each day each system was typed according to its geometric appearance. After several months of photos were examined, the number of types was reduced to four: oval, line, wave, and spiral vortex. In addition, the following characteristics were noted: degree of organization (very weak, weak, moderate, or pronounced), location (by region and latitude), size (cloud area and cloud plus clear area), growth (from the previous day), movement (direction and speed from the previous day), length of life, cloud heights, and direction of blow-off.[1] The ITCZ itself was not classified as a line, but any disturbances on it were noted in the statistics.

ESSA-III computer mosaics, because they are gridded and more complete in their daily coverage, were the primary data source. Photographs from ATS-I were used mainly to check conclusions drawn from the ESSA products, being particularly useful in judging type and degree of organization, cloud heights, and blow-off. ATS time lapse films, although outstanding for estimating type and degree of organization, growth, movement, cloud heights, blow-off, and rotation, were too few in number to be used extensively.

---

[1] See Appendix A for an elaboration of nomenclature and procedure.

RESULTS OF THE CLOUD CENSUS

Figure 1a is a graph of annual system frequency for each region. Systems were tallied only once during their lifetimes and classified according to the highest level of organization that they attained. The organizational hierarchy from lowest to highest is oval, line, wave, vortex (see Appendix B). Systems which moved from one region to another were tallied in the region where they had spent the longest time. If a system moved beyond the outer boundaries of the study area it was classified according to the highest organization attained while within the study area.

From Figure 1a, it is clear that, for all regions through the entire year, ovals, with a total frequency of over 500, were by far the most numerous systems. Lines, waves, and vortices each had total frequencies between 100 and 200. All systems except lines were least frequent in the southeast. The total frequency of ovals, waves, and vortices was two-thirds greater in the northern hemisphere. This pattern was undoubtedly related to the occurrence of a stronger and more persistent ITCZ in the north. The frequency of the ITCZ is represented in Figure 1b. Lines and ovals showed a similar regional variation: Both were most frequent in the western regions. Waves were about five times more numerous in the northern regions; vortices were fairly uniformly distributed from region to region.

Seasonal changes[1] in system frequency (Fig. 1b) were substantial for waves and vortices in the northeast and for ovals in the southwest and southeast. In all regions lines had minimum frequency in September-October-November.

Figure 2 shows latitudinal frequency distributions of daily frequencies presented by season and region. Each system was tallied once each day of its lifetime. The arrow on the abscissa represents the mean position of the ITCZ.

Again, one sees seasonal and regional differences in the frequency of systems; also evident are substantial latitudinal differences in distribution. Most striking, perhaps, is the almost complete absence of systems close to the equator. A sharp peak in the total frequency distribution was typically observed 5 to 10 degrees away from the equator (near the mean latitude of the ITCZ); frequencies then decreased slowly toward the poles. In spite of considerable overlap, medians for each type tended to follow the same pattern, with the oval median closest to the equator, the vortex median furthest poleward, and the wave median somewhere between. Ovals were conspicuous in all regions during all seasons; waves and vortices varied considerably in their

[1] Seasonal references in this paper refer to local seasons.

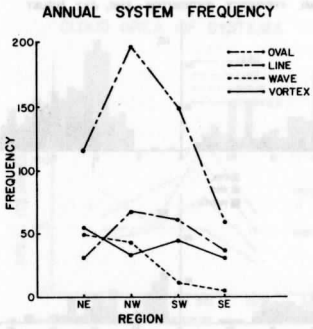

Figure 1. (a, left) Annual system frequency for each region. Systems are tallied only once and classified according to the highest level of organization they attained during their lifetime. (b, below) Seasonal system frequency plus the frequency of the ITCZ.

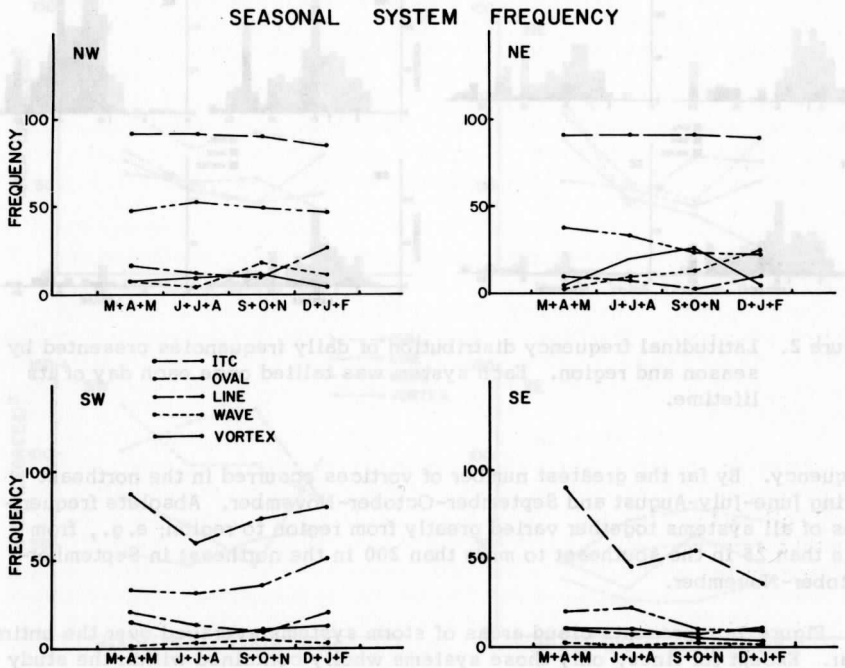

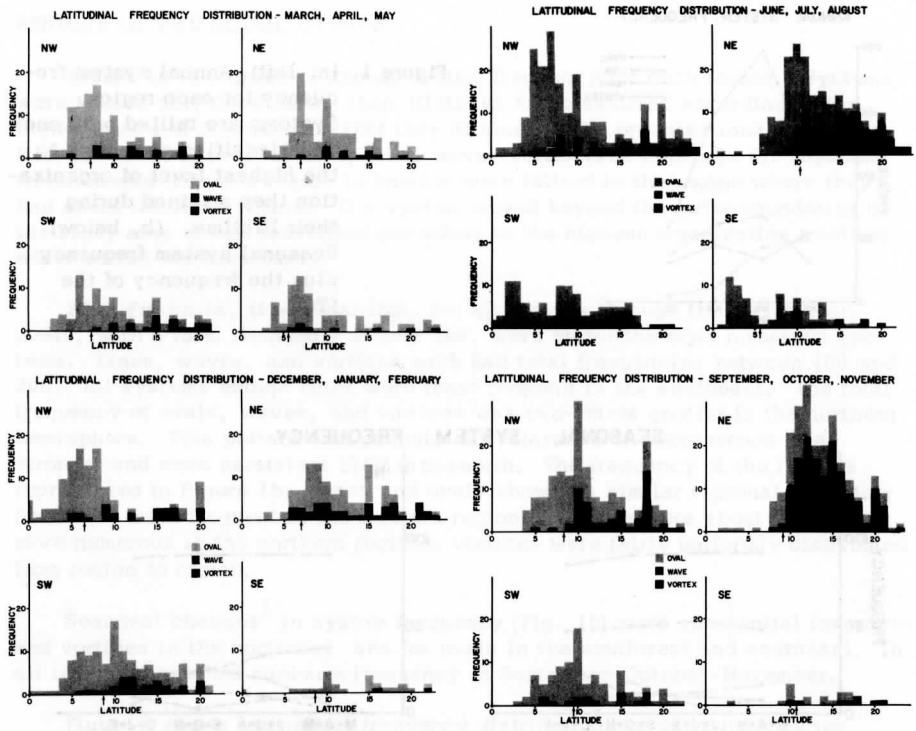

Figure 2. Latitudinal frequency distribution of daily frequencies presented by season and region. Each system was tallied once each day of its lifetime.

frequency. By far the greatest number of vortices occurred in the northeast during June-July-August and September-October-November. Absolute frequencies of all systems together varied greatly from region to region; e.g., from less than 25 in the southeast to more than 200 in the northeast in September-October-November.

Figure 3a represents cloud areas of storm systems averaged over the entire year. Except for lines, only those systems wholly contained within the study area are included in the averages. One sees especially well the tendency of systems (except lines in the northwest) to be larger in the two western regions; most particularly this was true of the southern hemisphere. Over the whole area, on the average, waves and lines were 50 percent larger in cloud area than ovals and vortices.

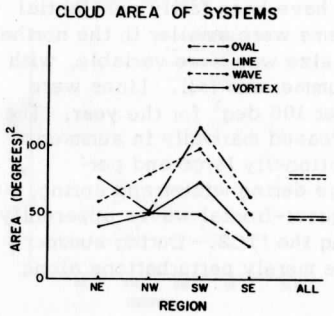

Figure 3. Cloud area of systems (a, left) averaged over the year and (b, below) by seasons.

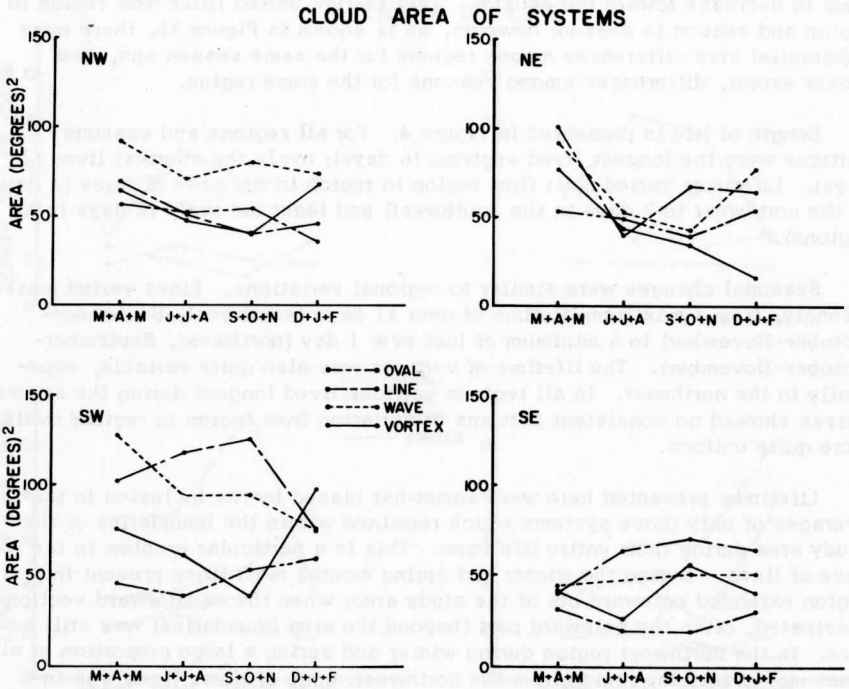

In Figure 3b seasonal changes are shown to have been fairly substantial except for ovals. During summer and fall, systems were smaller in the northern hemisphere; in the southern hemisphere average size was more variable, with lines alone showing a decrease in area during summer and fall. Lines were remarkably large in the southwest, averaging over 100 deg^2 for the year. The size of southwest vortices is shown to have increased markedly in summer; however, this was partly the effect of one exceptionally large and persistent vortex. In the northeast waves were large during winter and spring, due mainly to the more southerly occurrence of quasi-frontal waves apparently related to the subtropical jet, and often involving the ITCZ. During summer and fall in the northeast most wave systems were merely perturbations along the ITCZ.

Not shown in these graphs is the tendency for the maximum size of systems to decrease toward the equator. This feature varied little from region to region and season to season; however, as is shown in Figure 3b, there were substantial size differences among regions for the same season and, to a lesser extent, differences among seasons for the same region.

Length of life is presented in Figure 4. For all regions and seasons vortices were the longest lived systems (6 days); ovals the shortest lived (2 days). Lifetimes varied most from region to region in the case of lines (2 days in the northwest to 7 days in the southwest) and least for ovals (2 days in all regions).

Seasonal changes were similar to regional variations. Lines varied most strongly, from a maximum lifetime of over 11 days (southwest, September-October-November) to a minimum of just over 1 day (northwest, September-October-November). The lifetime of vortices was also quite variable, especially in the northeast. In all regions vortices lived longest during the summer. Waves showed no consistent patterns of variation from region to region; ovals were quite uniform.

Lifetimes presented here were somewhat biased by the inclusion in the averages of only those systems which remained within the boundaries of the study area during their entire lifetimes. This is a particular problem in the case of lines. During the winter and spring months most lines present in a region extended poleward out of the study area; when the equatorward section dissipated, often the poleward part (beyond the area boundaries) was still active. In the northwest region during winter and spring a large proportion of all lines moved into the region from the northwest; none of these lines was included in the lifetime averages. Thus there is a strong bias in lifetime averages toward transient, apparently nonfrontal lines that occasionally developed in the vicinity of the ITCZ. In the southwest, on the other hand, frontal bands which had dissolved over Australia often regenerated as they crossed the Coral Sea and moved into the southwest region. Many of these quasi-frontal, long-

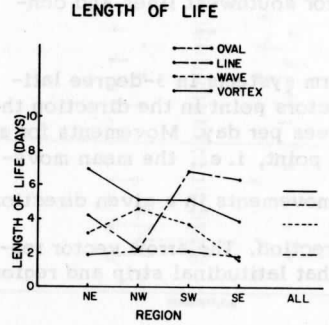

Figure 4. Length of life for systems (a, left) averaged over the year and (b, below) by seasons.

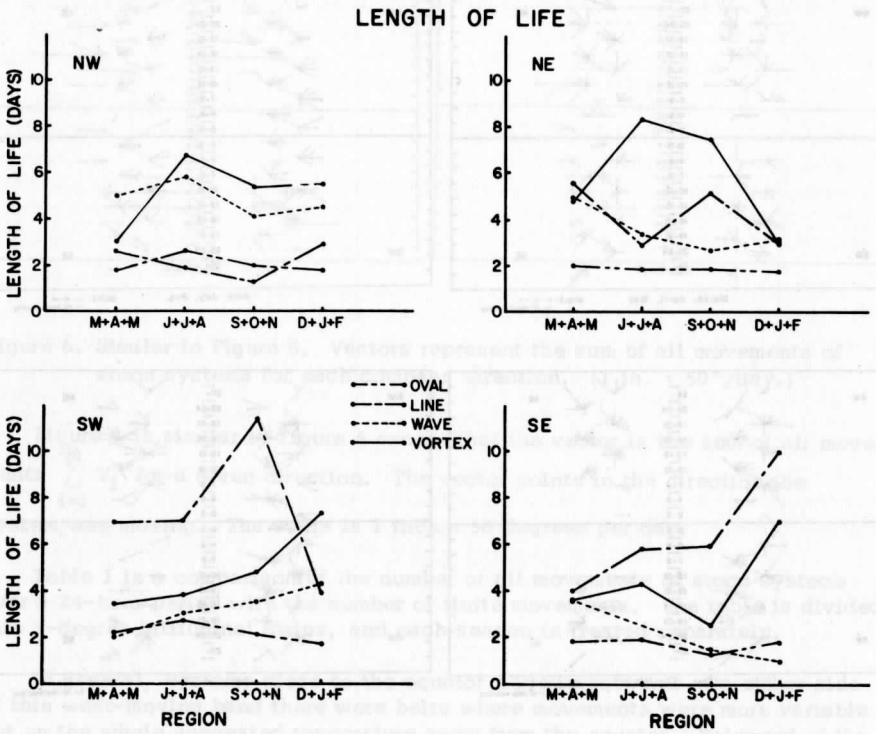

lived systems were included in lifetime averages for southwest lines and contributed to the high averages observed there.

Figure 5 represents the mean movement of storm systems in 3-degree latitudinal strips for each season and region. The vectors point in the direction the system was moving. The scale is 1 inch = 10 degrees per day. Movements for a strip were averaged individually for each compass point, i.e., the mean movement $\overleftarrow{V_0} = \frac{1}{n_0} \sum_{i=1}^{n_0} V_i$, where n_0 is the number of movements in a given direction, and V_i is the individual movements in a given direction. The arrow vector represents the mean vector of all compass points in that latitudinal strip and region.

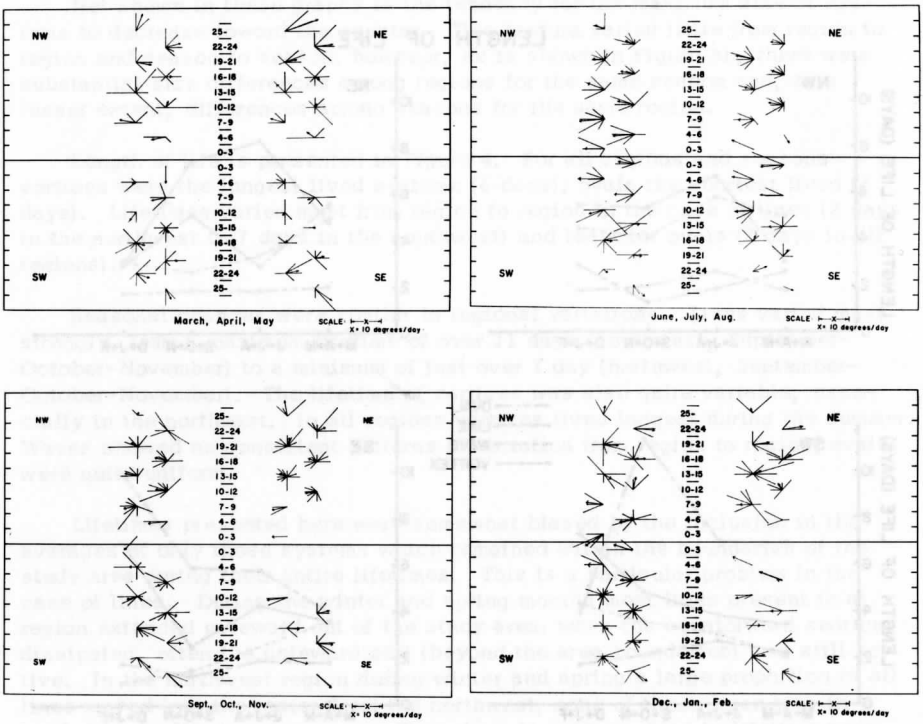

Figure 5. The mean speed of storm systems for each compass direction in 3-degree latitudinal strips by region. Arrow vector represents mean vector of all movements in that latitudinal strip. (1 in. = 10° /day.)

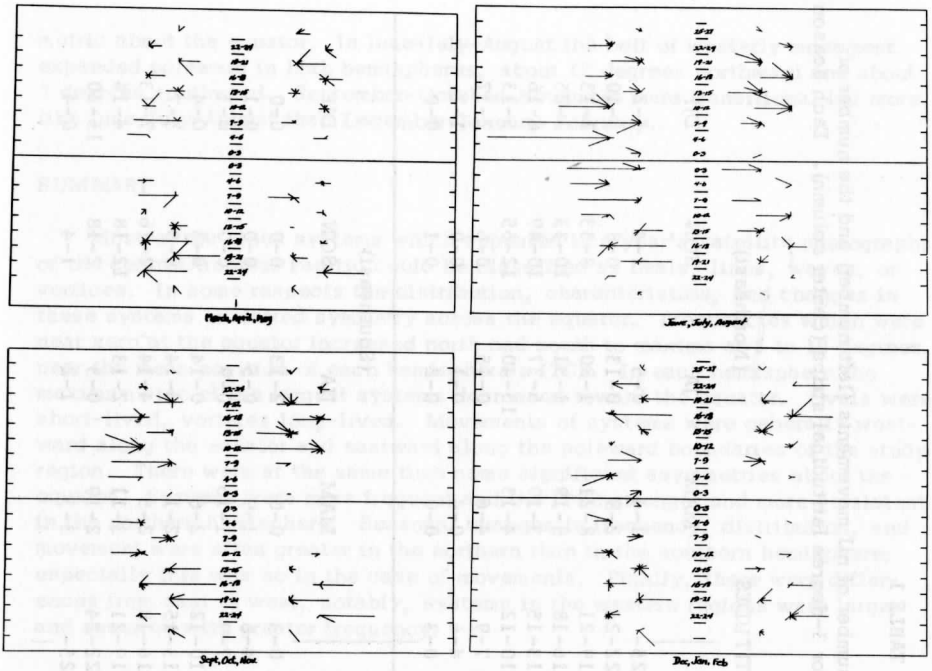

Figure 6. Similar to Figure 5. Vectors represent the sum of all movements of storm systems for each compass direction. (1 in. = 50°/day.)

Figure 6 is similar to Figure 5 except that the vector is the sum of all movements $\sum_{i=1}^{n_0} V_i$ for a given direction. The vector points in the direction the system was moving. The scale is 1 inch = 50 degrees per day.

Table 1 is a comparison of the number of nil movements of storm systems over a 24-hour period with the number of finite movements. The table is divided into 3-degree latitudinal strips, and each season is treated separately.

In general, systems close to the equator moved westward. On either side of this west-moving band there were belts where movements were more variable but on the whole suggested recurvature away from the equator. Poleward of the recurvature belts movements were easterly, with a weak to moderate poleward component. This pattern changed irregularly from season to season. December-January-February were much like March-April-May, with the belts nearly sym-

TABLE 1

Columns of number pairs in each region show the number of nil movements (left number) and the number of finite movements (right number) of storm systems for 3-degree latitudinal strips (center column). Each season is treated separately.

(Northwest)				LATITUDES	(Northeast)			
MAM	JJA	SON	DJF		MAM	JJA	SON	DJF
1-3	4-7	3-3	0-3	25-	1-4	0-5	1-4	1-2
4-9	9-23	6-8	1-10	22-24	2-8	0-13	0-8	3-10
7-15	10-26	6-24	6-34	19-21	8-21	1-20	8-33	3-13
3-11	2-16	6-25	10-26	16-18	8-19	1-31	10-33	3-25
2-9	1-12	2-16	1-10	13-15	3-10	5-37	10-49	6-16
2-12	2-27	4-41	0-4	10-12	4-13	13-40	12-55	5-13
6-14	4-34	3-29	3-16	7-9	4-6	0-15	0-6	2-17
6-6	2-38	1-9	1-26	4-6	0-4	0-1	0-0	1-3
0-0	1-6	0-1	1-9	0-3	0-0	0-2	0-1	0-0
(Southwest)					(Southeast)			
MAM	JJA	SON	DJF		MAM	JJA	SON	DJF
0-1	0-26	0-0	0-3	0-3	0-0	2-13	0-0	0-0
3-8	1-17	1-12	1-14	4-6	1-9	0-5	0-0	0-1
1-18	3-19	1-19	0-15	7-9	1-15	0-9	0-0	0-1
3-6	2-11	3-18	3-29	10-12	2-6	0-14	0-3	0-4
11-21	14-16	5-15	13-25	13-15	2-1	3-14	0-5	5-7
12-32	12-40	9-31	12-17	16-18	2-5	4-14	2-16	7-13
4-25	3-19	8-28	4-20	19-21	3-11	2-13	12-18	4-14
6-24	3-6	2-9	4-16	22-24	2-19	0-3	2-18	15-30
4-7	0-3	0-6	1-11	25-	3-3	1-2	1-4	0-4

metric about the equator. In June-July-August the belt of westerly movement expanded poleward in both hemispheres, about 12 degrees northward and about 3 degrees southward. September-October-November were transitional but more like June-July-August than December-January-February.

SUMMARY

Most of the cloud systems which appeared in a year's satellite photographs of the central tropical Pacific could be classified as ovals, lines, waves, or vortices. In some respects the distribution, characteristics, and changes in these systems exhibited symmetry across the equator. Frequencies which were near zero at the equator increased north and south to maxima at 5 to 10 degrees, near the mean position of each hemisphere's ITCZ. In each hemisphere the maximum size of the largest systems decreased toward the equator. Ovals were short-lived, vortices long-lived. Movements of systems were generally westward along the equator and eastward along the poleward boundaries of the study region. There were at the same time some significant asymmetries about the equator. Systems were more frequent and the ITCZ stronger and more persistent in the northern hemisphere. Seasonal changes in frequency, distribution, and movement were often greater in the northern than in the southern hemisphere; especially this was so in the case of movements. Finally, there were differences from east to west, notably, systems in the western regions were larger and occurred with greater frequency.

Analysis of the data tabulations is continuing. Through a consideration of system movement and blow-off we hope to gain some additional understanding of the upper level circulation, particularly its seasonal and regional variations. Plots showing the changing area of individual systems from day to day should yield insights into life cycles. Fourier analysis of daily system frequencies may show periodic variations in disturbance activity. It may be possible to calibrate systems in terms of energy transport and to estimate vertical energy fluxes over the tropical Pacific; perhaps we can also derive estimates of the spectral energy distribution between convective and synoptic scales. Combining these possibilities with what has been done already will give fairly complete satellite climatology of disturbances over the tropical Pacific.

APPENDIX A

GROUND RULES AND DEFINITIONS FOR SYSTEM CHARACTERISTICS

Organization

Type — Geometric description of a system: oval, line, vortex, or wave.

Degree

Depending on the intensity of its organization, each system was classified as very weak, weak, moderate or active (pronounced); nonexistent was also used in describing the ITCZ. Intensity was determined by the similarity of the actual cloud system to its geometric "ideal" form; also, type of cloud (stratiform, low convective, deep convective, cirrus, etc.) and delineation—the contrast between a cloud system and surrounding clouds.

Location

Region

The tropical Pacific was divided into four regions:

Northeast: 0° to 25°N, 150°W to 100°W
Northwest: 0° to 25°N, 150°W to 160°E
Southwest: 0° to 25°S, 150°W to 160°E
Southeast: 0° to 25°S, 150°W to 100°W

Latitude

The latitude of system centers was noted to the nearest degree except for lines, where the latitudinal extent was noted.

Size

Cloud

The area of cloud associated with a system in degrees of latitude squared. Only that part of a system lying inside the study area was considered.

Cloud + clear

Where organized clear areas were associated with a system, the cloudy and clear areas were measured in degrees of latitude squared.

Growth

The change in the cloud area of a system from the previous day, computed only if on successive days the system remained entirely within the outer boundary of the study area.

Length of life

The number of consecutive days during which a system was noted.

Movement

The change in the position of the system center from the previous day. Speed was measured in degrees per day; direction according to a 16-point compass.

Cloud heights — Inferred heights of clouds in the system:

L:	Low
M:	Middle
H:	High
L, M:	Low and middle
L, M, H:	Low, middle, and high
M, H:	Middle and high
L+M:	Convective cells extending to the troposphere
L+M+H:	Convective cells extending through the troposphere; cumulonimbi

Direction of blow-off — The direction in which cirrus anvils point when cumulonimbi are present.

Rotation

Direction — The direction in which systems were observed to rotate (clockwise or counter-clockwise). It was possible to confidently determine this parameter only when ATS time-lapse films ("CD" series) were available.

Speed — Approximate speed of rotation (slow = $< \frac{1}{2}$ rev/day; fast = $> \frac{1}{2}$ rev/day).

APPENDIX B

FORMS OF TROPICAL CLOUD DISTURBANCES

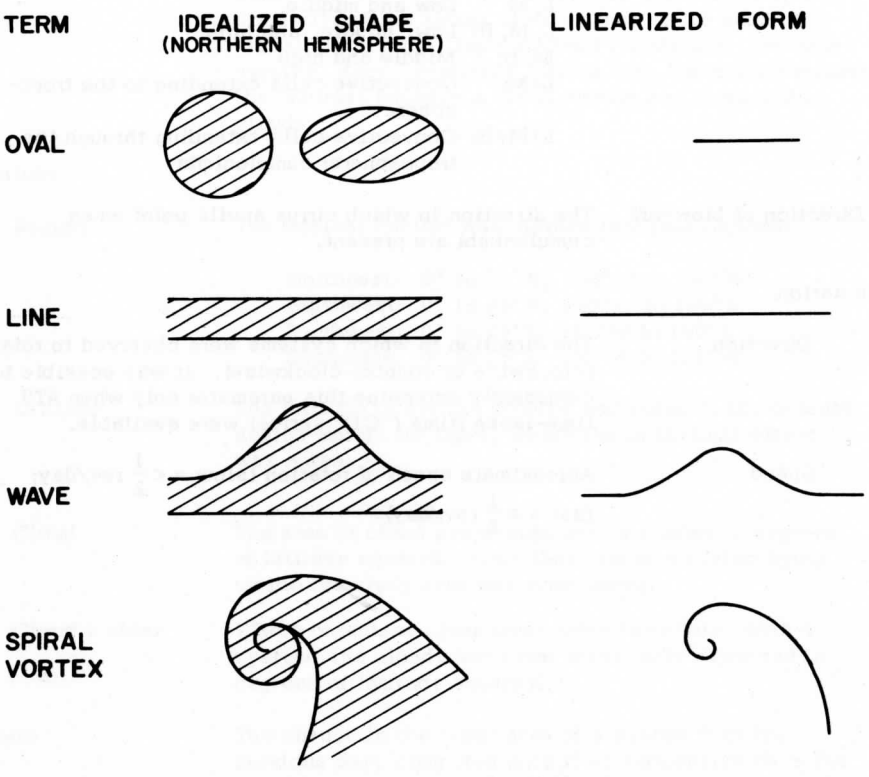

DEVELOPMENT OF A SPIRAL FROM A LINE:

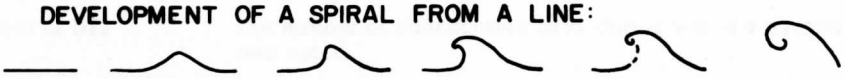

(Originated by E. G. Astling)

A PHOTOGRAPHIC SUMMARY OF THE EARTH'S CLOUD COVER FOR THE YEAR 1967

J. Kornfield and A. Hasler

ABSTRACT

Results of a multiple exposure averaging technique which allows one to summarize satellite cloud photographs for monthly and half-monthly periods are presented in the form of a cloud atlas of the entire earth for the year 1967. The cloud atlas makes it possible to observe many climatological features of the cloud field and their changes with time which are not readily apparent on the individual satellite pictures. Some of the major features are discussed briefly.

INTRODUCTION

In the past ten years, meteorological satellites have provided man his first extraterrestrial glimpses of the earth's cloud cover. These were truly glimpses; the small area viewed, the limited resolution, and the odd angles from which the cameras viewed the earth, as well as the irregularity of the orbit rarely permitted similar views of the same area. In the past two years, two technological advances in satellite meteorology have provided new possibilities to further our knowledge of the global cloud cover: the computer-produced cloud mosaics developed by the National Environmental Satellite Center of ESSA (Bristor, Callicott, and Bradford, 1966), which provide a single daily picture of the global cloud cover on either a polar or mercator projection, and the acquisition of high-quality pictures of nearly an entire hemisphere, which was achieved from earth synchronous orbit by NASA's Applications Technology Satellite Spin Scan Cloud Cameras (ATS-I and ATS-III).

These advances provide a means of gathering information on the distribution of clouds on a scale never before possible. In fact, the information content in one of these pictures is so great that it saturates the largest computers available today.

To summarize the cloud photographs, then, and to produce a "cloud atlas" which would permit a first view of the salient global cloud features, a simple photographic technique has been applied which takes advantage of the additive property that the photographic process can provide (Appendix). Photographic film is exposed to a series of satellite pictures taken at the same time daily and of the same geographic area. The resulting photographs provide a measure of the earth's cloud cover as viewed by the satellite for the chosen time period.

THE CLOUD SUMMARIES

The multiple-exposure cloud atlas which follows provides a summary of the ESSA-III and -V computer-produced mosaics for 1967.

The multiple exposures provide an approximation to the average cloud cover for monthly and half-monthly periods.[1] This approximation is broadly discussed in the Appendix. Because of variations in the original ESSA product and our own procedures, it was impossible to eliminate all variations in exposure, contrast, size, etc., from picture to picture. The "averages," however, enable one to observe the large-scale cloud features and their changes with time. It would be impossible to describe all of the features in these summaries, so we will only touch upon some of their more salient patterns.[2] Circulations on all scales may be inferred from the changing cloud patterns (Bryson, 1968).

Results of the multiple exposure technique applied to the mid-season months of January, April, July, and October, 1967, are presented in Figures 1 and 2. The complete cloud summary consisting of half-monthly pictures of the entire earth for 1967 is shown in Figures 3 through 10. Figure 11 consists of Northern and Southern Hemisphere polar stereographic projections and mercator projection grids to aid the reader in using the cloud summary.

The albedo difference between the ocean and land surfaces on the original photographs available is lost in the multiple exposure. Continents on the multiple exposures are usually marked because of the increased cloud cover above them or at their boundaries. One example of this phenomenon is the Indian subcontinent, which, in these pictures, is only clearly visible during the southwest monsoon season. In July the orographic lifting, which the Western Ghats provide, is marked by a line of heavier cloud cover along the subcontinent's western coast. (See Figures 2, 5, and 8; 75°E, 15°N.) Large areas of stratus or fog are found on the western coasts of South America and South Africa. They

---

[1] A maximum of three photographs was missing for any monthly period.

[2] Some features not discussed here are described in an earlier article by the authors (Kornfield, et al., 1967).

coincide fairly well with the regions associated with eastern boundary currents, which are relatively cold, due both to upwelling and because they carry water from higher latitudes. The stratus and fog seen most of the year off the western coast of South America coincide with the location of the cold Peruvian and Chilean currents. Off the coast of southwest Africa and Angola the stratus is associated with the cold Benguela current; in July and October (see Figures 5 and 6) the increase suggests a possible increase in upwelling.

Differences in topography, soil type, and vegetation also manifest themselves in these "averages" (Kornfield, et al., 1967); for example, the ranges of the Himalayas and Andes can be seen with varying degrees of clarity throughout the year, because of both the snow on them and the increased cloud cover above. The effects of topography and local surface heating on cloud production are seen on some of the world's islands. In the July and August averages (see Figures 2, 5, and 8), Cuba, Hispaniola, and Jamaica are clearly marked in the Caribbean Sea. The islands best marked in the Pacific Ocean are those of Indonesia, the Philippines, Taiwan, and Hawaii. Albedo effects which manifest differences in soil types, topography, and vegetation are found in the northern desert regions of Africa and on the Saudi Arabian peninsula. In South America, a persistent bright area at 20° S, 66° W marks the Salar de Uyuni, a large salt flat. All of these features vary with the season and, also depending on the ambient cloud cover, can be observed more readily at different times of the year.

The effects of monsoonal circulations on cloud distribution are also apparent on these pictures. In Africa, with the flow of the dry, dust-laden harmattan and the Egyptian northerlies across the Sahara, one finds the northern Savannah lands from about 5° N to 15° N almost completely devoid of clouds in January (see Figures 1 and 3). At the same time, below the equator a low-pressure system brings moist air onto the continent from the Atlantic and Indian Oceans, resulting in a considerable increase in cloud cover. The cloud patterns are almost completely reversed in July (see Figures 2 and 5), when moist air from the Atlantic invades the northern Savannah lands bringing the rains with it. The highlands of western Africa and its coast at approximately 5° N from 5° W to 15° E are clearly marked by clouds in July. (See Figures 2 and 5.) The subsidence associated with the high over southern Africa permits virtually no precipitation; there was a difference in rainfall of 10 inches[1] between the dry and wet seasons on the continent's interior in 1967. In tropical South America as in Africa, the changes in cloud cover between the wet and dry seasons also mirror observed precipitation patterns. In July, during the peak of the dry season, the eastern coast of Brazil south of the equator, which is a region of maximum winter rainfall, has cloud cover. (See Figure 5. Note: This is readily apparent in the original prints.) Just to the west in January and October (see Figures 3

[1] Deutcher Wetterdienst Seewetteramt.

and 6) one finds a relatively cloud-free region. This area of Brazil to the west of Cape Sao Rogue is known to be relatively dry (Trewartha, 1962). The "cloud averages" also show a decrease in cloudiness over the Guyanas during October (see Figures 2 and 6), which is their dry season. Rain forests to the east of the Andes are marked by clouds throughout the year.

One interesting feature of the southwest monsoon is exhibited over the Arabian Sea to the east of Cape Guardafui in July. A relatively clear zone is found which apparently outlines Africa's coast during the summer months June through August, which is visible in Figures 2, 4, and 5. This zone may be due to warm, dry, upper level air brought from Northeast Africa and its subsequent modification.

An equatorial "doublet," persistent regions of convective activity on either side of the equator, occurs in the late winter and spring months over the Indian Ocean (see Figures 1, 3, and 4). A double cloud structure also appears in the late fall in the eastern Pacific where a suggestion of its existence has been made (Alpert, 1945). The southern part of the double structure, which marks convective activity in the eastern Pacific in October (see Figures 2 and 6), breaks in the region of the Galapagos also suggesting that the position of the cumulus bands is determined by the property of the sea. The clear zone in the Pacific, from the Galapagos to about 165°E, as well as the cloud break at the Galapagos, may owe their origins in part to the cold subsurface Cromwell current which flows along the equator from the western Pacific to the Galapagos as well as to "normally" upwelled water along the equator (Lettau, 1968).

We have only touched upon some of the more prominent global features of the cloud field here. Indeed, circulations on many scales are evident in the photographs. It is hoped that the meteorological community will find this photographic summary a useful guide to the earth's average cloud field.

CONCLUSION

Results of a multiple-exposure averaging technique which allows one to summarize satellite cloud photographs for monthly and half-monthly periods have been presented in the form of a cloud atlas of the entire earth for the year 1967. This atlas makes it possible to observe many climatological features of the cloud field and their changes with time which are not readily apparent on the individual satellite pictures.

ACKNOWLEDGMENTS

The writers would like to thank ESSA for providing the computer-produced mosaics; Professor V. E. Suomi, director of the University of Wisconsin Space Science and Engineering Center, for his support; and David Cadle and John Riggs of the SSEC Photographic Laboratory for their conscientious work in producing the multiple-exposure "averages."

REFERENCES

Alpert, A. C., 1945: "The intertropical convergence zone of the eastern Pacific region (1)," Bull. Am. Meteor. Soc., 26, 426-432.

Bristor, C. L., W. M. Callicott, and R. E. Bradford, 1966: "Operational processing of satellite cloud pictures by computer," Mon. Wea. Rev., 94, 515-527.

Bryson, R. A., 1968: "A Climatologist Views Weather Satellites, NASA-ERC Colloquium, Cambridge, Mass., May 27, 1968.

Fletcher, R. D., 1945: "The general circulation of the tropical and equatorial atmosphere, J. Meteor., 2, 167-174.

Kornfield, J., et al., 1967: "Photographic cloud climatology from ESSA III and V computer produced mosaics," Bull. Am. Meteor. Soc., 48, 878-883.

Lettau, H., 1968: Personal communication.

Trewartha, G. T., 1962: The Earth's Problem Climates, Univ. Wisconsin Press, Madison.

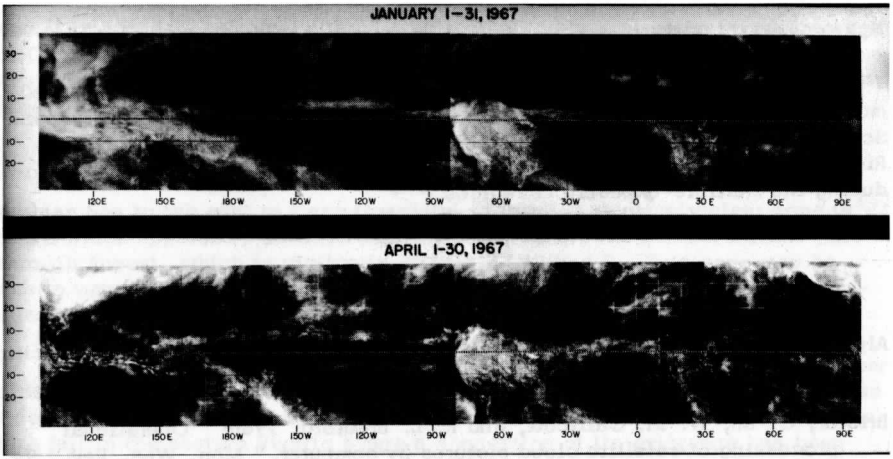

Figure 1. January 1-31 and April 1-30, 1967. Mercator projection multiple-exposure monthly averages from ESSA-III and ESSA-V computer-produced mosaics.

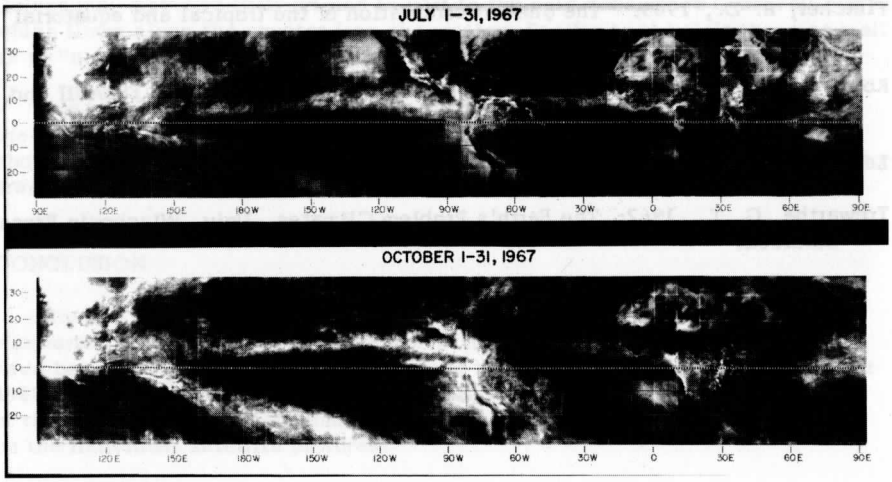

Figure 2. July 1-31 and October 1-31, 1967. Mercator projection multiple-exposure monthly averages from ESSA-III and ESSA-V computer-produced mosaics.

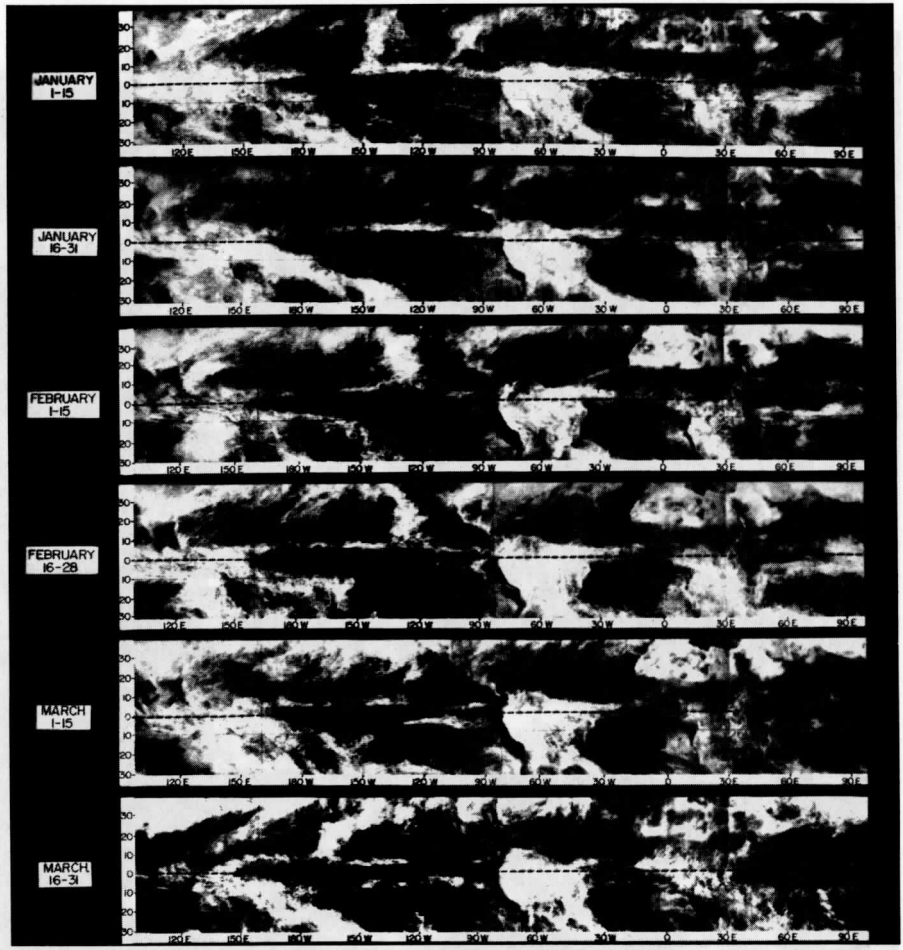

Figure 3. Mercator projection. January-March 1967 multiple-exposure half-monthly averages from ESSA-III and ESSA-V computer-produced mosaics.

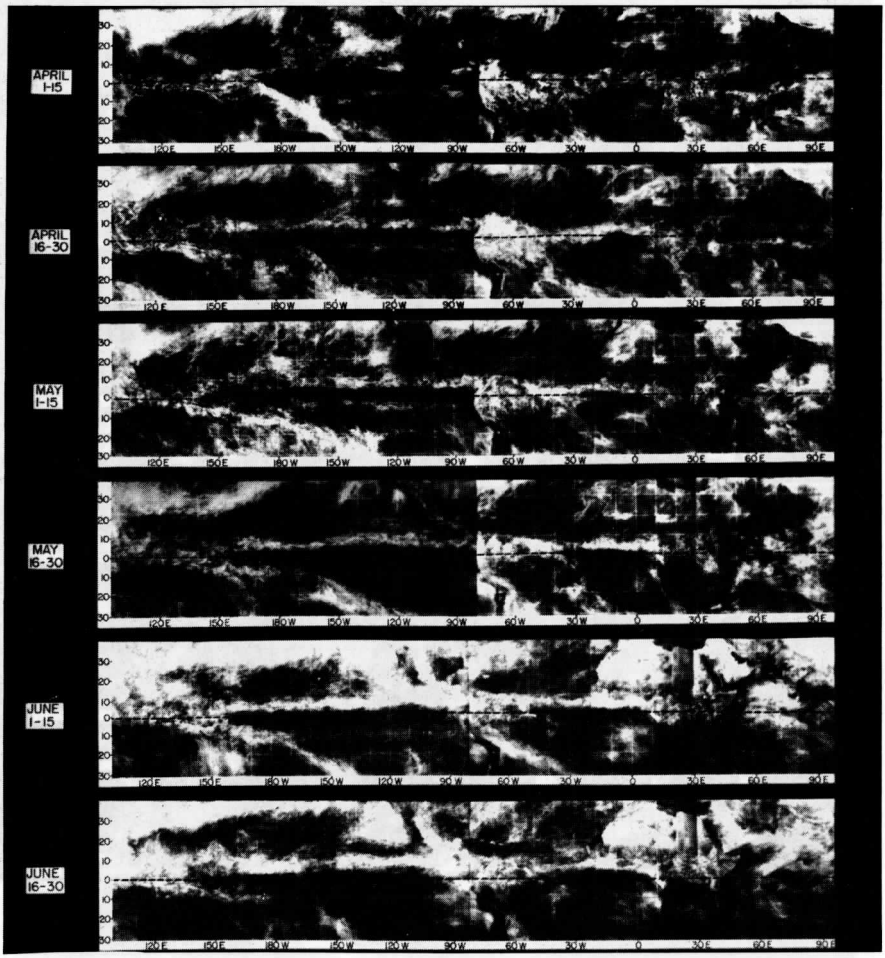

Figure 4. Mercator projection. April-June 1967 multiple-exposure half-monthly averages from ESSA-III and ESSA-V computer-produced mosaics.

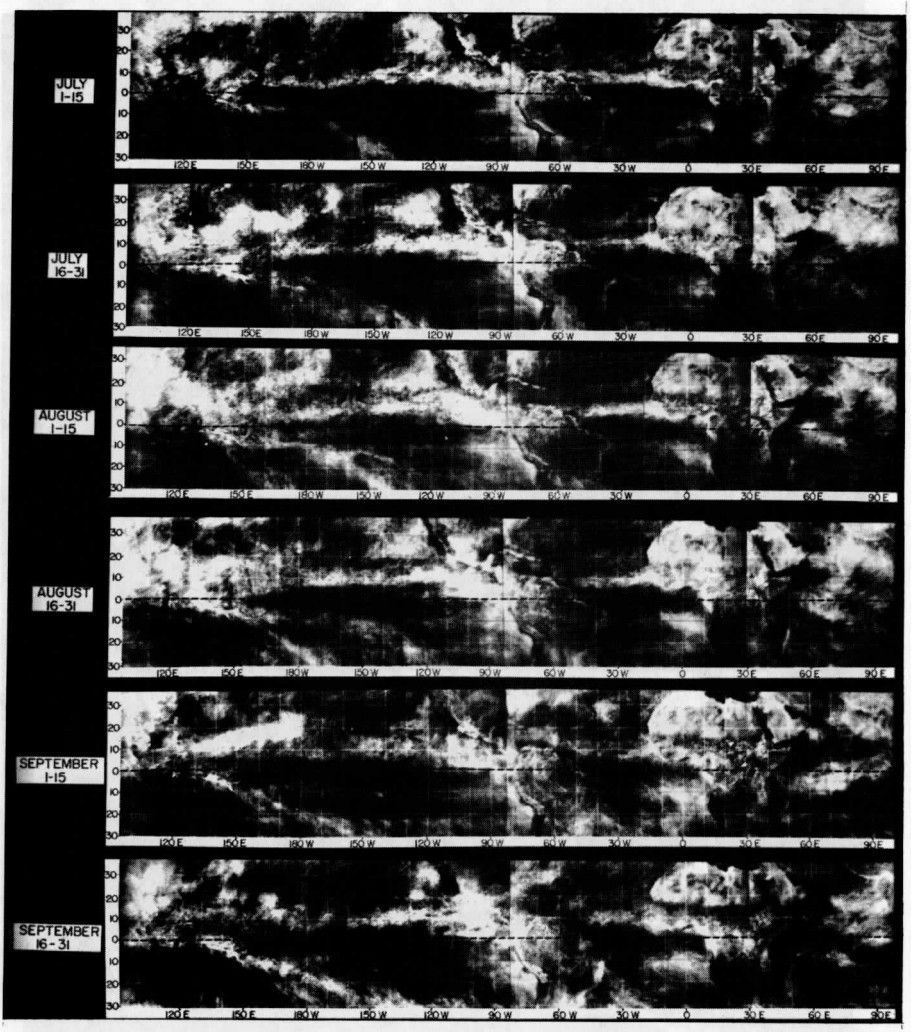

Figure 5. Mercator projection. July-September 1967 multiple-exposure half-monthly averages from ESSA-III and ESSA-V computer-produced mosaics.

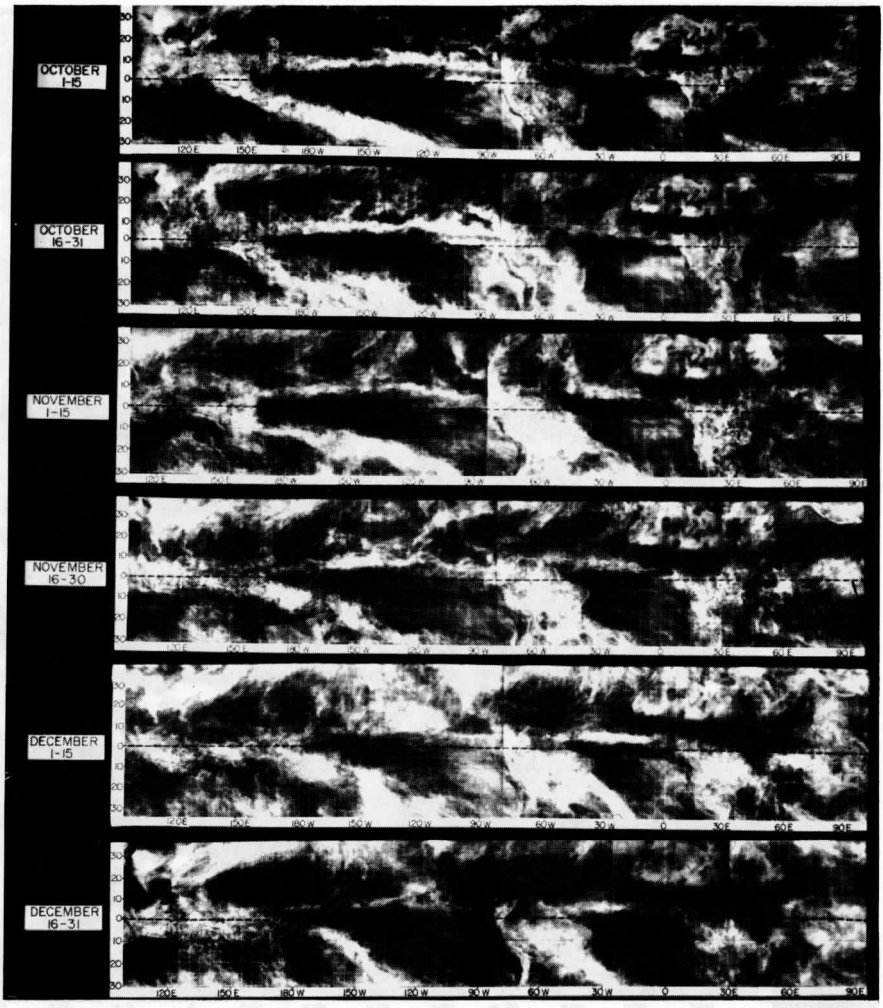

Figure 6. Mercator projection. October-December 1967 multiple-exposure half-monthly averages from ESSA-III and ESSA-V computer-produced mosaics.

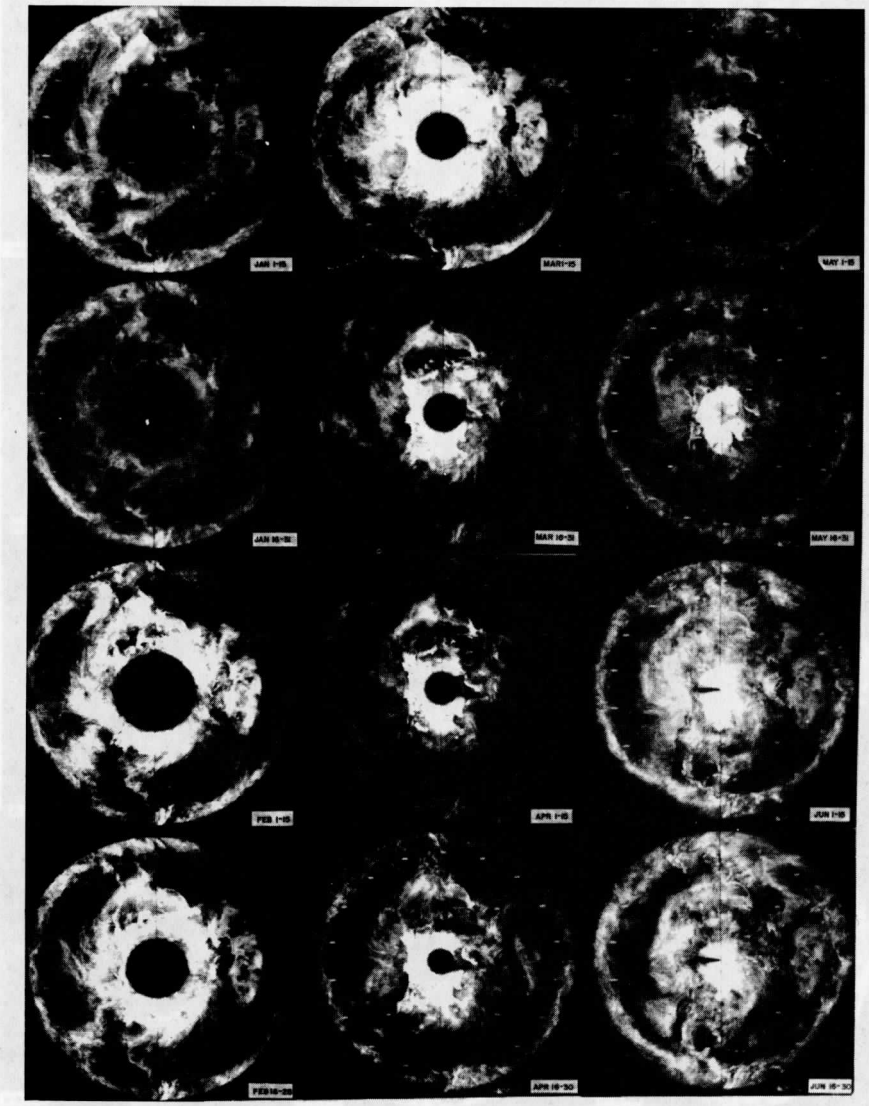

Figure 7. Northern Hemisphere 1967. First half of multiple-exposure half-monthly averages from ESSA-III and ESSA-V computer-produced mosaics.

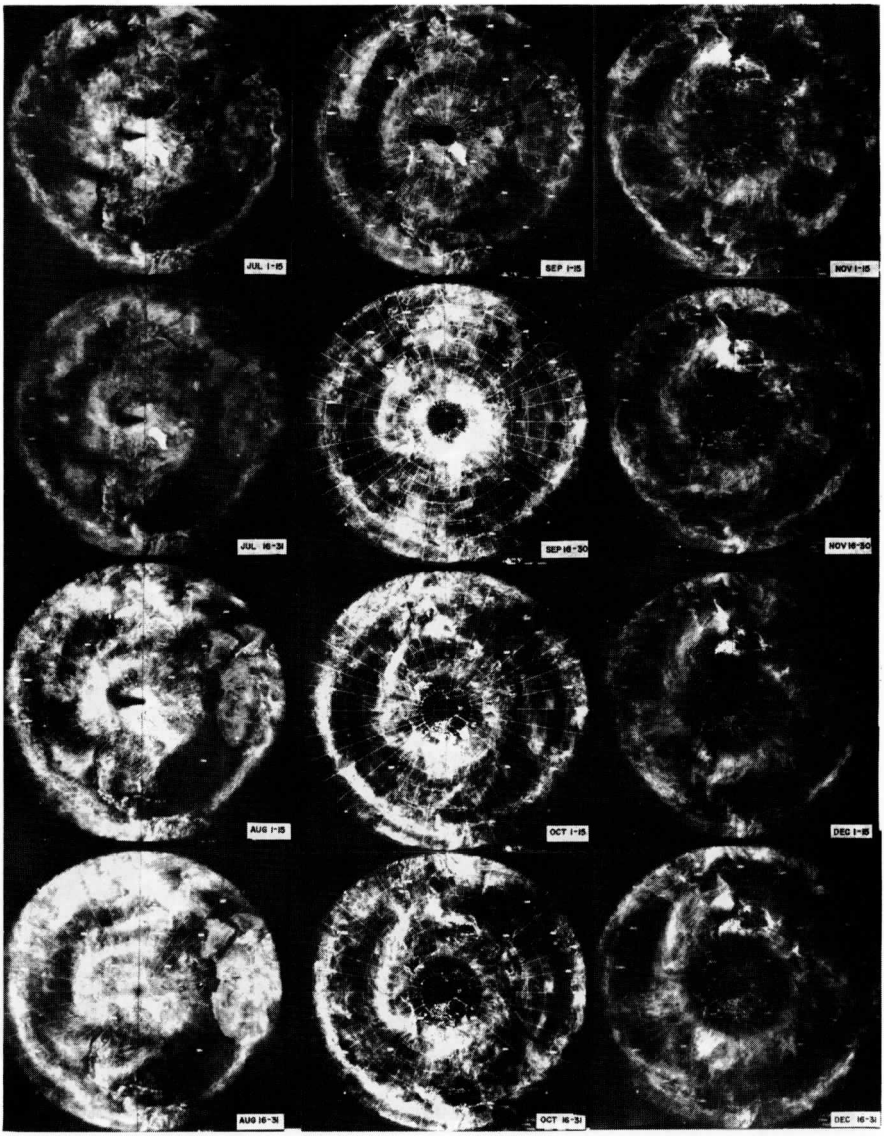

Figure 8. Northern Hemisphere 1967. Second half of multiple-exposure half-monthly averages from ESSA-III and ESSA-V computer-produced mosaics.

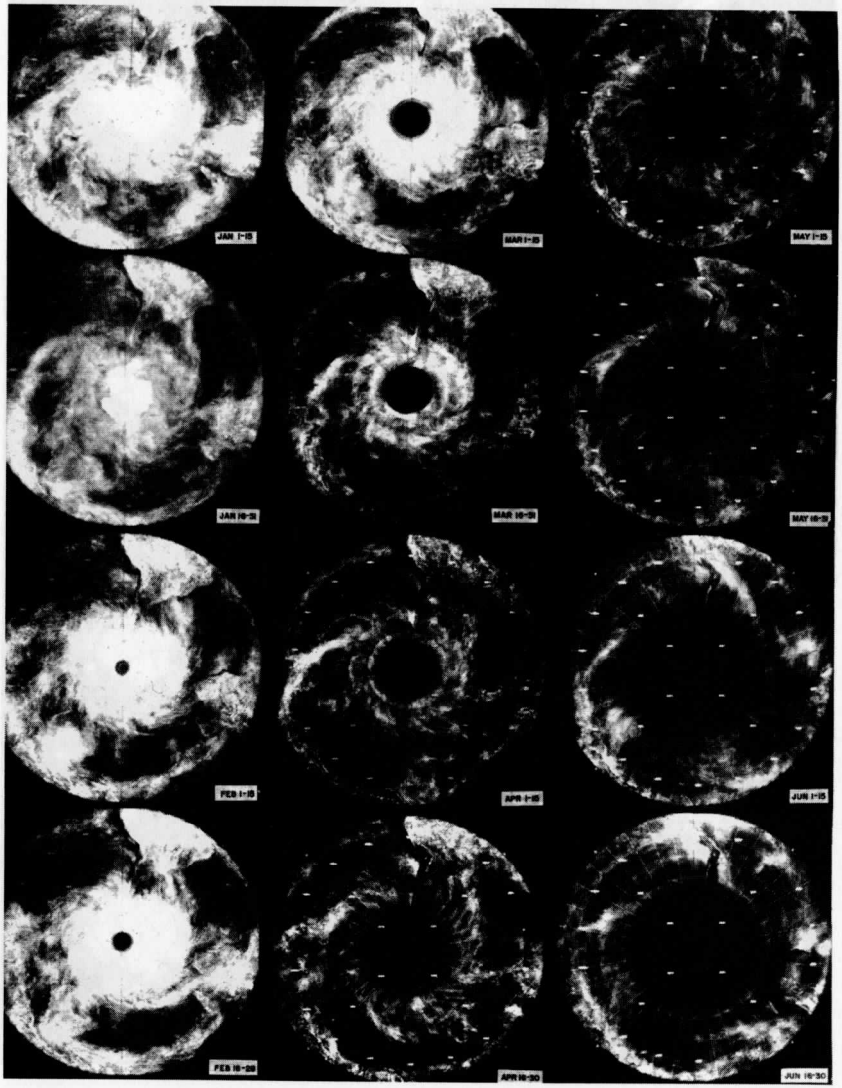

Figure 9. Southern Hemisphere 1967. First half of multiple-exposure half-monthly averages from ESSA-III and ESSA-V computer-produced mosaics.

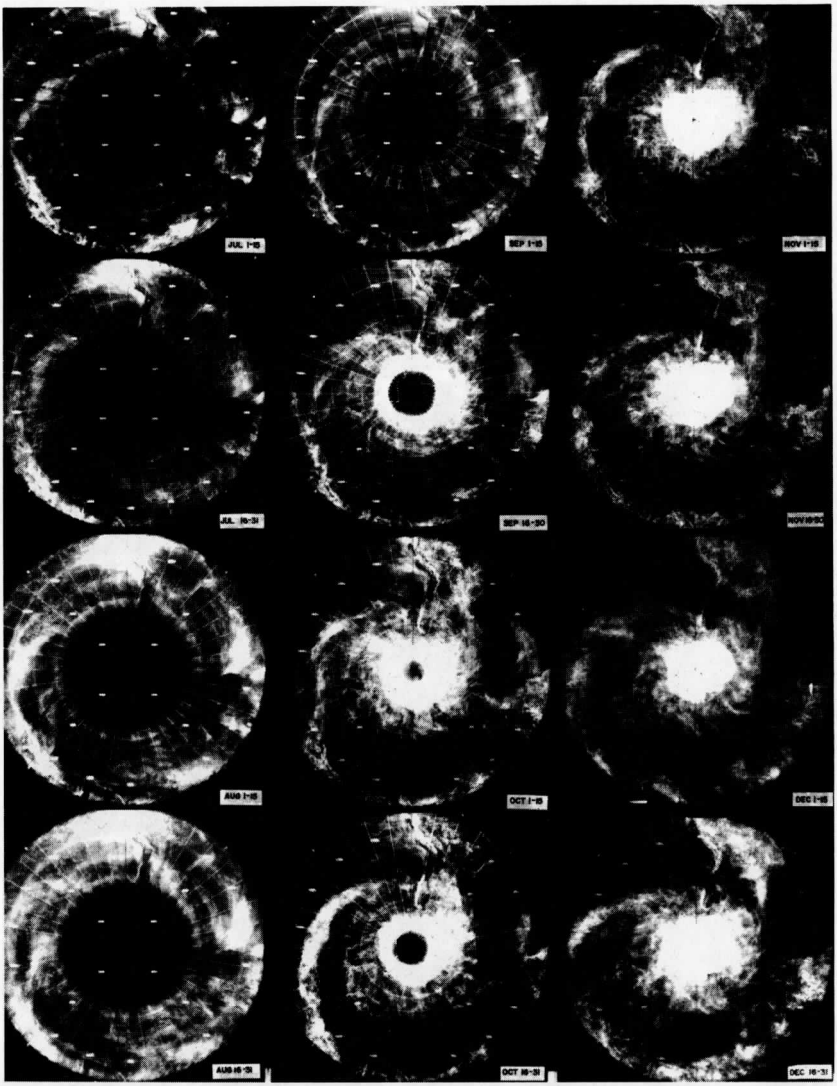

Figure 10. Southern Hemisphere 1967. Second half of multiple-exposure half-monthly averages from ESSA-III and ESSA-V computer-produced mosaics.

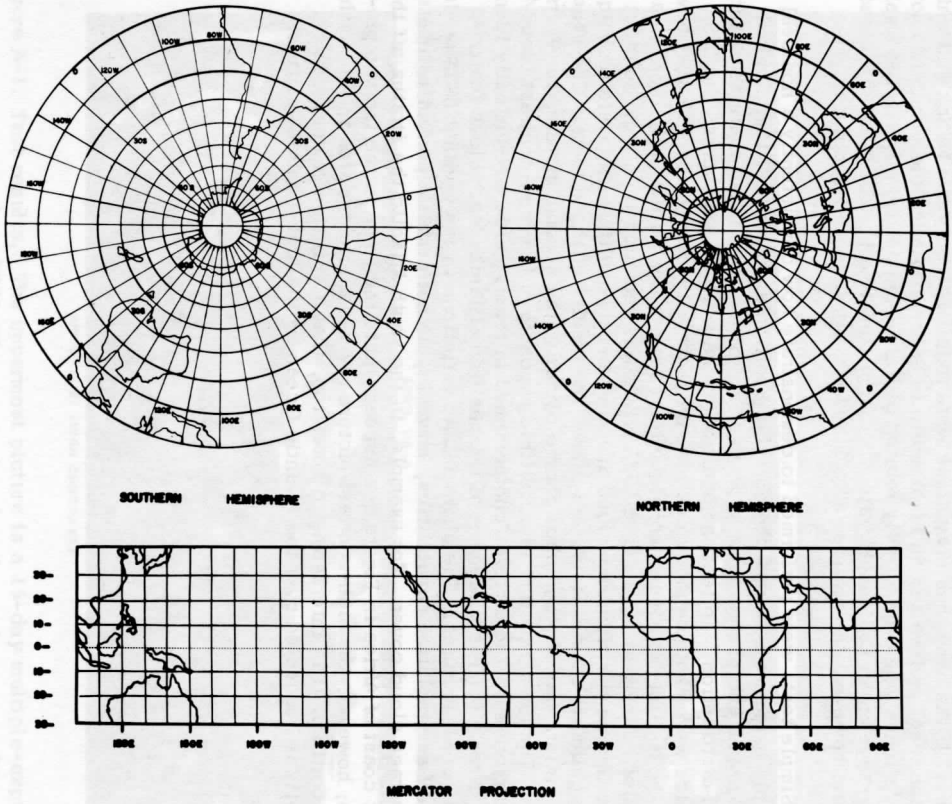

Figure 11. Northern Hemisphere, Southern Hemisphere, and mercator projection grids.

APPENDIX

In order to obtain a picture of the average cloud cover, the full gray scale would not be needed. It would only be necessary to distinguish between a cloud's presence or absence, a simple cloud/no-cloud decision on each ideal picture. If the number of gray steps were reduced to only two (black and white) on each ideal picture and an ideal multiple exposure made, the resultant photograph's tones would be directly related to the average cloud cover. The small tonal range on an ESSA photograph does approximate a perfect cloud/no-cloud picture; however, the pictures are biased by variations in brightness.

Simple tests were performed to demonstrate how consistently a nonideal multiple exposure performs photographic addition and how well the nonideal photographs and photographic processes reproduce the salient features of the cloud distribution. To test the addition of the multiple exposures, the ESSA mosaics were photographed in reverse order for a 15-day period. To test how well the multiple exposure technique represents a consistent picture of the average cloud distribution, a set of ESSA prints was reproduced on high-contrast film affecting the cloud/no-cloud decision and the multiple-exposure technique was applied to them. Figure A-1 shows the results of these tests. The uppermost picture was photographed chronologically; the second picture, in reverse order. The lowest picture is a multiple exposure of the high-contrast cloud/no-cloud pictures. The pictures photographed in reverse order are virtually identical. Nearly perfect agreement of the position of large-scale cloud features exists in all pictures. The photographic variations in the original ESSA product as well as resolution capabilities, however, do not permit a perfect estimate of average cloud cover. For example, in the south Atlantic the stratus off the west coast of Africa in Figure A-1 appears quite the same in the top two pictures; however, the high-contrast picture reveals a brighter area in the northeast portion. It is interesting to note, too, that a splitting of convective activity is suggested over the Atlantic Ocean by the high-contrast picture.

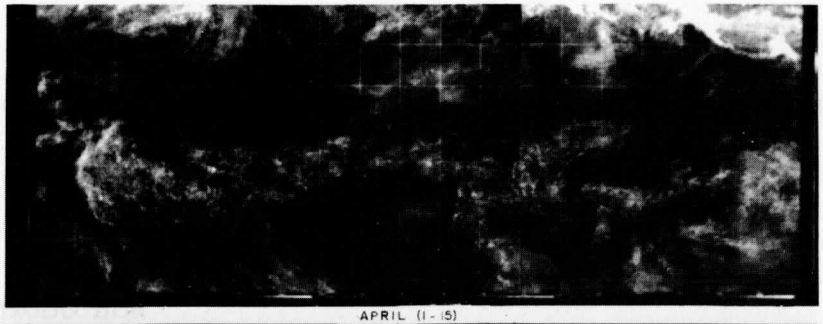

APRIL (1-15)

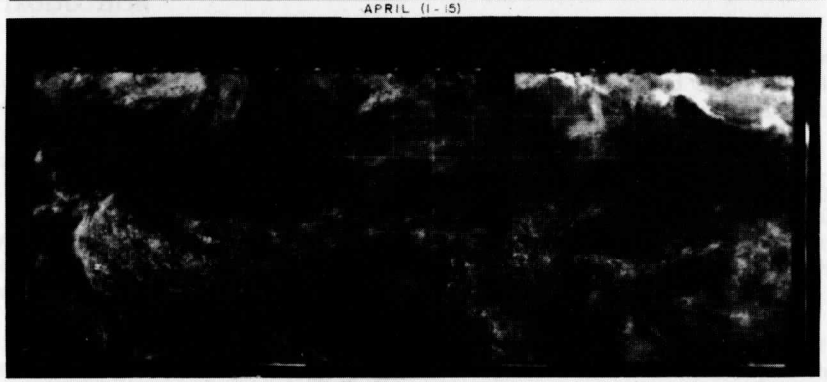

APRIL (15-1)

APRIL (1-15) (HIGH CONTRAST)

Figure A-1. Test results. The uppermost picture is a 15-day multiple-exposure average from ESSA-III computer-produced mosaics exposed in chronological order. The center picture is photographed identically as the first except that it was exposed in reverse order. The lowest picture is a 15-day multiple-exposure average made from ESSA-III computer-produced mosaics which were copied on high-contrast film before applying the multiple-exposure technique.

Scanner's note:

This page is blank.

METEOROLOGICAL APPLICATIONS OF REFLECTED RADIANCE MEASUREMENTS FROM ATS-I AND ATS-III[1]

T. Vonder Haar

INTRODUCTION

Two meteorological experiments on NASA's Applications Technology Satellites (ATS) were the Spin Scan and Multi-Color Spin Scan Cloud Cameras (SSCC and MSSCC). The experiments are designed to take unique advantage of the ATS geostationary orbits and to image and measure reflected radiance from cloud patterns over a large portion of the earth on a nearly continuous basis throughout the daylight hours. Thus, for the first time, the dimension of time is added to the study and use of data from meteorological satellites. This allows the study of weather in motion, the formation and dissipation of clouds and weather systems, and the possibility of inferring wind velocities from the remote satellite platform.

The spin scan "cameras" are not really cameras at all. They consist of quantitative photomultiplier tubes behind the optics of a small telescope. Thus they measure the reflected radiance from clouds and the ocean and ground features in selected spectral regions. Brief descriptions of the experiments' characteristics are given by Suomi and Vonder Haar (1969), Warnecke and Sunderlin (1968), McQuain (1967), and Suomi and Parent (1968). The ATS Meteorological Data Catalogs issued by the Goddard Space Flight Center, NASA, contain additional information. Complete technical details of the spin scan camera experiments, together with a large number of scientific papers based on ATS data will soon be published in a book, Weather in Motion, by the University of Wisconsin Press.

Most meteorological attention has thus far been directed to the high-resolution images obtained from the ATS experiments. These photographs, and especially the time-lapse movies made from them, provide a new view of weather conditions and stimulate and support many research and operational

---

[1]Presented at 49th Ann. Meet., Am. Meteor. Soc., New York, Jan. 20-23, 1969.

efforts. The purpose of the present paper is to point out the equally wide range of possible meteorological applications of the quantitative measurements of reflected radiance from the ATS satellites. Such data allow the wide dynamic range and high areal resolution of the spin scan sensors to be exploited to the fullest and are particularly valuable when used to complement the more familiar photographs.

REFLECTED RADIANCE DATA FORMAT

NASA ground stations receive the ATS data and have three recording options available. In schematic form, Figure 1 shows these options: Data can be recorded (1) on film through an electronic photofax to produce the standard ATS photograph; (2) on magnetic tape in analog form to archive the measurements and to provide precision display photographs at a later time; or (3) on magnetic tape in digital form.

The reflected radiance data are more generally accessible to scientific users from the digital tapes, although an A/D system at The University of Wisconsin allows archived data to be used in a computer as well. The digital tape records consist of 8192 samples along each east-west ATS scan line. In 8-bit form, each sample of the continuous scan is represented by a digital "count" ranging from 0 to 255. An entire ATS-I picture consists of approximately 2000

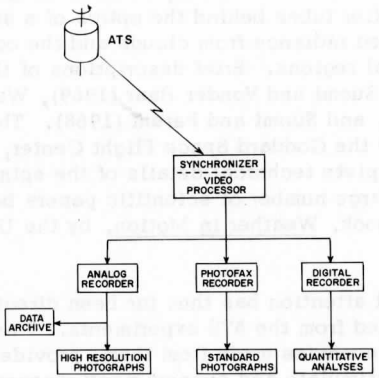

Figure 1. Schematic depiction of the data flow sequence from the Spin-Scan Cloud Camera experiments.

such records, one for each scan line. ATS-III carried a 3-channel color instrument and also had more lines per picture, 2400, than ATS-I. Thus, more than three times as many records make up an ATS-III picture, and these fill three to four standard high-density magnetic tapes.

On a digital tape, data samples are available approximately every 1 nm in the east-west direction and each scan line is about 2 nm north or south of the adjacent scans. Nominal camera resolution is 2 nm at the half-power point, so an array of digital samples represents an overlapping field of scan spots.

RELATIVE RADIANCE VALUES

The response of the spin scan cameras to reflected solar radiance is highly linear over a wide range. Thus, the voltage output of these instruments, or the digitized counts from this signal, is a good measure of relative values of reflected radiance. For many quantitative meteorological applications good relative values of "brightness" are very useful.

For an example of the high areal resolution, refer first to Figure 2. This is a 4-times enlargement of a standard ATS-III photograph. Severe weather conditions were found over part of the south-central United States on this day, and the case has been examined by several groups using the time-lapse movie technique. By 2236Z the severe weather areas along the frontal zone can be noted within the indicated box. Figure 3 is an objective analysis of relative reflected radiance values for the boxed region. The very brightest areas are solid black. Sharp gradients of radiance mark the edges of the bright cirrus plumes seen on the photographs.

This quantitative analysis allows one to accurately pinpoint the location of each very bright area. These points mark the apparently thickest, best developed convective clouds. Note that some of these regions are located well under the plume, as well as at the apex of each plume. Radar reports for one hour after the picture time show a very good correspondence between the brightest reflected radiance regions and the location of heavy precipitation areas. Several scientists (Sikdar, et al., 1969) are extending this study of severe weather regions using ATS radiance data, with special attention to time sequences of such analyses. The high areal resolution of the ATS data is shown by the great detail within each 50- to 60-mile-square latitude-longitude grid. Note also that the wide dynamic range of radiance measurements provides more than adequate brightness resolution.

Figure 2. Enlargement of an ATS-III photograph on 19 April 1968. Regions of severe weather are enclosed within the box.

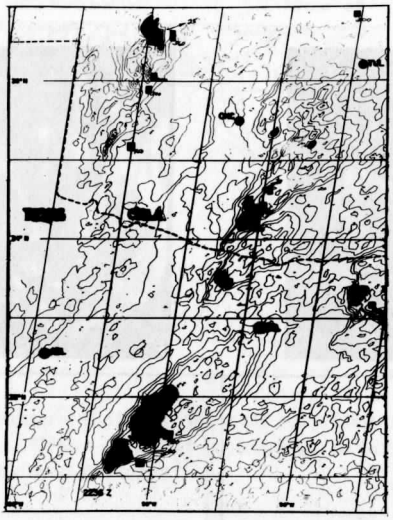

Figure 3. Reflected radiance analysis of the boxed area in Figure 2. Brightest areas are black; squares mark radar reports 69 min after analysis time.

Figure 4 contains two radiance analyses from two pictures obtained the same day over the equatorial Pacific. In this case the radiance data cover an area several thousand miles in extent. Pairs or sequences of these analyses are used to study cloud development, dissipation, or motion. They are particularly useful in supporting aircraft, ship, balloon, and surface observations made during a field experiment. ATS-I data are available during the Line Island Experiments and ATS-III will support BOMEX. In Figure 4, the large-scale features show little change over a 23-min interval (except for the sun-glitter region). Near point A, however, changes in mesoscale convective cloudiness can be noted.

Vonder Haar, et al. (1968) used relative radiance values to study ring-like cloud patterns in the deep tropics. An example is shown in Figure 5, where very small scale clear regions have apparently deep convective clouds on their perimeters. Preliminary results on the time and space variations of these phenomena are being used by scientists concerned with numerically modeling these features. ATS data in this form can support meteorological research projects that were unable to use earlier types of satellite observations.

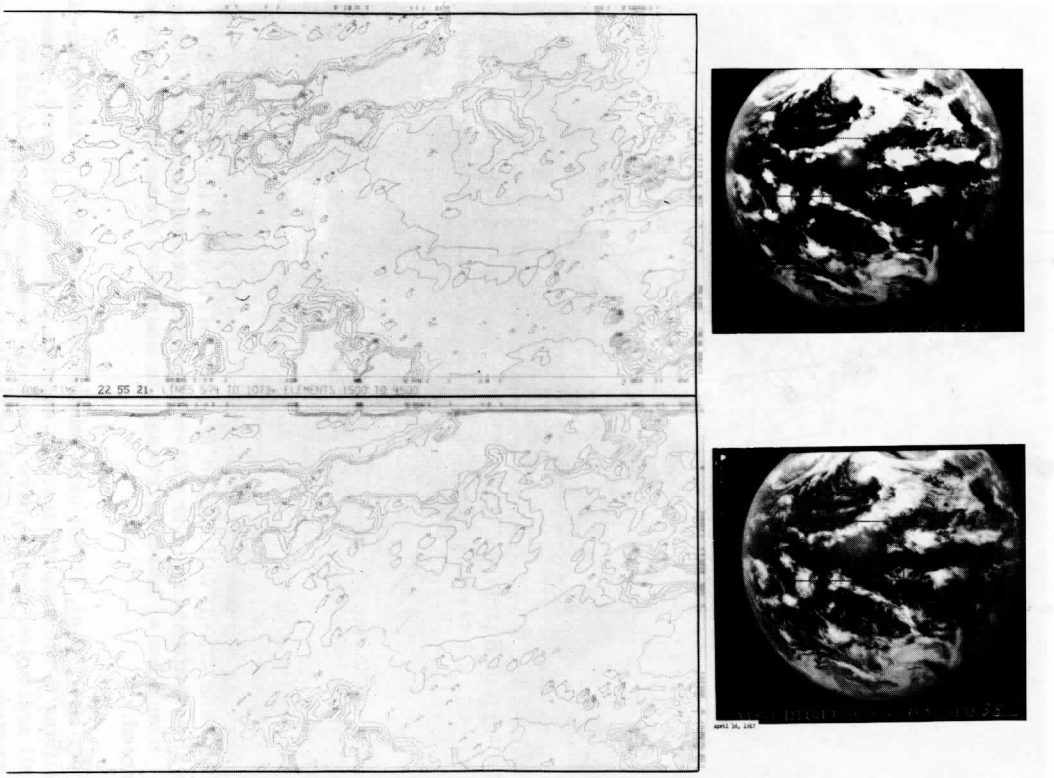

Figure 4. Isolines of reflected radiance over the same region from two consecutive ATS-I photographs.

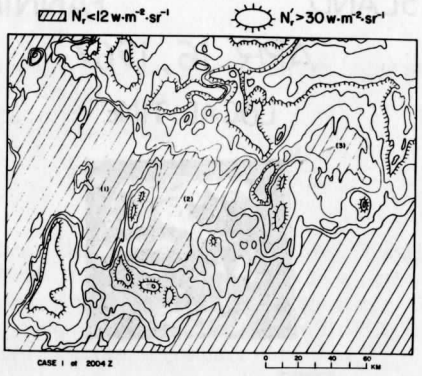

Figure 5. Reflected radiance analysis of small ring-like cloud systems in the deep tropics. Cross-hatched regions are clear; "tic" marks locate the brightest cloud features.

Figure 6, from Levanon (1969), shows reflected radiance values from a sequence of "pictures" used to examine the sun-glitter region near the Line Islands. From each radiance plot (cross-section) he has located two island regions and extracted the distribution of sea-surface slopes from temporal variations of radiance (intensity). Using a relation between the variance of the waves' slope and wind velocity, he obtained a good estimate of surface wind speed. This demonstrates the application of quantitative ATS data to obtain a basic observation, rather than to study cloud features.

ABSOLUTE RADIANCE MEASUREMENTS

With the aid of a proper calibration, Peekna, Parent, and Vonder Haar (1969) show how the voltage output of the ATS sensors can be converted to absolute reflected radiance measurements. Hanson and Suomi (1969) have provided this calibration for ATS-I. Based on both these papers one can use the defining relation:

$$N_r'(\phi_2, \gamma) = \rho'(\gamma, \delta, \phi_1, \phi_2)\, N_i'(\phi, \delta) \cos \delta d\Omega \qquad (1)$$

to express the effective reflected radiance, N_r', in terms of the effective incident radiance, N_i'; the effective bi-directional reflectance, ρ', of the reflecting surface; and the four angles, γ, δ, ϕ_1, and ϕ_2, which define the attitude of the reflecting surface to the sun and the satellite sensor. Effective radiance denotes that which is within the limited spectral region (0.45 - 0.65μ) viewed

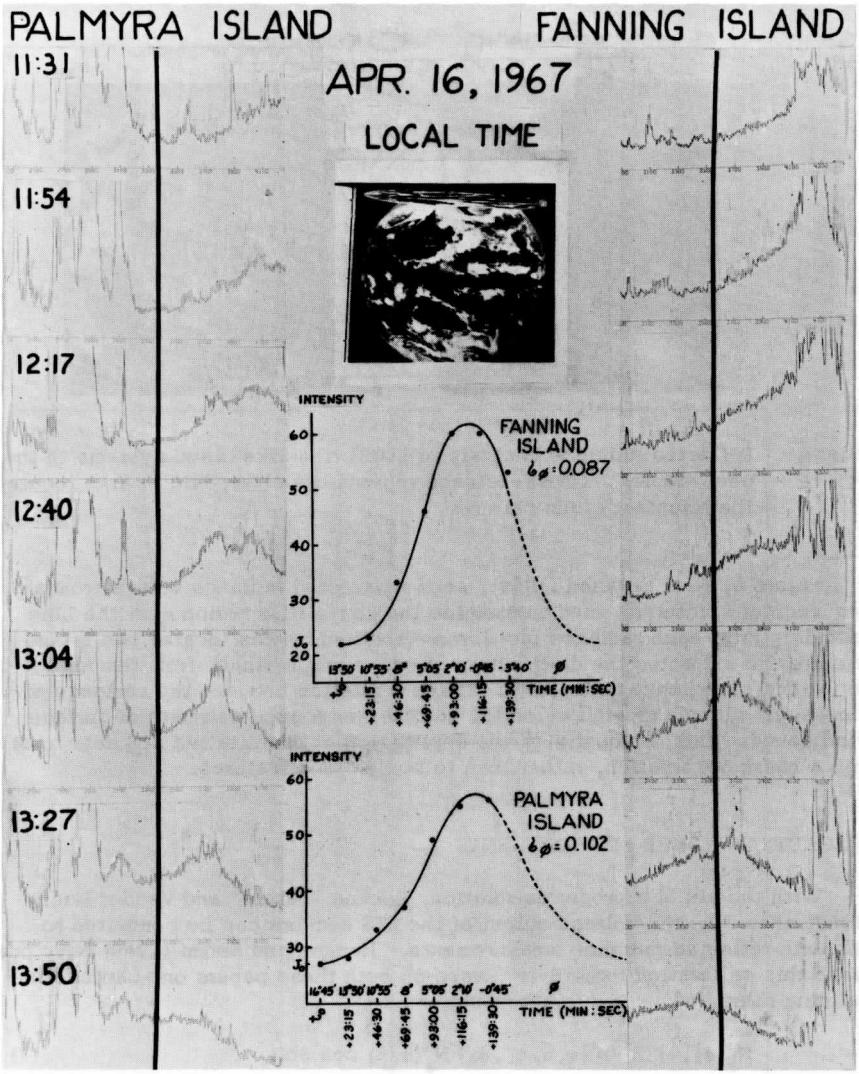

Figure 6. East-west cross-sections of reflected radiance used by Levanon (1969) to study sun glitter.

by the ATS-I sensor. The term $\delta\Omega$ represents the solid angle subtended by the sun at the reflecting surface.

Assuming the incident radiance is only direct solar radiation (no "skylight") we have:

$$\rho'(\gamma, \delta, \phi_1, \phi_2) = \frac{N_r'(\phi_2, \gamma)}{H_\odot' \cos \delta} \qquad (2)$$

with $H_\odot'$ the effective solar constant (irradiance). For illustrative purposes we may assume also that the reflecting surface is a perfectly diffuse reflector (i.e., reflects according to Lambert's law and thus appears as an isotropic surface to an instrument with a fixed instantaneous field of view). In this case, r', the total directional reflectance, equals $\pi\rho'$ and:

$$r' = \frac{\pi N_r'}{H_\odot' \cos \delta} \qquad (3)$$

For ATS-I, $H_\odot' = 192$ watts $\cdot$ m^{-2}, and from Hanson we obtain N_r' from the voltage output of the camera or an equivalent digital count (relative radiance value).

The quantity, r', is sometimes called the "diffuse albedo." Examples of such absolute effective radiance and albedo measurements are shown in Table 1. These are random measurements selected from several ATS-I radiance studies. The values are within accepted limits and thus support the calibration efforts. Aside from extending our knowledge of the reflection characteristics of clouds and surface features, these absolute values can be used in meteorological research on radiation and energy budget problems.

SUMMARY

The spin scan camera experiments on the ATS satellites offer a wide range of meteorological applications using relative and absolute reflected radiance data. Radiance analyses can complement the normal photographic products and add a quantitative nature to studies using ATS measurements. Of course, the application of these data should always exploit the nearly continuous time coverage provided by the experiment. This very great scientific advantage means the end of "snapshot" view limitations in the use of meteorological satellite data.

Scientific studies using radiance measurements are continuing. ATS-III provides the first simple multi-spectral radiance data from meteorological satellites in three spectral regions in and near the visible wavelengths. Cloud

TABLE 1

Example of Absolute Radiance Measurements from ATS

Feature	N_r' ($w \cdot m^{-2} \cdot sr^{-1}$)	ρ' (sr^{-1})	r' (%)
Clouds			
Cb	28.8 - 36	0.15 - 0.22	47 - 69
St	25.6	0.13	42
Ocean	3.4 - 4.8	0.02 - 0.025	6 - 8
Land			
Baja California	9.4	0.05	15
Christmas Island	12	0.07	21
Full Moon	6	0.03	9

height or surface pressure may be inferred from such bispectral observations. The time variation of cirrus clouds above a convective cell is related to the vertical heat and mass transport and perhaps even rainfall. Objective studies of the characteristic distribution of clear and cloud regions within typical meteorological features will provide information needed to plan future satellite sensing systems.

In addition, radiance measurements can be used in objective techniques for inferring winds from cloud motions. These winds are vitally needed to add to our global observing system. In this same area, all wind-measuring techniques and research projects will benefit when reflected radiance data in digital form are used to properly grid and map the ATS photographs. Ausfresser, et al. (1969) and scientists at the National Environmental Satellite Center, ESSA, are developing this capability.

Radiance measurements from geosynchronous satellites will have even more meteorological value when infrared sensors are added to the sensing system. These, too, will provide images, both day and night, and also measurements of cloud height, sea surface temperature, and especially the vertical temperature profile.

ACKNOWLEDGMENTS

Professors Verner E. Suomi and Robert J. Parent of the University of Wisconsin Space Science and Engineering Center were principal investigators for the SSCC experiments. Many individuals associated with NASA's ATS Project Office deserve our thanks. Mr. Eric Smith of the SSCC developed all programs required to use the digitized radiance measurements.

REFERENCES

Ausfresser, H., A. Johnson, and R. Kowalski, 1969: "Computer correction of distortion in ATS-SSCC photographs," Bull. Am. Meteor. Soc., 40, 2, 76-78.

Hanson, K., and V. Suomi, 1969: "The inspace absolute calibration of the ATS-I cloud camera," Weather in Motion, Univ. Wisconsin Press, Madison (in press).

McQuain, R., 1967: "ATS-I camera experiment successful," Bull. Am. Meteor. Soc., 48, 2, 74-79.

Peekna, S., R. Parent, and T. Vonder Haar, 1969: "Possibilities for quantitative radiance measurements in the 450-650 nm region from the ATS-I satellite," Weather in Motion, Univ. Wisconsin Press, Madison (in press).

Sikdar, D., et al., 1969: "Convective transport of mass and energy in severe storms over the United States—An estimate from a geosynchronous altitude" (to be submitted for publication).

Suomi, V., and R. Parent, 1968: "A color view of planet Earth," Bull. Am. Meteor. Soc., 49, 2, 74.

Suomi, V., and T. Vonder Haar, 1969: "Geosynchronous meteorological satellite," J. Spacecraft Rockets, 6, 3.

Vonder Haar, T., et al., 1968: "Phenomenology of convective ring clouds in the tropics derived from geosynchronous satellite observations," Proc. Internatl. Conf. Cloud Physics, Toronto, August.

Warnecke, G., and W. Sunderlin, 1968: "The first color picture of the Earth taken from the ATS-III satellite," Bull. Am. Meteor. Soc., 49, 2, 75-83.

Scanner's note:

This page is blank.

ANALYSIS OF A STRATOSPHERIC HAZE PHENOMENON PHOTOGRAPHED ON THE GEMINI V SPACEFLIGHT

E. Remsberg and J. Weinman

ABSTRACT

A haze layer extending to $\lesssim$ 50 km has been observed above a tropical depression. Densitometric color ratios show the haze to be composed of particles with radii of the order or less than 0.1μ at stratospheric levels. Vertical motion necessary to support these particles is available in tropical storms, and the fine structure of the haze is consistent with models of such storms. The possible relationship between the stratospheric haze layer and the particular storm system at tropospheric levels is discussed.

1. INTRODUCTION

In recent years increased attention has been given to the study of interactions between the troposphere and stratosphere. These interactions have been inferred from measurements of the vertical transport of trace gases and radioactivity (Junge, 1963). Most investigators believe that convection through the tropopause and diffusion are the major transport mechanisms to upper levels. For example, Hesstvedt (1964) shows the source of mesospheric water vapor to be the tropical troposphere; this water vapor is believed to enter the stratosphere through breaks in the tropopause. Although diffusion may be the dominant fair weather vertical transport mechanism, Theon, Nordberg, and Smith (1967) have suggested that dynamical mechanisms, such as cyclonic systems and thunderstorms, also inject material into the stratosphere. U-2 aircraft observations of significant penetrative convection over a severe storm system in Oklahoma (Roach, 1967) show one of these possible particle exchange mechanisms.

Equipment which measures aerosols is frequently sent aloft on rather large balloons which are launched during relatively "fair weather." Lidar probing of stratospheric aerosols is also conducted under relatively cloud-free conditions (Kent, Clemesha, and Wright, 1967). A fair weather sampling bias may therefore exist. The stratosphere may contain a concentration of particles in the proximity of storms that is greater than existing measurements indicate.

Although foul weather observations of vertical transport of material in the upper stratosphere are sparse, recent photographs of tropical storms taken from the Gemini V spaceflight may provide clues to the problem. Photographs (Earth Photographs from Gemini III, IV and V, 1967), shown in Figures 1 and 2, show horizons that exhibit haze structures above the limb. A visual comparison of

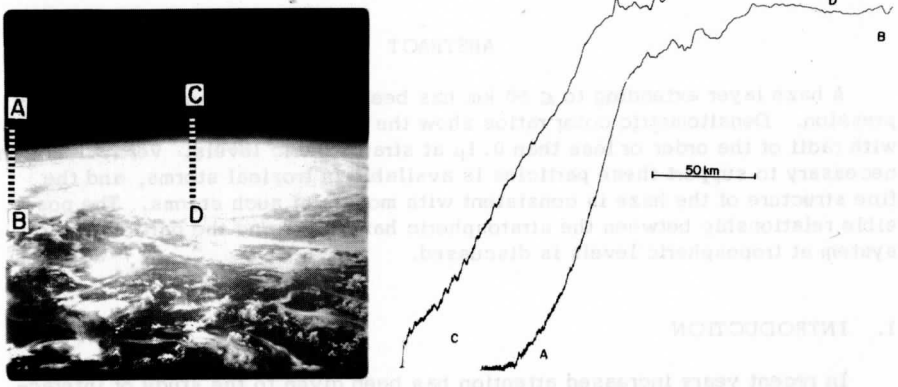

Figure 1. Tropical Depression No. 23 photographed from Gemini V, S-65-45548 (left). This portion of Figure 1 has been reversed to agree with the orientations of the tracings in Figures 5 and 6. Densitometer trace obtained along dashed lines $\overline{AB}$ and $\overline{CD}$ (right).

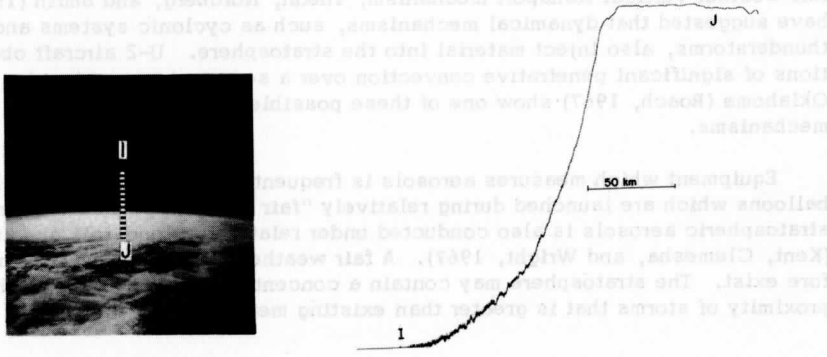

Figure 2. Hurricane Doreen photographed from Gemini V, S-65-45789 (left). Densitometer trace obtained along dashed line $\overline{IJ}$ (right).

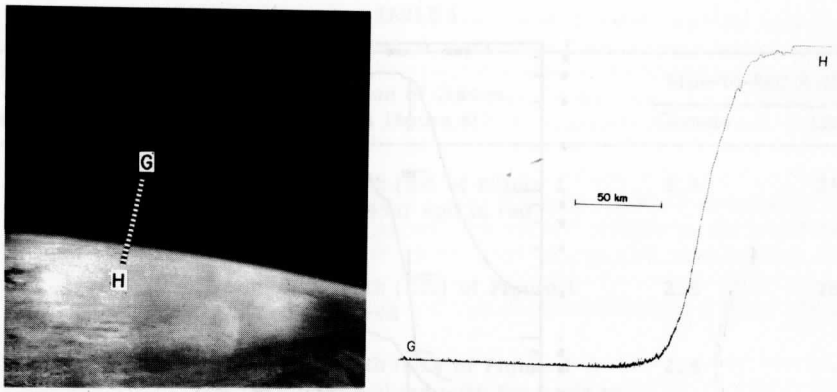

Figure 3. Typhoon Lucy photographed from Gemini V, S-65-45771 (left). Densitometer trace along dashed line $\overline{GH}$ (right).

the photographs with many others suggests that the haze envelopes are somewhat unique. (The horizon of Figure 3 is typical of that seen in many photographs obtained during the flight.) These photographs may therefore provide evidence regarding a possible vertical transport mechanism in the stratosphere.

2. SOURCES OF HAZINESS ON PHOTOGRAPHS

The hazes shown in Figures 1 and 2 appear to extend well into the stratosphere. It is therefore necessary to determine whether the phenomenon might be an artifact. This haziness may be due to several causes which will be considered.

Reflection, due to contamination on the window, is difficult to analyze, because the spacecraft underwent considerable stress during various stages of the flight. The identification sheets for several of the Gemini flights, including Gemini V, indicate that a few photographs such as S-66-54702 have been blurred by contamination on the window. However, the haziness shown in these photographs differed from the haze shown in Figures 1 and 2. In order to emphasize the marked dissimilarity of these effects, the effect of window contamination was simulated by the experimental arrangement described in the Appendix. The results of this experiment are summarized in Figure 4, which shows the output voltage from the photodetector scanned as a function of position in Figure 1. The conditions under which these traces were measured are summarized in Table 1.

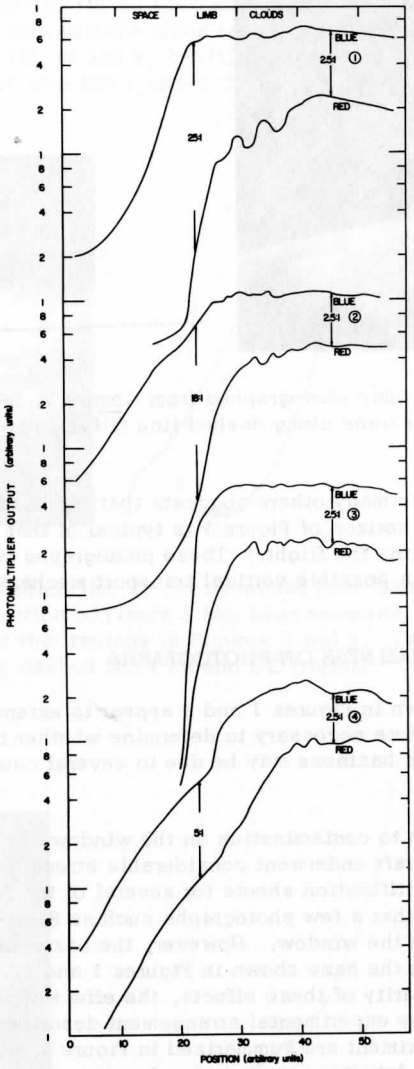

Figure 4. Photometric traces of Figure 1. See Table 1 for description of each trace.

TABLE 1

Designation	Description of Traces (shown in Figure 4)	Blue-to-Red Ratio	
		Clouds	Limb
1	Trace along path ($\overline{AB}$) of Figure 1 in blue ($\lambda = 0.45\mu$) and in red ($\lambda = 0.65\mu$)	2.5	25
2	Trace along path ($\overline{CD}$) of Figure 1 in blue and in red	2.5	18
3	Trace along path ($\overline{CD}$) of Figure 1 for both blue and red with the horizon masked above 20 kilometers	2.5	-
4	Traces along ($\overline{CD}$) with the horizon masked for blue and red. An oiled glass was interposed 10 in. from the detector	2.5	5

Trace 1 (top of Figure 4), measured along ($\overline{AB}$), was obtained to determine the extent of the troposphere. Trace 2, measured along ($\overline{CD}$), was obtained to determine the density of the image of the haze phenomenon both in blue ($\lambda = 0.45\mu$) and red ($\lambda = 0.65\mu$) light. Note that the measurements obtained with the red filter are similar near the limb for traces 1 and 2. Trace 3 was also measured along ($\overline{CD}$); however, the transparency was covered by an opaque sheet which masked the image of the stratosphere. Trace 4 was a repetition of trace 3, except that an oil-film-covered glass plate was interposed between the slide projector and the photodetector. The location of the plate was adjusted so that the blue trace in 4 corresponded to the blue trace in 2. Under these conditions the red trace in 4 did not correspond to the red trace observed in 2. The color of the haziness produced by the oil-covered glass was redder than the haze observed in Figure 1.

Distant clouds observed along the horizon in Figure 1 were obscured by the oil-covered glass plate. A comparison of observations in red for trace 3 and 4 clearly illustrates this effect.

It is possible that a thin film of oil would not appear colorless. However, a uniform colored oil film on the window would only serve to displace the curves described in Section 4 without changing their shape. Since the curves are calibrated in terms of previously measured reflectivities of clouds and the

atmosphere shown in Figure 1, the Q-ratios described in Section 6b would be unaffected by the spectral transmission of uniform contamination on the window. If an oil layer on the window were of varying thicknesses, a color dependency could arise in the image, but the probability that a glob of blue oil existed exactly along the horizon is remote.

Although contamination on the spacecraft window is able to produce haziness in photographs, the dominantly blue color of the observed haze and the appearance of distant clouds observed near the limb of Figure 1 cannot be reconciled with the effects produced by such contaminants. Of several hundred Gemini V photographs only two, Figures 1 and 2, showed this peculiar haziness. The appearance of tropical disturbances in both Figures 1 and 2 is significant.

The optical environment of the Gemini spacecraft has been examined by Newkirk (1967). A debris cloud, caused by the life support system and other vehicle particles, surrounds and follows the capsule, causing incident light to scatter slightly. However, if the haze were due to this debris cloud, this effect would appear on the horizons shown in other photographs taken under similar lighting conditions. Such an effect was not observed.

The intensity of the haze layer might be assumed to be due to molecular Rayleigh scattering of light reflected from cloud layers below the haze. Although few photographs were taken under optical conditions similar to those encountered in Figure 1, Typhoon Lucy, in the dissipation stage shown in Figure 3, was taken under similar lighting conditions. No haze layer is noted in the densitometer analysis. This possible mechanism for the observed effect is thereby eliminated.

Eberhard and fogging effects on the sensitivity of the emulsion (Mees, 1954) may also be neglected, because no haze effect is evident in Figure 3, where light levels were comparable to those encountered in Figure 1.

3. GEOGRAPHICAL LOCATION

The tropical depression No. 23 (TD 23) shown in Figure 1, S-65-45548 (Earth Photographs from Gemini III, IV and V, 1967), was identified with the aid of aircraft reports cited in the Mariner's Weather Log (1966). This tropical depression was located at 21° N, 156° E near the southeastern side of Marcus Island when it was observed at 0125 GMT on August 27, 1965 (Orbit 83). Analyses were also made of photographs of Tropical Storm Doreen, shown in Figure 2, S-65-45789 (Earth Photographs, 1967), located at 17° N, 126° W when observed at 2133 GMT on August 23, 1965 (Orbit 35), and Typhoon Lucy shown in Figure 3, S-65-45771 (Earth Photographs, 1967), located at 37° N, 142° E when observed at 0201 GMT on August 23, 1965 (Orbit 23).

4. PHOTOGRAPHIC CALIBRATION

A Hasselblad camera, model 500-C, with an 80-mm Zeiss Planar lens was used by Astronauts L. G. Cooper and Charles Conrad during their flight. The distance subtended by 0.1 radian, shown in Figure 5, was determined from the known focal length of the camera lens.

The data employed in the present analysis consist of 70-mm third-generation positive transparencies taken from optical masters. The characteristics of the processed film were not available. A calibration procedure was therefore employed to relate the density of the positive transparency to the estimated intensity of light reflected only from features found in the analyzed photograph.

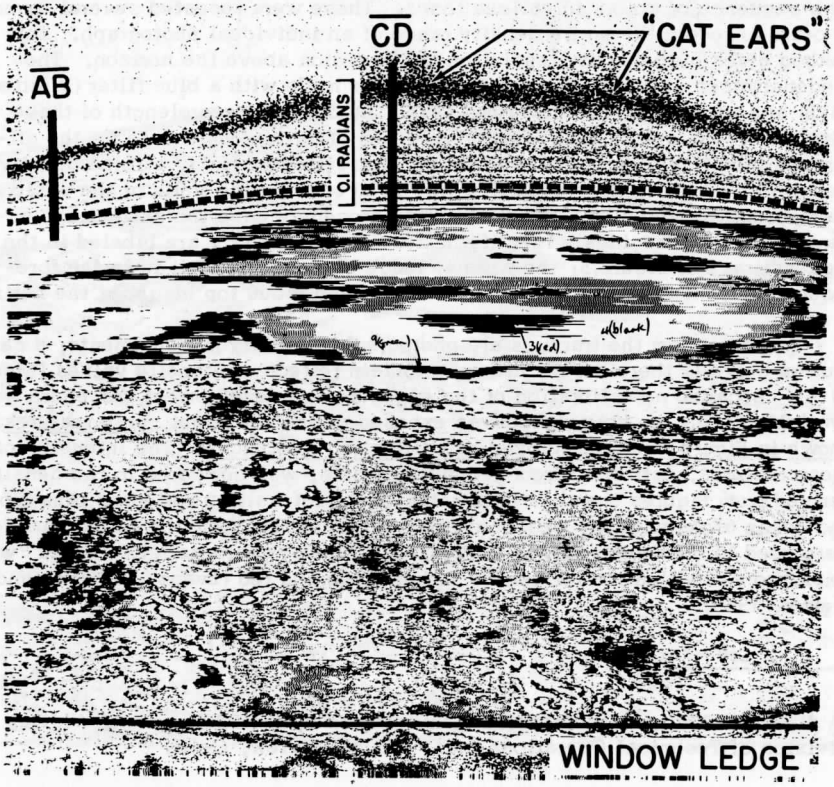

Figure 5. Isodensitrace of Figure 1 for $\lambda = 0.45\mu$.

For image forming light, intensity corrections must be made for vignetting and off-axis effects, which render the corners and edges darker than the centers of photographs. Since the intensity is proportional to the fourth power of the cosine of one-half the aperture angle (Mees, 1954), the measured intensity values were corrected for this effect. Intensity values at the corners of Figure 1 are thus expected to be about 11 percent lower than the intensity at the center of the picture. A densitometer measurement of a Gemini V photograph taken normal to a homogeneous land surface revealed a decrease in intensity between 9 to 12 percent from the center to the corners of the photograph.

Density measurements of the positive transparency were determined with the aid of a Beckman-Whitley color isodensitracer.[1] Figures 5 and 6 show black-and-white photographs of the isodensitracings of Figure 1. The original isodensity tracing shown by Remsberg (1968) represented isopleths of density by a sequence of colors in various tones. These were repeated several times in order to record the entire density range of an individual photograph. This method gives high density resolution in the region above the horizon. The isodensitraces shown in Figures 5 and 6 were made with a blue filter (Wratten #47B) and with a red filter (Wratten #92). The dominant wavelength of these filters is 0.45μ and 0.65μ, respectively. In order to compensate for the difference in optical density of the film for blue reflected light, a fixed density wedge was added to the wedge that was used to make the trace of the positive transparency covered by a red filter. This procedure gave the same range of density for both tracings. Identifying features of Figure 1 are labeled in the isodensitrace of Figure 5; the window ledge of the spacecraft is in the foreground, and the dashed line represents the mean cloud top height at the horizon.

Raw data from the tracings are photographic density measurements; a calibration curve is therefore necessary to obtain reflected intensity values (Mees, 1954). Because no calibration of the exposure and development procedure was available, i.e., no gray wedge was exposed during the flight, only features shown in Figure 1 were employed as calibration references. The intensity of these features, estimated from geophysical data, was compared to the density derived from Figures 5 and 6. Estimates of the intensities reflected from clouds and ocean along with the measured relative intensities from the window ledge were used to obtain the curves in Figure 7. These "characteristic curves" were employed as calibration references in both blue and red (Evans, Hanson, and Brewer, 1953).

---

[1] A direct-recording isophotometer manufactured by the Beckman and Whitley Division of Technical Operations Inc., Mountain View, Calif.

Albedo values for a white cloud as a function of sun angle and wavelength are taken from the Handbook of Geophysics and Space Environments (Elterman and Toolin, 1965) and from the work of Fritz (1958). For a solar zenith angle of 0°, cloud albedo ranges between $0.5 < A_{(\lambda = 0.45\mu)} < 0.6$ and $0.5 < A_{(\lambda = 0.65\mu)} < 0.8$. Albedo figures for the ocean are $A_{(\lambda = 0.45\mu)} \simeq 0.08$ and $A_{(\lambda = 0.65\mu)} \simeq 0.04$.

The albedos of the clouds and ocean (quoted above) were measured from aircraft; however, the reflected intensity can be computed so as to include the

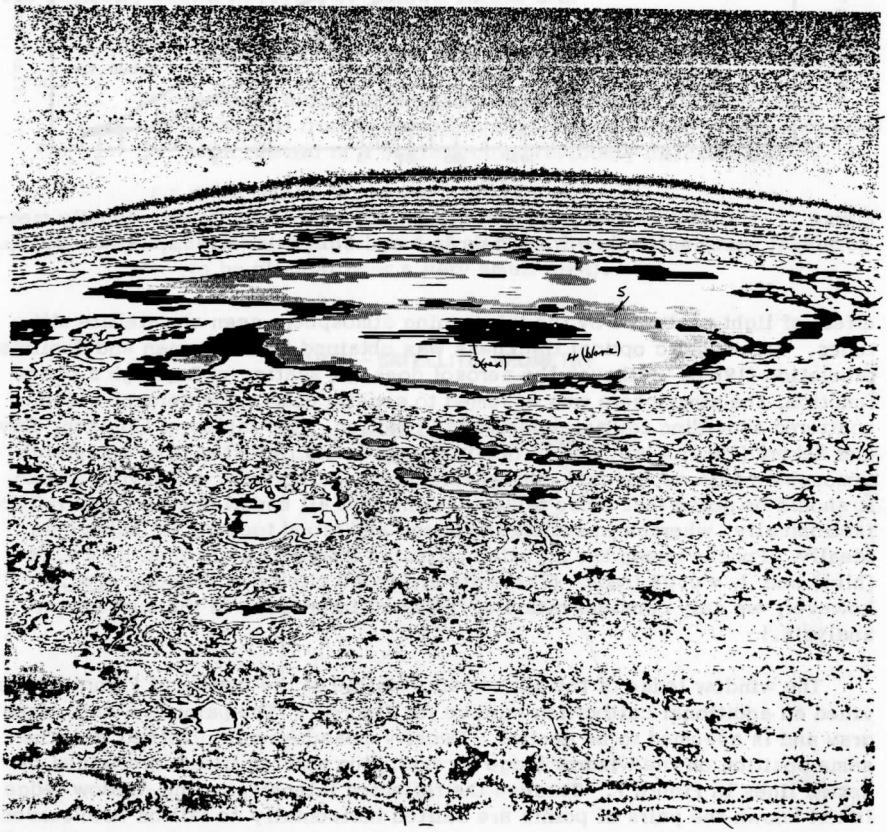

Figure 6. Isodensitrace of Figure 1 for $\lambda = 0.65\mu$.

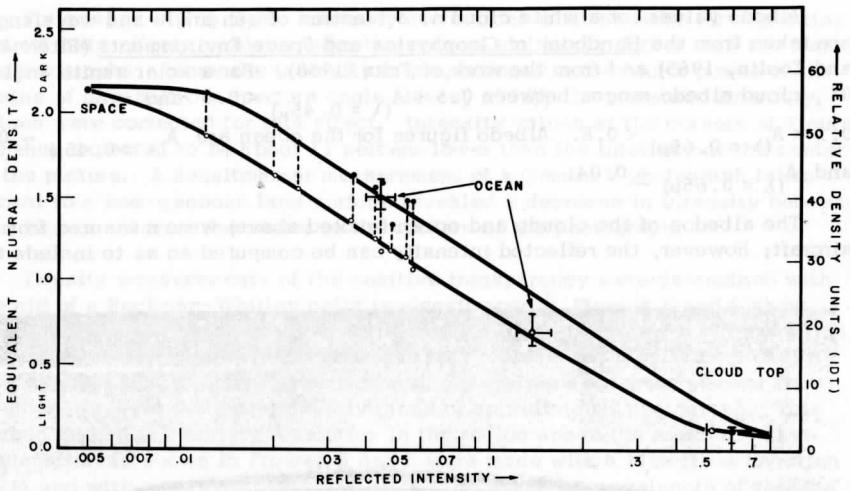

Figure 7. Calibration curve for obtaining reflected intensity from density measurements taken from Figures 5 and 6. (○) $\lambda = 0.45\mu$; (●) $\lambda = 0.65\mu$.

effect of light scattered by the intervening atmosphere seen at satellite altitudes. Atmospheric optical thickness was obtained from Elterman and Toolin's tabulation (1965). Although the aerosol does not scatter by Rayleigh's phase function, the atmosphere was assumed to consist of gas and aerosol which scattered according to Rayleigh's phase function. The tables of Coulson, Dave, and Sekera (1960) were used to obtain the intensity reflected from a Rayleigh atmosphere with appropriate optical thickness and suitable underlying albedo. It should be noted that these tables assume that all underlying surfaces reflect isotropically, whereas in reality the ocean and cloud tops do not behave so ideally. For the ocean the adjusted reflected intensities are then $I_r = 0.14$ (blue) and $I_r = 0.05$ (red). (The units are those cited by Coulson, et al.; however, we only consider ratios of reflected intensities in the subsequent analysis.)

The window ledge of the spacecraft, visible at the bottom of Figure 1, provided an additional calibration surface for Figure 7. The paint is a dark slate gray and is assumed to be neutral. Density measurements obtained from the same position on the window ledge for both blue and red filters are joined by dotted lines in Figure 7. Because the reflected intensity on the window ledge is not known the pairs of points are shifted horizontally to fall on both curves simultaneously. This procedure provides extra points for the determination of the calibration curve in the region where the reflected intensity is comparable to that observed from the haze layer. The curves are admittedly average curves,

and departure from linearity probably exists in the very dark and very bright regions. Possible nonlinear film effects for blue vs. red at light levels of the haze are negligible because density measurements from the gray window ledge differ by a constant factor in the calibration curves.

5. RESULTS AND DISCUSSION

a. Geometrical Analysis

One can determine the height of the haze layer above the storm center from the geometry shown in Figure 8. Known values are:

h = altitude of spacecraft (198 km above mean sea level).

t = vertical height of the haze layer above the horizon as measured from isodensitracings and adjusted to real distances with the aid of a scale factor previously described.

r = mean radius of the earth (6371 km).

a, b = major and minor axes of ellipses fitted to the storm (assumed to be circular over a very small area).

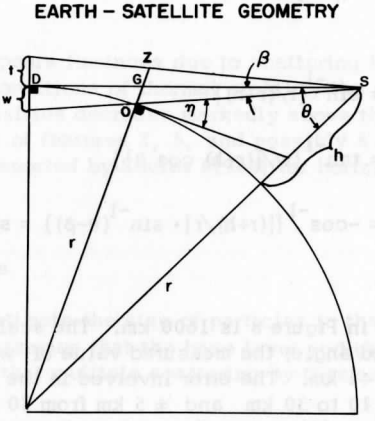

Figure 8. Geometry utilized for determining height of the haze.

w = distance from "center of the storm" to the horizon measured in the same manner as t.

If one assumes that the haze observed at the horizon is located at the storm center, 0, the following two methods may be used to determine the height, $\overline{OZ}$, in Figure 8. The first method requires h, t, r, a, and b as input variables. The ratio b/a represents the eccentricity of an ellipse fitted to the storm center and is a measure of the foreshortening present in the field of view. An alternate method to evaluate this foreshortening uses the measured value w. The development of the equations follows from the trigonometry of the earth-satellite shown in Figure 8 (Remsberg, 1968).

The height of the haze above mean sea level is:

$$\overline{OZ} = \overline{OG} + \overline{GZ} \tag{1}$$

where

$$\overline{GZ} = \frac{(r+h)\cos\{\eta + \sin^{-1}[(r/(r+h)) \cdot \cos\eta]\}\sin\{\tan^{-1}[t/((r+h)\cdot\cos\theta)]\}}{\cos(\beta-\eta)\cos\{\beta-\eta+\tan^{-1}[t/((r+h)\cos\theta)]\}} \tag{2}$$

$$\overline{OG} = \frac{(r+h)\cos\{\eta + \sin^{-1}[(r/(r+h))\cdot\cos\eta]\}\cdot\sin\beta}{\cos(\beta-\eta)\cos\eta} \tag{3}$$

and the angles

$$\theta = \sin^{-1}[r/(r+h)] \tag{4}$$

$$\beta = \tan^{-1}\{w/[(r+h)\cos\theta]\} \tag{5}$$

$$\eta = -\cos^{-1}\{[(r+h)/r]\cdot\sin^{-1}(\theta-\beta)\} = \sin^{-1}(b/a) \tag{6}$$

are shown in Figure 8.

The distance $\overline{DS}$ in Figure 8 is 1600 km. The scale shown in Figure 5 indicates the subtended angle; the measured value of w therefore is 130 km, and the value of t is 44 km. The error involved in the computation of final t values is ± 3 km from 10 to 30 km and ± 5 km from 30 km to higher altitudes. Equation (7) gives $\overline{OZ}$ in kilometers for ranges of t and b/a. Because the horizon is obscured by a cloud layer, values of t are corrected to yield heights above ground level.

$$\overline{OZ} = (0.26 \pm 0.02)t + (48 \pm 9)\text{km} \tag{7}$$

$$6 < t(\text{km}) < 29 \qquad 0.15 \leq b/a \leq 0.21$$

With the aid of a Joyce microdensitometer, traces were scanned perpendicular to the horizon of the earth for several of the photographs (see Figures 1 through 3). Examination of the slope of the intensity as a function of height yields an approximate figure for the thickness of the dense atmosphere (Table 2).

TABLE 2

Height Analysis

Number	Feature	Thickness (km)
1	TD 23 (center) (Figure 1) $\overline{OZ}$	51 ± 5
2	TD 23 (edge) (S-65-45548, Figure 1)	20 ± 3
3	Hurricane Doreen (S-65-45789, Figure 2)	37 ± 5
4	Typhoon Lucy (S-65-45771, Figure 3)	23 ± 3
5	Horizon over Turkey (S-65-45555, not shown)	20 ± 3

The atmosphere appears luminous due to scattering by aerosols and molecules. Under normal conditions of thermal stability the particle concentration and thus the light intensities decrease markedly above the tropopause. The 20 km ± 3 km thickness of features 2, 5, and possibly 4 in Table 2 agrees favorably with values reported by Soules (1963) for horizons photographed from satellites.

b. Brightness Analysis

It is possible to estimate the size of particles in the haze layer as a function of altitude if one assumes that the haze layer and the stratified atmosphere are optically thin such that multiple scattering by these atmospheric constituents can be neglected.

The reflected intensity from the haze, $I_{TH,\lambda}(z)$ (trace $\overline{CD}$ in Figure 5), is given by the expression:

$$I_{TH,\lambda}(z) = I_{E,\lambda}(z) + G_H \cdot P_H(\Theta) \int_z^\infty \beta_H(z') e^{-(1+\frac{1}{\mu})\tau_\lambda(z')} dz' \qquad (8)$$

where

$I_{E,\lambda}(z)$ = intensity scattered by stratified atmosphere in the background. (Trace $\overline{AB}$ in Figure 5.)

G_H = a geometrical shape factor assumed appropriate for the haze visible above the storm.

z' = integration variable, $z < z' < \infty$.

$\beta_{H,\lambda}$ = $\int_0^\infty Q(r',\lambda)\pi r'^2 n(r')dr'$ = the scattering coefficient.

$Q(r',\lambda)$ = the scattering efficiency factor.

$n(r')$ = number of particles with radii between r' and $r' + dr'$.

$\tau_\lambda(z)$ = $\int_z^\infty \beta_\lambda(z')dz'$ = optical thickness.

E = natural aerosol + pure air. (Data derived from trace $\overline{AB}$ of Figure 5.)

H = haze particles.

TH = E + H. (Data derived from trace $\overline{CD}$ of Figure 5.)

μ = cos θ.

θ = zenith angle.

where τ is the optical path from the top of the atmosphere to the depression and τ/μ is the optical path from the depression to the satellite. Values for τ_{λ_1} and τ_{λ_2} as a function of altitude were obtained from the Handbook of Geophysics (1965). The sun is approximately at zenith; thus the light scattered by the haze layer toward the spacecraft by an angle $90° < \Theta < 100°$ is proportional to the scattering phase function $P_H(\Theta)$.

Differentiating equation (8) with respect to z gives

$$\frac{dI_{TH,\lambda}(z)}{dz} - \frac{dI_{E,\lambda}(z)}{dz} = G_H \cdot P_H(\Theta) \cdot \beta_{H,\lambda}(z)\, e^{-(1+\frac{1}{\mu})\tau_\lambda(z)} \qquad (9)$$

The intensity gradients in equation (9) were measured at $\lambda_1 = 0.45\mu$ and at $\lambda_2 = 0.65\mu$. If the phase function $P_H(90°)$ (Deirmendjian,1964) and the geometry factor G_H are relatively independent of wavelength, the ratio of quantities defined in equation (9) renders it feasible to eliminate these quantities. If the size distribution of the particles is monodisperse, it follows that

$$\frac{Q(r,\lambda_2)}{Q(r,\lambda_1)} = \frac{\frac{dI_{TH,\lambda_2}(z)}{dz} - \frac{dI_{E,\lambda_2}(z)}{dz}}{\frac{dI_{TH,\lambda_1}(z)}{dz} - \frac{dI_{E,\lambda_1}(z)}{dz}} e^{-(1+\frac{1}{\mu})[\tau_{\lambda_2}(z) - \tau_{\lambda_1}(z)]} \qquad (10)$$

Values of density along traces $\overline{AB}$ and $\overline{CD}$ are converted to reflected intensity from the calibration curves in Figure 7. Reflected intensities are adjusted to compensate for off-axis effects, and smooth curves are then fitted to the adjusted values. The intensity gradient from these curves is evaluated as a function of z for both traces $\overline{AB}$ and $\overline{CD}$ in blue and red. Ratios of the differences of the gradients yield the unknown Q-ratios by equation (10).

A plot of the Q-ratios vs. altitude is shown in Figure 9. A mean Rayleigh value of 0.23 is shown for comparison,and the error represented is for one standard deviation. An "effective particle size" can be estimated if the particles are assumed to have an index of refraction of 1.5. For a monodisperse size distribution, the mean Rayleigh Q-ratio, 0.23, implies that the "particle radius" $r \leq 0.10\mu$, and the maximum possible Q-ratio, 0.40, implies that $r \leq 0.16\mu$. The results shown in Figure 9 serve to strengthen the argument against the haze being window contamination illuminated by direct sunlight or light reflected from cloud layers below the satellite. Values obtained in the above analysis would have to exceed four standard deviations before attaining the Q-ratio of 1.0, which would characterize the reflection of "white" light from window contamination. In order for the Q-ratio to appear "blue" as measured, the distribution of particle sizes would necessarily be of the order of or less than 0.1μ in radius. It is improbable that window contaminants would be subjected to a mechanism which would discriminate in favor of such small particles.

The terminal velocity, computed by the method of Millikan (1947), for particles of $r < 0.16\mu$ radius, is $< 9 \times 10^{-4}$ mb/hr (Remsberg, 1968).

It is possible in principle but difficult in practice to infer the particle density distribution as a function of height because the haze geometry is in doubt. Furthermore, the solution of the transfer equation for any but planar geometry is difficult to obtain. However, a very crude calculation suggests that the scattering coefficient $\beta_H(30\text{ km}) \simeq 10^{-2}\text{ km}^{-1}$. The procedure described above removes dependence on the unknown geometry factor, G_H, which cancels in equation (10).

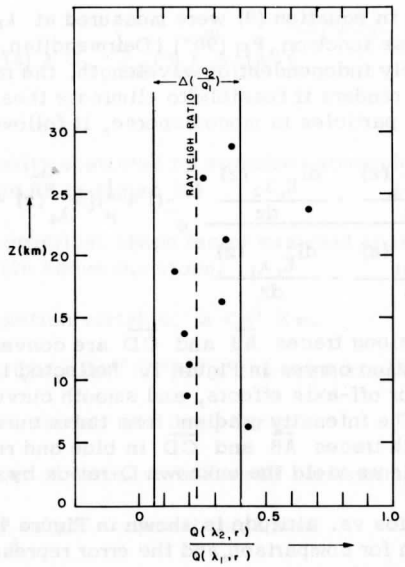

Figure 9. Ratio of scattering efficiency factors derived from equation (10) as a function of altitude.

c. Meteorological Analysis

A time series analysis of the vertical wind field was computed for the period August 23-30 by the method of Bellamy (1949) in order to ascertain the state of TD 23 when it was photographed. This kinematic method yields values of space-mean vertical pressure velocity, $\bar{\omega}_k$, from the divergence of the horizontal wind field. The divergence was computed from data obtained from the 3-station network, Guam Island, Wake Island, and Marcus Ialand, which surrounded the storm TD 23 during the period August 23-30, 1965.

Results of the computations showing isopleths of vertical motion in mb/hr as a function of time are displayed in Figure 10. One notes that the upward motion was near its maximum value on August 27, when Figure 1 was photographed. As a result of the assumptions inherent in the kinematic method, values of vertical motion above the 600-to 500-mb level, shown by dashed lines, are considered of questionable magnitude. An independent confirmation of the existence of particles which were raised to at least the 100-mb level is evident in the June 1966 Nimbus II observations of Hurricane Alma in the 14 to 16μ CO_2 band (Nordberg, et al., 1966). These particles were evident in the maturing

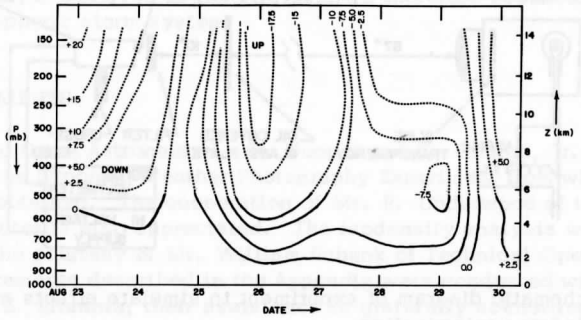

Figure 10. Time series analysis of the vertical wind field, $\bar{\omega}$ (mb/hr).

stage; however, they were no longer evident at this altitude in the decaying stage. The general absence of haze in photographs of most storms suggests that the haze may only appear at a relatively early stage in the development of tropical storms. This seemingly preferential appearance of the haze may provide clues as to why the haze appears so high over this mere depression and not over actual hurricanes photographed while they were in later stages of their development.

The mean vertical velocities shown in Figure 10 exceed $(8 \pm 1) \times 10^{-4}$ mb/hr, the terminal fall velocities of 0.1μ radius particles, by as much as three orders of magnitude at the time of the photograph in Figure 1. The vertical motion is therefore clearly sufficient to support the haze particles in the lower stratosphere.

Tropical Storm Doreen, S-65-45789 (Earth Photographs, 1967), in Figure 2 also exhibits a stratospheric haze phenomenon to a lesser degree than TD 23. However, no meteorological data were available from the eastern Pacific region.

Cirrus with high vertical wisps, such as those in the foreground of Figure 1, were also observed by Roach (1967) in his analysis of a severe storm which penetrated into the stratosphere. The association of the haze phenomenon with the circulation pattern present in Figure 1 also seems to be supported by Estoque's analysis (1963), which indicates that vertical motion ascends near the edges of the storm. The so-called "cat ears" feature above the storm center in the isodensitracing (Figure 5) appears to be consistent with Estoque's storm model. Whether the influence of the storm upon the level of the haze layer is direct upwelling or is indirectly related to the isentropic surface profile of the "heat island effect" (Koteswaram, 1967) cannot be determined.

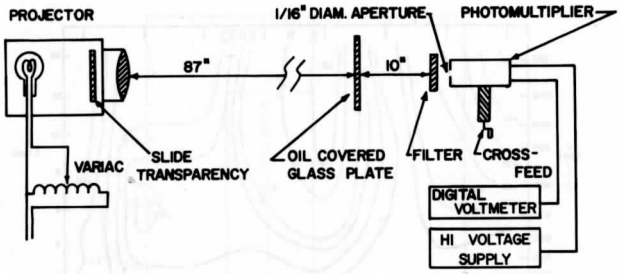

Figure 11. Schematic diagram of experiment to simulate effects of probable window contamination.

7. CONCLUSIONS

In the analysis of the phenomenon in Figure 1, the following facts are brought out:

1. Haze layers are apparent on only two photographs, Figures 1 and 2, taken on the Gemini V flight. The haziness in Figure 1 showing a tropical depression is more blue than the haziness that could be produced by contamination on the spacecraft window.

2. If contamination on the spacecraft window would have been sufficiently thick to produce the observed haziness, the distant clouds observed near the limb of Figure 1 would also have been obscured. Such was not the case.

3. The haze observed above the tropical depression seems to extend to $z \lesssim 50$ km.

4. A color densitometric calculation suggests that the haze consists of particles of the order of or less than 0.1μ at stratospheric levels. This particle size is comparable to that measured in the stratospheric aerosol.

5. Vertical velocities required to support such particles seem readily available in the lower stratosphere above tropical depressions. On the basis of only three tropical storm systems observed, the haze seems to appear at a particular stage in the development of such storms.

6. The "cat ear" structure of the haze is consistent with Estoque's model of the vertical motion field associated with tropical disturbances. This structure also agrees qualitatively with the isentropic profile of the "heat island effect" for tropical storms.

The haze layer observed in the stratosphere therefore seems to be associated with the tropospheric storm system.

ACKNOWLEDGMENTS

We wish to thank Astronauts L. G. Cooper and C. Conrad, Jr., for their completion of the Synoptic Weather Photography Experiment from which these pictures were obtained. The cooperation of Mr. R. Underwood of the Manned Spaceflight Center is also appreciated. The isodensity analysis was made possible through the courtesy of Mr. William Schenk of Technical Operations, Inc., and the measurements described in the Appendix were conducted with the cooperation of Mr. E. Eloranta; their assistance is gratefully acknowledged. The comments of Mr. Stanley Soules and Drs. Frank Sechrist, Donald Johnson, Carl Mateer, and Julius London were also most helpful.

REFERENCES

Bellamy, J. C., Feb. 1949: "Objective calculations of divergence, vertical velocity and vorticity," Bull. Am. Meteor. Soc., 30: 2, 45-49.

Coulson, K. L., J. V. Dave, and Z. Sekera, 1960: Tables Related to Radiation Emerging from a Planetary Atmosphere with Rayleigh Scattering, Univ. of Calif. Press.

Deirmendjian, D., Feb. 1964: "Scattering and polarization properties of water clouds and hazes in the visible and infrared," Appl. Optics, 3: 2, 187-196.

Earth Photographs from Gemini III, IV and V, 1967: NASA SP-129, U.S. Gov. Print. Off., Washington, D.C.

Elterman, L., and R. B. Toolin, 1965: Handbook of Geophysics and Space Environments, Shea Valley, ed., McGraw-Hill Book Co., Inc., New York, 7-1 to 7-5.

Estoque, M., June, 1963: "Some numerical studies of tropical cyclones," Proc. 3rd Tech. Conf. Hurricanes & Tropical Meteor., Geofysica Internacional, Mexico City, 133-150.

Evans, R. M., W. T. Hanson, and W. L. Brewer, 1953: Principles of Color Photography, John Wiley and Sons, Inc., New York, 454-488.

Fritz, S., Feb. 1958: "Absorption and scattering of solar energy in clouds of 'large water drops'—Part II," J. Meteor., 15: 1, 51-58.

Hesstvedt, E., Feb. 1964: "On the water vapor content in the high atmosphere," Geofysiske Publikasjoner of Oslo, 25: 3, 1-18.

Junge, C., 1963: Air Chemistry and Radioactivity, Academic Press, New York, 183-203.

Kent, G. S., B. R. Clemesha and R. W. Wright, Feb. 1967: "High altitude atmospheric scattering of light from a laser beam," J. Atmos. Terrestrial Phys., 29: 2, 169-181.

Koteswaram, P., Aug. 1967: "On the structure of hurricanes in the upper troposphere and lower stratosphere," Month. Weather Rev., 95: 8, 541-564.

Mariner's Weather Log, May 1966: 10: 3, 73-78.

Mees, K. C. E., 1954: Theory of the Photographic Process, rev. edn., Macmillan Co., New York, 1031 and 1038.

Millikan, R. A., 1947: Electrons (+ and -), Protons, Photons, Mesotrons, and Cosmic Rays, Univ. Chicago Press.

Newkirk, G., Jr., July 1967: "The optical environment of manned spacecraft," Planetary and Space Sci., 15: 7, 1267-1285.

Nordberg, W., et al., Nov. 1966: "Preliminary results from Nimbus II," Bull. Am. Meteor. Soc., 47: 11, 857-872.

Remsberg, E. E., June 1968: Analysis of a Stratospheric Haze Phenomenon Photographed on the Gemini V Space Flight, M. S. Thesis, Dept. Meteor., Univ. Wisconsin, Madison.

Roach, W. T., July 1967: "On the nature of the summit areas of severe storms in Oklahoma," Quart. J. Roy. Meteor. Soc., 93: 397, 318-336.

Soules, S., Nov. 1963: "Spectral reflectance photography of the Earth from Mercury Spacecraft MA-8," Meteor. Satellite Lab. Rept. No. 22, U.S. Dept. Commerce, Washington, D.C.

Theon, J. S., W. Nordberg, and W. S. Smith, July 1967: "Temperature measurements in noctilucent clouds," Science, 157: 3787, 419-421.

APPENDIX

Studies have been made on the composition and optical effects of contamination on the Gemini spacecraft windows. The principal contaminant was a silicone potting compound, DC-325, which ablated from the nose fairing and collected as a silicone-oil film on the spacecraft window.

An experiment was conducted to simulate the effect of a silicone-contamination film upon light transmitted through a window from an exterior horizon view. The schematic diagram shown in Figure 11 illustrates the experiment. A third-generation positive transparency of TD 23 (see Figure 1), was mounted as a 3-1/4-in. by 4-in. slide. It was then projected by a Beseler #3620 lantern slide projector using a magnification of approximately 12. Heating caused by the lamp was reduced by wiring the bulb to a Variac. This preserved the lantern slide during the experiment. Light detection was achieved by an RCA #931A photomultiplier tube, covered by a 1/16-in. diameter aperture, mounted on a cross-feed mechanism at the projected image. The output of the photomultiplier tube was monitored with a digital voltmeter that could be read to three significant figures. Wratten filters, #92 (red) and #47B (blue), such as the ones used in the other densitometric tracings, were placed in front of the detector as indicated. The response of the photomultiplier tube is wavelength dependent, but we are only interested in the ratios of the photomultiplier output for blue vs. red. Therefore, no attempt was made to convert the output to photographic densities. The distance between the lens of the projector and the detector was 97 in.

Using appropriate marks on the transparency, scans were conducted along traces $\overline{AB}$ and $\overline{CD}$ shown in Figure 5. This was done in red and in blue for both paths. The horizon above 20 kilometers was then occulted with an opaque shield on the slide. Traces were repeated in red and blue for the path $\overline{CD}$. In order to simulate the smearing effects of a silicone-oil film on the image, a high-quality 9-in. by 9-in. piece of plate glass was coated with a thin film of DC-704 clear silicone oil. The glass plate was inserted in the field of view 10 in. from the detector; this distance was adjusted empirically so that the diffused horizon matched the horizon shown in Figure 1 when the blue filter covered the photomultiplier. Again the path $\overline{CD}$ was scanned in both colors. The traces are described in Table 1, and the results are shown in Figure 4.

Scanner's note:

This page is blank.

MECHANISMS OF LARGE-SCALE WAVE PROPAGATIONS THROUGH THE TROPICS

J. Bennett and J. Young

ABSTRACT

The dynamical effects which influence the coupling of large-scale atmospheric disturbances between latitudes are studied in a one-layer model of the tropical atmosphere. Attention is focused upon the response of the tropics to propagating waves in middle latitudes, with particular attention being given to the influence of the zonal shear flow upon the wave motions.

It is found that most westward-moving waves propagate most freely and often exhibit quasi-resonance; they are thus able to excite significant disturbances even across the equator. An exception is the wave moving slowly westward which is abruptly absorbed at a critical latitude where the wave speed is equal to the speed of the mean easterly flow. Eastward-moving waves in general do not propagate very far into the tropics before being gradually attenuated.

INTRODUCTION

The observations of well-organized wave motions propagating in the equatorial atmosphere (Yanai, 1966) have spurred many theoretical works. Matsuno (1966) treated the theory of free waves on an equatorial beta-plane with no shear in the basic current. Recent theory on possible sources of energy for such waves emphasizes the possibility of forcing by processes in mid-latitudes. Charney (1963) argues that motion in the tropics should be even more quasi-horizontal and uncoupled in the vertical than the mid-latitude motions, and thus subject to lateral forcing.

Mak (1969) investigated the lateral forcing theory quantitatively with a semi-empirical model and found that the observed flow statistics at 30° N could explain the internal statistics of the tropics without internal sources of heat or moisture. Thus, the possibility of large-scale waves propagating into the tropics certainly bears further investigation.

The dynamics of wave propagation in a shear flow arise in many atmospheric problems. Charney and Drazin (1961) investigated the possibility of planetary waves propagating into the upper atmosphere and found that the mean winds could act to reflect waves and thus trap the energy in the troposphere. Booker and Bretherton (1967) investigated the vertical propagation of gravity waves in a shear flow and found that at the level where the horizontal trace velocity of the wave is equal to the mean wind speed the waves are absorbed. At this point the wave equation is singular, and some confusion arose over whether the wave is reflected or absorbed. In terms of group velocity, Bretherton (1966) was able to show that a wave packet traveling toward the critical level would never actually reach it and would thus be effectively absorbed.

The present study attempts to fill some gaps left by two earlier studies. The equations used here are similar to the equations of both Matsuno (1966) and Mak (1969). They reduce to Matsuno's in the case with no basic current. Mak's model had two layers in pressure coordinates and was much more complicated, but it was unsuitable for investigating the mechanisms of latitudinal energy transfer.

DERIVATION OF THE WAVE EQUATION

Let us consider a layer of an incompressible fluid with a free surface, the shallow water model, which has a mean zonal velocity varying with the meridional coordinate. The two horizontal equations of motion and the continuity equation are:

$$\frac{\partial u}{\partial t} + U\frac{\partial u}{\partial x} + v\frac{dU}{dy} - fv + \frac{\partial \phi}{\partial x} = 0 \tag{1}$$

$$\frac{\partial v}{\partial t} + U\frac{\partial v}{\partial x} + fu + \frac{\partial \Phi}{\partial y} = 0 \tag{2}$$

$$\frac{\partial \phi}{\partial t} + U\frac{\partial \phi}{\partial x} + v\frac{d\Phi}{dy} + gh\left(\frac{\partial u}{\partial x} + \frac{\partial v}{\partial y}\right) = 0 \tag{3}$$

where u and v are velocities in the x and y directions, and ϕ is the geopotential. Small letters denote perturbation quantities, and capital letters refer to the base state. H is the mean height of the fluid. The coriolis parameter, f, is assumed to vary linearly in the meridional direction:

$$f = \beta y$$

where $\beta = df/dy$ is evaluated at the equator. From the fact that the base state is only composed of a zonal velocity and only varies in the meridional direction, it follows that it is geostrophic:

$$\frac{d\phi}{dy} = -fU$$

For convenience we nondimensionalize by taking

$$T = (1/\sqrt{gH}\beta)^{1/2} \qquad L = (\sqrt{gH}/\beta)^{1/2}$$

The equations now are:

$$\frac{\partial u}{\partial t} + U\frac{\partial u}{\partial x} + v\frac{dU}{dy} - yv + \frac{\partial \phi}{\partial x} = 0$$

$$\frac{\partial v}{\partial t} + U\frac{\partial v}{\partial x} + yu + \frac{\partial \phi}{\partial y} = 0$$

$$\frac{\partial \phi}{\partial t} + U\frac{\partial \phi}{\partial x} - yUv + \frac{\partial u}{\partial x} + \frac{\partial v}{\partial y} = 0$$

Assuming solutions of the form

$$u = u(y)e^{i(kx-kct)}$$

$$v = v(y)e^{i(kx-kct)}$$

$$\phi = \phi(y)e^{i(kx-kct)}$$

The equations reduce to:

$$ik(U-c)u + v\frac{dU}{dy} - yv + ik\phi = 0$$

$$ik(U-c)v + yu + \frac{d\phi}{dy} = 0$$

$$ik(U-c)\phi - yUv + iku + \frac{dv}{dy} = 0$$

By solving the first equation for u and substituting in the last two equations:

$$ik(U-c)v + \frac{y}{ik(U-c)}\left(yv - ik\phi - v\frac{dU}{dy}\right) + \frac{d\phi}{dy} = 0 \qquad (4)$$

$$ik(U-c)\phi - yUv + \frac{1}{U-c}\left(yv - ik\phi - v\frac{dU}{dy}\right) + \frac{dv}{dy} = 0 \qquad (5)$$

Now, by differentiating equation (5) with respect to y and substituting for $\frac{d\phi}{dy}$ from equation (4) and for ϕ from the undifferentiated form of equation (5), one can obtain a single equation for v:

$$\frac{d^2v}{dy^2} + \frac{dv}{dy}\left[-yU - \frac{2(U-c)}{(U-c)^2-1}\frac{dU}{dy}\right] + v\left\{k^2(U-c)^2 - k^2 + \frac{1}{(U-c)} - y^2 - U - \frac{1}{(U-c)}\frac{d^2U}{dy^2}\right.$$

$$+\frac{1}{(U-c)^2}\left(\frac{dU}{dy}\right)^2 + \frac{Uy^2}{(U-c)}$$

$$\left.+\frac{1}{(U-c)^2-1}\frac{dU}{dy}\left[yU(U-c) + y\frac{U}{(U-c)} + \frac{\frac{dU}{dy}}{(U-c)^2} + \frac{dU}{dy} - 2y\right]\right\} = 0 \qquad (6)$$

If the mean velocity is set identically equal to zero, this equation reduces to Matsuno's equation (6) for which the free modes are:

$$e^{-y^2/2}\, H_n(y)$$

where H_n is the n-th order Hermite polynomial. Although very general methods of obtaining solutions for equation (6) are available, they are time-consuming and not very instructive. We will limit ourselves to heuristic arguments and qualitative analyses of some numerical attempts at obtaining solutions.

The behavior of the solution is highly dependent on the sign of the coefficient of v. The coefficient of $\frac{dv}{dy}$ is unimportant for realistic flow states in the earth's atmosphere, and the equation can be transformed into an equation with very similar solutions which does not contain this term.

When R, the coefficient of v, is positive and varies slowly with y, a "WKB" approximation, analogous to ray tracing in optics, is appropriate. Oscillatory solutions are possible with "local wave number" $\sqrt{R}$.

Such solutions will be referred to as propagating, although it should be remembered that this refers to a wave-like form for the envelope of the latitudinal structure rather than to a wave pattern traveling from one latitude to another. As R changes with y, one may think of processes of partial reflection taking place. When R becomes zero and changes sign (i.e., possesses a turning point), the solutions give wave "trapping" in the region $R > 0$, and

tend to damp for $R < 0$, unless R becomes positive again, in which case the wave has "tunneled" through the region of negative R.

At the "critical latitude" the coefficient goes to positive infinity indicating that the wavelength of simple traveling waves would go to zero and that therefore the trace velocity in the y-direction would go to zero. When the group velocity approaches zero in such a way that the energy can never actually reach the critical point in a finite amount of time, the wave is said to be absorbed (Bretherton, 1966).

Equation (6) was approximated by a finite difference analog encompassing 19 grid points between approximately 30°N and 30°S. We simulated mid-latitudinal forcing of the tropics by setting $v = 1$ at the northern boundary and $v = 0$ at the southern boundary. The finite difference analog was solved for various values of k, c, $R(y)$, and width of boundaries. In the process, the values of the coefficient $R(y)$ were printed out in order to analyze the results qualitatively according to the concepts of propagation, reflection, and absorption.

By arbitrarily setting the boundary conditions and fixing ω (the frequency) and k, we confine ourselves to looking at the asymptotic solution to the initial value problem that is generated by starting a wave traveling along the boundary and keeping it there until the whole tropical atmosphere is pulsing at its frequency and wavelength. By ignoring the transient responses to the forcing at the boundary, we are neglecting the way in which the energy initially enters the tropics, preferring to look at the tropics much later when the system is statistically steady. Again we refer the reader to Booker and Bretherton (1967) for consideration of the related initial value problem. The southern boundary condition is set equal to zero for two reasons: (1) It allows attention to be focused upon the interesting problem of wave propagation from one hemisphere to the other, and (2) The response when the southern boundary condition is not zero can be added to that found here (where it is zero) since the governing equation (6) is linear.

For our base state we assume a parabolic zonal wind that is symmetric about the equator. This is a fair approximation to the average conditions in the tropics and is easy to treat both numerically and analytically:

$$U = py^2 + Q$$

If we take $\sqrt{gh} = +40$ m/sec, appropriate values for Q and P are -0.03 and 0.004, respectively, giving a 1.2 m/sec easterly wind at the equator and 0.3 m/sec westerly wind at $y = 3.0$ that corresponds to roughly 30°N. We will refer to this as basic flow A. Basic flow B corresponds to Q and P increased from their values in current A by the factor 8.

Figure 1 gives the coefficient of v in equation (6) as a function of c and y for k = 2.1 (corresponding to a wavelength of approximately 3000 km if $\sqrt{gH}$ = 40 m/sec). Four distinct regions are apparent:

1. For large positive c (eastward moving waves which compose the bulk of the energy of mid-latitudes), the coefficient is negative, which implies damped solutions, and hence the waves are confined to mid-latitudes.

2. For small negative c, the coefficient is first negative and later positive, which implies the possibility of "tunneling" through the nonpropagating region.

3. For any wave speed in the range of the mean wind speed at some latitude there is a critical point, which implies absorption of wave energy before the equator is reached.

4. For large westward wave speeds there is no critical point, and the wave is free to propagate into the tropics and across the equator.

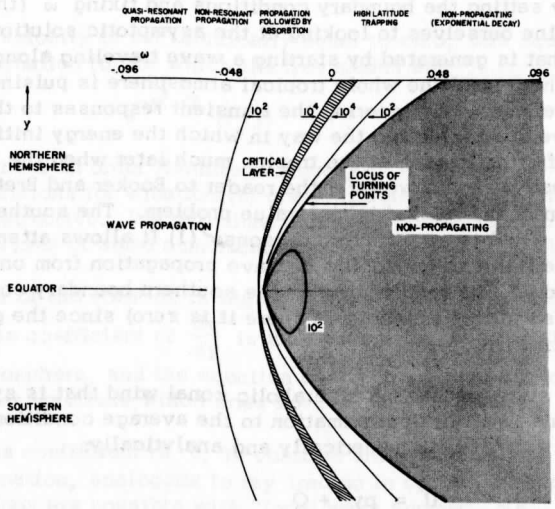

Figure 1. Wave propagation coefficient R as a function of wave phase, speed, and latitude for the case with basic zonal current A. Nonpropagating regions (R < 0) are denoted by stippled areas. Hatched region for propagating waves (R > 0) indicates region of critical layer absorption. Thin solid lines indicate magnitudes of R.

FREE WAVES

When the mean velocity is set identically equal to zero, equation (6) reduces to:

$$\frac{d^2v}{dy^2} + (\omega^2 - k^2 - \frac{k}{\omega} - y^2)v = 0$$

The free waves are the eigensolutions to this equation and satisfy the homogeneous boundary conditions. In the infinite domain the solutions are $e^{-y^2/2}$ multiplied by Hermite polynomials and the eigenvalues are:

$$\alpha = \omega^2 - k^2 - \frac{k}{\omega} = 2n + 1$$

where $\omega = ck$, $n = 0, 1, 2, \ldots$, etc., and n is the order of the polynomial. The value of α determines three roots, two corresponding to gravity waves and one to a Rossby wave. As Matsuno pointed out, the low-order modes (small n) are trapped near the equator and are relatively insensitive to distant boundaries. However, the higher order modes found by Matsuno would be affected by the finiteness of the real earth.

For this reason the eigenvalue problem corresponding to $v = 0$ at $y = \pm 10.0$ was studied by finding the eigenvalues and the eigenfunctions of the finite-difference analogs of equation (6) with $U = 0$. The values $y = \pm 10.0$ correspond roughly to the north and south poles, respectively.

Figure 2 exhibits some eigenvalues which are symmetric about the equator. We see that each mode is centered near a latitude approximately as $\alpha^{1/2}$ so that the low modes are trapped near the equator. The higher modes are trapped in a latitudinal band centered at mid-latitudes, and it can be shown that the lowest frequency (for large α) reduces to the classical mid-latitude Rossby wave frequency. Thus we see that the model suggests little natural coupling between the Rossby waves of high and low latitudes, even in the absence of a basic zonal flow.

FORCED WAVES IN THE TROPICS

These results for $\alpha = 6.04$ do suggest the possibility of coupling across the subtropical latitude belt. This was investigated further by specifying non-zero values of v at the boundaries $y = \pm 3.0$, thus modeling the effects upon the tropical atmosphere of a wave moving along higher latitude circles. Mathematically, we then examine solutions of equation (6) which are "forced" by the boundary conditions, with k and c specified.

Since the forced response of a system is related to its free modes, additional numerical eigensolutions were found for this case with boundaries at

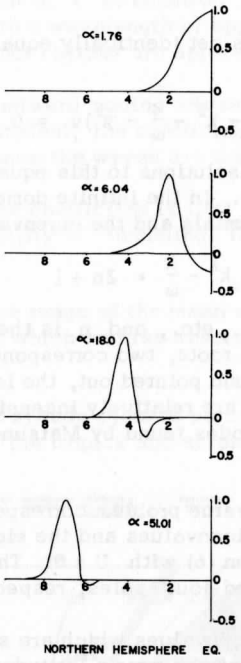

Figure 2. Latitudinal profiles of northward motion v(y) corresponding to symmetric free modes obtained numerically for the case with no basic zonal current. Distance is in nondimensional units. Amplitudes are arbitrary. α is indicative of the latitudinal mode number.

$y = \pm 3.0$. It was found that the solutions for smallest α were not changed much by the closer boundaries but that the higher modes corresponded to rapid oscillations in v throughout the whole tropical domain.

The forced solutions (with $U = 0$) are shown as solid lines in Figure 3 for various values of phase speed (and hence frequency and α). We see that the ability of the motions to penetrate into the Southern Hemisphere depends strongly upon the wave speed (in the cases shown, all are to the west). The maximum response at all latitudes is found for waves whose wavelength and speed nearly equal the values for an eigenmode of the system. Such westward-moving waves are thus "quasi-resonant" and represent the strongest excitation of the tropics by the mid-latitudes. Figure 3 shows that the latitudinal forms

of these quasi-resonant waves closely resemble those of the corresponding free waves. In the case $c = -0.19$, wave trapping in low latitudes actually produces a larger equatorial response than at the boundary.

We now turn to consideration of the wave propagation characteristics in the presence of a basic zonal flow with shear—basic flow A. Figure 4 illustrates the importance of the direction of wave movement for two waves moving at the same speed. The speeds are here chosen to lie outside the range associated with "critical" or "turning point" latitudes. While the westward-moving wave ($\omega = +0.17$) propagates freely and with large amplitude, the eastward-moving wave does not propagate and simply decays quickly to zero.

Other features predicted by Figure 1 can be illustrated for basic flow B. Figures 5 and 6 show the wave response for successively larger speeds of west-

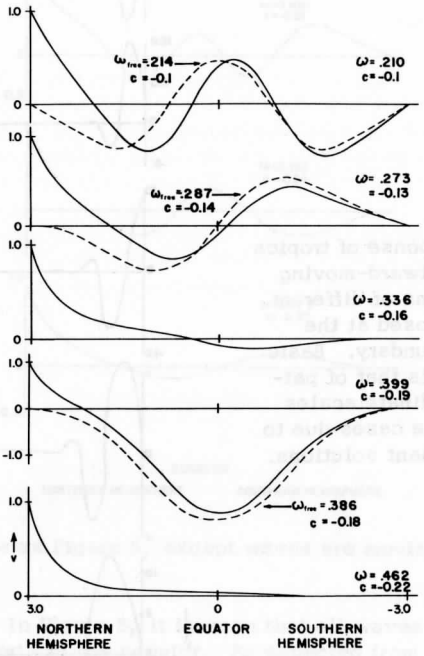

Figure 3. Solid lines indicate latitudinal profiles v(y) of response of tropics to imposed westward-moving waves at their northern boundary with no zonal flow. Dashed lines indicate free modes with neighboring phase speed.

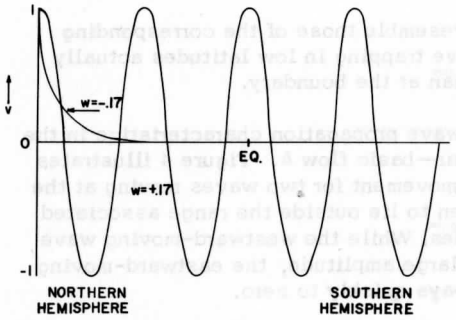

Figure 4. (left) Response of tropics v(y) to wave motions of same speed but differing directions imposed at the northern boundary. Basic zonal flow is that of pattern A. Speeds are chosen to allow comparisons of propagation regions at the left and right sides of Figure 1.

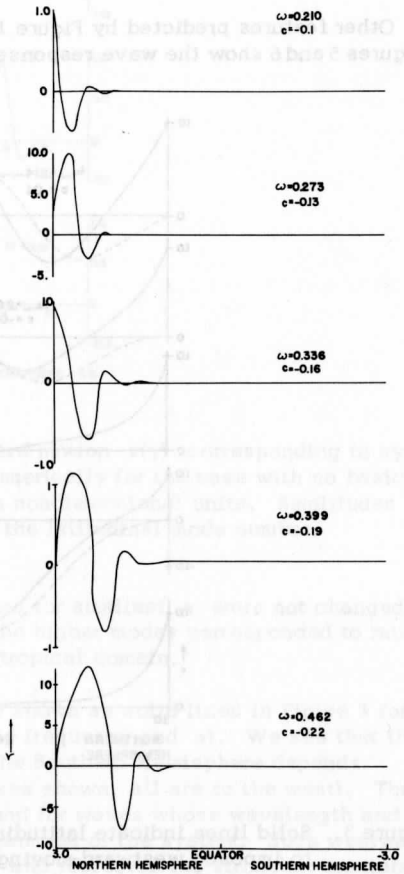

Figure 5. (right) Response of tropics v(y) to westward-moving wave motions of different speeds imposed at the northern boundary. Basic zonal flow is that of pattern B. Ordinate scales vary in some cases due to quasi-resonant solutions.

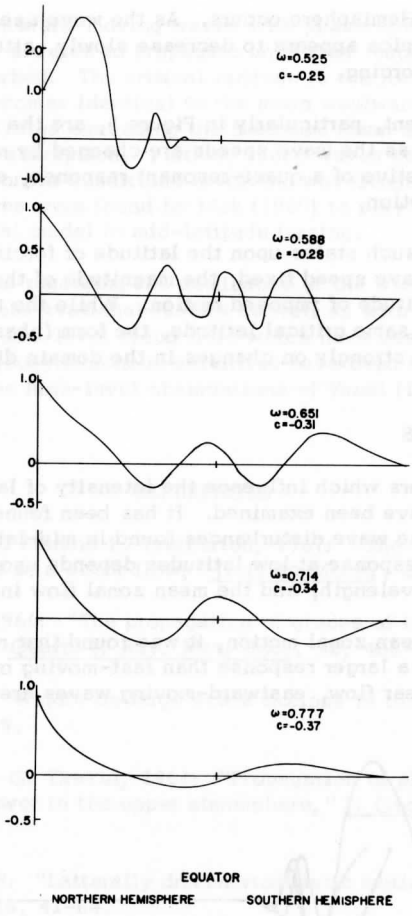

Figure 6. Same as Figure 5, except waves are moving faster.

ward wave movement. In Figure 5, it is seen that all waves suffer absorption at a critical latitude north of the equator. As expected from the condition $U(y) - c = 0$, the critical latitude moves toward the equator as the westward wave speeds increase.

With the second part of Figure 6, the critical latitude has "moved past the equator" and disappeared. Wave absorption immediately ceases and propaga-

tion into the Southern Hemisphere occurs. As the wave speeds increase further, the response of the tropics appears to decrease slowly, attaining a maximum at the boundary point of forcing.

Other features evident, particularly in Figure 5, are the strong differences in response magnitude as the wave speeds are changed by modest amounts. This is strongly suggestive of a quasi-resonant response, even in the presence of critical layer absorption.

The dependence of such states upon the latitude of forcing is shown in Figure 7. Even with wave speed fixed, the magnitude of the response is highly dependent upon the latitude of imposed motion. While the three responses exhibit absorption at the same critical latitude, the form (phase) of the response is also seen to depend strongly on changes in the domain dimensions.

CONCLUDING REMARKS

The dynamical factors which influence the intensity of large-scale disturbances in the tropics have been examined. It has been found that these motions may be coupled with the wave disturbances found in mid-latitudes. The precise character of the response at low latitudes depends upon the phase speed of the waves, their wavelength, and the mean zonal flow in the tropics.

In the absence of mean zonal motion, it was found that relatively slow-moving waves produce a larger response than fast-moving ones. In the presence of an easterly shear flow, eastward-moving waves are largely trapped in

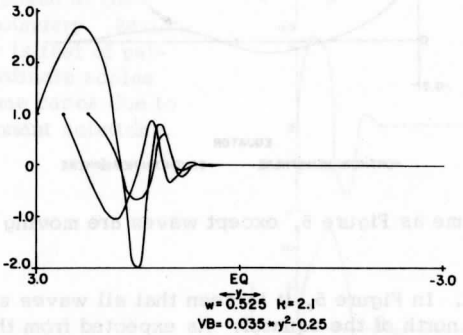

Figure 7. Response of tropics v(y) to westward moving wave of fixed speed at a northern boundary of variable location. Speed corresponds to the top portion of Figure 6. Basic zonal current is given by pattern B.

the subtropics. Westward-moving waves with phase speeds within the range of mean flow values are free to propagate until they reach a critical latitude, where they are absorbed. The critical latitude is the location where the westward wave speed becomes identical to the mean westward flow of air. Waves moving westward at rates exceeding the maximum mean zonal flow exhibit free propagation with no absorption. Further, these waves may undergo amplification when quasi-resonant conditions involving wavelength and wave speed are satisfied. Such waves were found by Mak (1969) to play a key role in the response of a tropical model to mid-latitude forcing.

These conclusions regarding the dominance of the westward-moving waves seem to agree with observational results as well as with the theoretical model. Disturbances in the low-level cloud field which have been studied using data taken from the ATS geosynchronous satellites have been found to possess these features, as have the high-level observations of Yanai (1968).

REFERENCES

Booker, John R., and Francis P. Bretherton, 1967: "The critical layer for internal gravity waves in a shear flow," J. Fluid Mech., 27, 513-539.

Bretherton, F. P., 1966: "The propagation of groups of internal gravity waves in a shear flow," Quart. J. Roy. Met. Soc., 92, 466-480.

Charney, J., 1963: "A note on large scale motions in the tropics," J. Atmos. Sci., 20, 607-609.

Charney, J., and P. G. Drazin, 1961: "Propagation of planetary-scale disturbances from the lower to the upper atmosphere," J. Geophys. Res., 66, 83-110.

Mak, Man-Kin, 1969: "Latterally driven stochastic motions in the tropics," J. Atmos. Sci., 26, 41-64.

Matsuno, T., 1966: "Quasi-geostrophic motions in the equatorial area," J. Meteor. Soc. Japan, 44, 25-42.

Yanai, M., and T. Maruyama, 1966: "Stratospheric wave disturbances propagating over the equatorial Pacific," J. Meteor. Soc. Japan, 44, 291-294.

Scanner's note:

This page is blank.

THREE-DIMENSIONAL, NUMERICAL SOLUTION OF THE ATMOSPHERIC DEEP-CONVECTION PROBLEM

U. Shafrir, S. Kaniel, and B. Schkoller

INTRODUCTION

It is a widespread feeling among meteorologists that the most crucial piece of information missing from our picture of the atmosphere as a whole is the mechanisms by which energy is supplied to the system. As it is clear that the atmospheric energy source resides in the tropics, what the foregoing statement really means is that we know too little about and do not understand at all the geophysical fluid dynamics of tropical regions. Expectedly, one result of this lack of understanding shows up very clearly in the imperfect predictions of numerical general circulation models. The importance of the ATS contribution should be measured against this background. For the first time we have available time-lapse photography of vast regions in the tropics which reveal, through cloud patterns, the preferred scales utilized by the solar energy to drive the atmosphere.

Several such case histories analyzed thus far clearly show that there are several basic mesoscale organizations of the flow (such as streets, rings, etc.) which dominate the tropical scene in most synoptic situations. However, upon closer examination, it becomes evident that the basic "building block" of these mesoscale patterns is the individual, deep-convection cell.

CURRENT WORK

Our current efforts focus on numerical modeling of the phenomena of deep convection. Because the same basic equations of hydrodynamics are applicable for both an individual cell and an ensemble of deep-convection elements, we plan to use the experiences gained during the construction of a numerical model of an individual cell when trying, at a later stage, to model numerically a whole ensemble of such cells.

The basic set of what later became known as "the anelastic equations" was originally derived by Batchelor in 1953. Ogura and Charney (1960) have derived independently an identical set of equations by filtering acoustic waves out of the "primitive" set of hydrodynamic equations (e.g., Navier-Stokes) for ideal fluid. Ogura and Phillips (1962) have shown that the apparently simpler set of approximations made by Batchelor is actually identical with that of Ogura and Charney and, in particular, that an assumption about the time scale must be made in order to derive these equations.

The set of anelastic equations was never solved for three independent space variables plus time. Ogura and Charney (1960), Ogura and Phillips (1962), and finally Ogura (1963), in a review article on numerical modeling of various scales of atmospheric flow patterns, have all pointed out a straightforward procedure of integration. However, the excessive amount of time coupled with a requirement for a huge memory core in a fast electronic computer have made it unrealistic to attempt a three-dimensional integration of these equations until now. In addition to this rather technical "boundary condition," there existed another, deeper rooted obstacle: No study of deep convection will be complete without obtaining detailed information on both the build-up and decay phases of a convective cell, as well as the spatial and temporal frequency of appearance for a given set of boundary and initial conditions. This obviously requires long-term integration of the differential equations, with its inherent danger of generating kinetic energy in the system by numerical rather than by physical means.

POSSIBLE SOLUTIONS

This problem, encountered in studies of the general circulation of the atmosphere has, as far as we know, only two solutions which are "guaranteed to work:" (1) to introduce into the equations the right amount of additional viscosity which will dissipate the artifically created kinetic energy; and (2) to use an energy- and momentum-conserving, finite difference scheme in the numerical computations.

The first solution, in addition to being unattractive from an "elegance" point of view, raises some questions with respect to the physical interpretation of the numerical results. The second solution has been impractical to date, because no three-dimensional, finite difference, energy-conserving scheme can be found in the literature.

At present, our investigation of the problem of deep convection is proceeding along three lines: (1) derivation of a stable, energy-conserving, finite difference scheme suitable for use with a nonlinear partial differential equation of the Navier-Stokes type; (2) construction of an efficient computational scheme to solve the set of three-dimensional, time-dependent, anelastic equations;

and (3) construction of an efficient computational scheme of the relevant microphysical parameters, which will be introduced together with moisture at a later stage of this investigation.

REFERENCES

Batchelor, G. K., 1953: "The conditions for dynamical similarity of motions of a frictionless perfect-gas atmosphere," Quart. J. Roy. Meteor. Soc., 79, 224-235.

Ogura, Y., 1963: "A review of numerical modeling research on small scale convection in the atmosphere," Meteor. Mono., 5: 27, 65-76.

Ogura, Y., and J. Charney, 1960: "A numerical model of thermal convection in the atmosphere," Proc. Internatl. Symp. Numerical Weather Prediction, Meteor. Soc. Japan, Tokyo, 431-452.

Ogura, Y., and N. A. Phillips, 1962: "Scale analysis of deep and shallow convection in the atmosphere," J. Atmos. Sci., 19, 173-179.

Scanner's note:

This page is blank.

ON THE TRANSIENT BEHAVIOR OF A SIMPLE MODEL OF CONVECTION

R. Schlesinger and J. Young

ABSTRACT

The transient behavior of the simple model of convection devised by Asai is studied. It is shown that the initial behavior of convective disturbances depends strongly upon the precise form of the disturbance and dissipative mechanisms. Final approach to a steady convective cell is dependent upon the relative importance of entrainment of heat and momentum. These conclusions, derived from linear analysis, are substantiated by a series of numerical experiments exhibiting the full nonlinear behavior of the system from formative stages to the final steady-state cell.

INTRODUCTION

In this paper we consider some influences of initial conditions, stability, entrainment intensity, and geometric configuration upon the development of steady-state cumulus convection as modeled by T. Asai (1967).

The geometry of Asai's convection model and the chief variables and constants are shown in Figure 1 and the following list of pertinent symbols:

- r = radial coordinate.
- z = vertical coordinate.
- u = radial velocity.
- w = vertical velocity.
- a = radius of updraft.
- b = total radius of cell.
- c = thickness of layer of inward motion.
- d = total thickness of cell.
- g = acceleration due to gravity.
- Θ = mean potential temperature at rest.

θ = potential temperature.

θ_e = equivalent potential temperature.

σ = a/b.

μ = c/d.

$l_r = \alpha a$, radial mixing length ($\alpha > 0$).

$l_z = \alpha d/2$, vertical mixing length.

$s_a = -\partial\theta_e/\partial z$ averaged along axis.

$s_b = +\partial\theta/\partial z$ averaged along axis.

$\delta = s_a/s_b$.

$$k_1 = (g/\Theta)(1-\sigma^2)/\left[1 - \frac{\ln\sigma}{\mu(1-\mu)}(a/d)^2\right].$$

$$k_2 = \frac{[2\alpha^2/a(1-\sigma^2)^2]\left[1 + (1-\sigma^2)^3\left(\frac{\sigma\ln\sigma}{1-\sigma^2}\right)^2\left(\frac{a}{d}\right)^4/2\mu^3(1-\mu)^3\sigma\right]}{1 - \frac{\ln\sigma}{\mu(1-\mu)}\left(\frac{a}{d}\right)^2}.$$

$$k_3 = s_b\left(\delta - \frac{\sigma^2}{1-\sigma^2}\right).$$

$$k_4 = [2\alpha^2/a(1-\sigma^2)^2]\left[1 + \frac{1-\sigma^2}{\alpha^2}\left(\frac{a}{d}\right)\right].$$

Asai's basic assumptions are as follows:

1. The atmosphere is unstable for moist ascending motion and stable for dry descending motion.

2. Motion is two-dimensional and cylindrical.

3. All diabatic heating is due to condensation, and evaporation is neglible in the descending current.

4. The total height of the cylinder is much smaller than the atmospheric scale height so that density variations may be disregarded.

5. $u < 0$, $\partial u/\partial z = 0$ for $0 \leq z < c$; $u > 0$, $\partial u/\partial z = 0$ for $c < z \leq d$; $w > 0$, $\partial w/\partial r = 0$ for $0 \leq r < a$; $w < 0$, $\partial w/\partial r = 0$ for $a < r \leq b$.

6. θ increases with height but at each level assumes separate constant values in the ascending and descending regions.

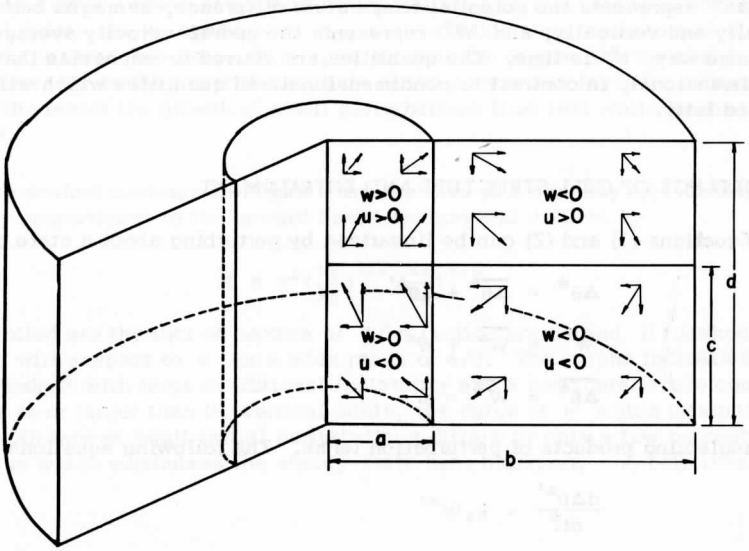

Figure 1. Illustration of the principal geometric features of Asai's model of symmetric convection. The vector meridional wind and its components are denoted by arrows in each subregion. The cloudy region is assumed to be $r < a$.

7. No motion or transport of properties occurs normal to a boundary.
8. A mixing-length hypothesis is assumed for eddy transport of heat and momentum as indicated in the list of symbols.

By integrating the thermodynamic equation and the vorticity equation and simplifying the resulting expressions with the help of his assumptions, Asai obtains two ordinary nonlinear differential equations relating the velocity of the updraft to the potential temperature difference between the updraft and the surrounding downdraft:

$$\frac{d\Delta\theta^*}{dt^*} = k_3 W^* - k_4 \Delta\theta^* W^* \qquad (1)$$

$$\frac{dW^*}{dt^*} = k_1 \Delta\theta - k_2 W^{*2} \qquad (2)$$

$\Delta\theta^*$ represents the potential temperature difference, averaged both horizontally and vertically, and W^* represents the updraft velocity averaged in the same way; t^* is time. The quantities are starred to emphasize that they are dimensional, in contrast to nondimensionalized quantities which will be defined later.

IMPORTANCE OF CELL STRUCTURE AND ENTRAINMENT

Equations (1) and (2) can be linearized by perturbing about a state of rest

$$\Delta\theta^* = \overline{\Delta\theta^*} + \Delta\theta^{*\prime} \tag{3}$$

$$W^* = \overline{W^*} + W^{*\prime} \tag{4}$$

$$\overline{\Delta\theta^*} = \overline{W^*} = 0 \tag{5}$$

and neglecting products of perturbation terms. The following equations result:

$$\frac{d\Delta\theta^{*\prime}}{dt^*} = k_3 W^{*\prime} \tag{6}$$

$$\frac{dW^{*\prime}}{dt^*} = k_1 \Delta\theta^{*\prime} \tag{7}$$

When k_3 is positive, as is assumed throughout, equations (6) and (7) have solutions which are linear combinations of e^{Kt^*} and e^{-Kt^*}, where

$$K = \sqrt{k_1 k_3} \tag{8}$$

The e-folding time, the length of time in which the amplifying component e^{Kt^*} grows by a factor of e, is defined by

$$\tau^* = 1/\sqrt{k_1 k_3} \tag{9}$$

Figure 2 exhibits the dependence of τ^* upon the shape of the convective cylinder (σ) and upon the conditional instability (δ) of the updraft. As in Asai's article (1967), the thickness of the inflow layer is taken to be half the total thickness in order to maximize steady-state upward heat transport with respect to μ. A mean potential temperature of 300°K is taken as a reasonable value. The fraction of the area covered by ascending motion is limited by the requirement that k_3 be positive for exponential growth of small perturbations. From Asai's definition of k_3, the cut-off value σ_c of σ is

$$\sigma_c = \sqrt{\frac{\delta}{1+\delta}} \tag{10}$$

The solid curves, which are nearly horizontal for small σ, are isolines of $1/\tau^*$ (1/min). As σ approaches σ_c, the e-folding time tends to infinity, since k_3 approaches zero. It is apparent that the greater the instability (the larger δ), or the lower the altitude of the convective layer for a fixed value of Θ, the faster the growth of small perturbations from rest while linear theory applies.

The dashed contours in Figure 2 are isolines of a quantity H (°C-cm/sec) directly proportional to the upward heat transport and defined by

$$H = \sigma^2 \left(\frac{k_1}{k_2}\right)^{1/2} \left(\frac{k_3}{k_4}\right)^{3/2} \qquad (11)$$

Also plotted are the loci of maxima of $1/\tau^*$ (solid curves) and H (dashed curves) with respect to σ for a wide range of a/d. The graphs indicate that for an updraft with large conditional instability and a horizontal scale comparable to or larger than its vertical scale, the value of σ which maximizes the growth rate of small initial perturbations differs by only a few percent from the value which maximizes the steady-state heat transport, and both these

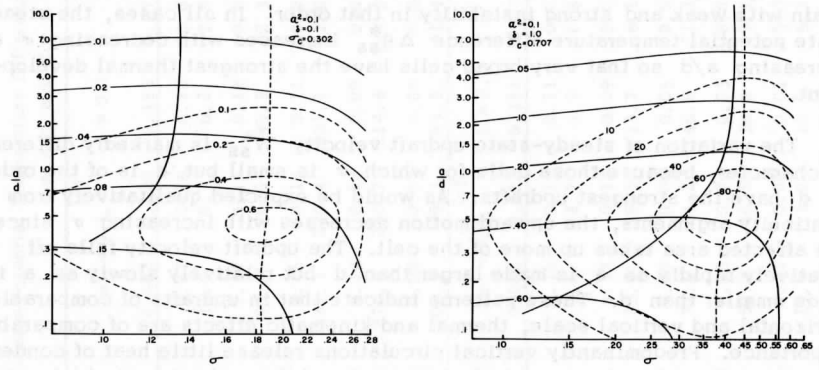

Figure 2. Isolines of H (dashed contours) and $1/\tau^*$ (solid contours) as functions of σ and a/d, as explained in the text. $s_b = 3.8$°C/km. (a) $\delta = 0.1$; (b) $\delta = 1.0$.

values are nearly independent of a/d. If the instability is small, the critical values of σ are still virtually independent of a/d, but the correlation between rapid early growth and large steady-state heat transport is much weaker. In narrow updrafts, no such correlation is evident. The degree of entrainment is unimportant; α^2 is 0.1 in Figure 2, but if α^2 is increased to 1.0, H varies with σ and a/d in much the same way, apart from becoming about one order of magnitude smaller and taking on its absolute maximum for a/d about 40 percent larger.

Under a wide variety of initial conditions (with certain restrictions to be described later), $\Delta\theta^*$ and W^* tend asymptotically to the nonzero steady-state values obtained formally by setting $\frac{d\Delta\theta^*}{dt}$ and $\frac{dW^*}{dt}$ equal to zero in equations (1) and (2), namely

$$\Delta\theta^*_{ss} = k_3/k_4 \tag{12}$$

$$W^*_{ss} = \left(\frac{k_1 k_3}{k_2 k_4}\right)^{1/2} \tag{13}$$

The variation of these values with entrainment intensity, stability, and cell shape for a total thickness of 1 km is demonstrated in Table 1. The same assumptions are made as in Figure 2. Cases a and b correspond to weak entrainment ($\alpha^2 = 0.1$), with weak instability ($\delta = 0.1$) and strong instability ($\delta = 1.0$), respectively. Cases c and d represent strong entrainment ($\alpha^2 = 1.0$), again with weak and strong instability in that order. In all cases, the steady-state potential temperature difference $\Delta\theta^*_{ss}$ increases with decreasing σ and increasing a/d so that very broad cells have the strongest thermal development.

The variation of steady-state updraft velocity W^*_{ss} is markedly different in character, because those cells for which σ is small but a is of the order of d have the strongest updrafts. As would be expected qualitatively from continuity arguments, the upward motion decreases with increasing σ since the affected area takes up more of the cell. The updraft velocity falls off relatively rapidly as a is made larger than d but relatively slowly as a is made smaller than d. These patterns indicate that in updrafts of comparable horizontal and vertical scale, thermal and kinematic effects are of comparable importance. Predominantly vertical circulations release little heat of condensation in spite of moderate updraft velocities, while predominantly horizontal circulations release the most heat despite small upward velocities.

Parts a and b of Table 1 are not fully comparable with each other, nor are parts c and d, since σ_c is 0.707 for $\delta = 1.0$ but only 0.302 for $\delta = 0.1$, resulting in considerably different ranges of admissible values for σ. If σ is substantially below 0.3, the tenfold increase in the stability ratio results in an increase of $\Delta\theta^*_{ss}$ by one order of magnitude or slightly more over the

TABLE 1

Steady-State Potential Temperature Difference $\Delta\theta^*_{ss}$ (°K) and Upward Motion W^*_{ss} (cm/sec) as a Function of σ and a/d for d = 1 km, $\mu = 0.5$, and $S_b = 3.8°C/km$

(a) $\alpha^2 = 0.1$, $\delta = 0.1$

a/d \ σ	0.082	0.122	0.183	0.273
11.59	0.17	0.16	0.12	0.03
	11.6	8.7	6.2	2.8
2.86	0.17	0.15	0.12	0.03
	93.0	70.0	49.5	22.3
1.00	0.16	0.15	0.11	0.03
	331.3	270.4	201.1	92.6
0.350	0.14	0.12	0.09	0.03
	274.4	255.7	214.4	106.5
0.086	0.08	0.07	0.05	0.02
	106.1	99.3	83.5	41.4

(b) $\alpha^2 = 0.1$, $\delta = 1.0$

a/d \ σ	0.082	0.159	0.309	0.599
11.59	1.86	1.79	1.53	0.53
	37.9	25.6	17.7	8.7
2.86	1.82	1.75	1.48	0.51
	303.5	205.4	141.8	69.5
1.00	1.71	1.64	1.39	0.46
	1081.6	822.5	590.9	261.3
0.350	1.46	1.40	1.17	0.37
	895.6	843.9	685.1	233.3
0.086	0.87	0.83	0.68	0.19
	346.3	328.5	265.6	84.3

(c) $\alpha^2 = 1.0$, $\delta = 0.1$

a/d \ σ	0.082	0.122	0.183	0.273
11.59	0.16	0.15	0.11	0.03
	3.5	2.7	1.9	0.8
2.86	0.13	0.12	0.09	0.03
	25.7	19.3	13.7	6.1
1.00	0.09	0.08	0.06	0.02
	77.6	63.2	46.8	21.4
0.350	0.05	0.04	0.03	0.01
	50.0	46.5	38.8	19.1
0.086	0.01	0.01	0.01	0.00
	13.9	13.0	10.9	5.3

(d) $\alpha^2 = 1.0$, $\delta = 1.0$

a/d \ σ	0.082	0.159	0.309	0.599
11.59	1.73	1.66	1.41	0.47
	11.5	7.8	5.4	2.6
2.86	1.39	1.33	1.11	0.35
	84.0	56.7	38.8	18.1
1.00	0.94	0.89	0.73	0.21
	253.3	191.9	135.7	55.5
0.350	0.48	0.46	0.37	0.10
	163.2	153.1	121.9	38.0
0.086	0.15	0.14	0.11	0.03
	45.3	42.8	34.1	10.2

NOTE: In each row upper figures are for $\Delta\theta^*_{ss}$; lower figures are for W^*_{ss}.

tabulated range of a/d, while W^*_{ss} increases by close to half an order of magnitude. Therefore, in Asai's model, the released latent heat in the updraft increases somewhat more strongly with the instability than does the upward motion.

Parts a and c of Table 1 are completely comparable with each other, as are parts b and d, since each separate pair of parts assumes the same value of δ and hence the same value of σ_c. Both comparisons show that the thermal development decreases drastically with increasing entrainment in narrow updrafts but by only a few percent in wide updrafts. When α^2 is increased from 0.1 to 1.0, W^*_{ss} drops by nearly a full order of magnitude in narrow updrafts and by about half an order of magnitude in wide ones. Increasing the entrainment intensity in narrow updrafts reduces both the thermal and kinetic development drastically, while in wide updrafts the kinematic development is damped by a factor of three with only a slight decrease in the thermal development.

THEORETICAL PREDICTIONS

Table 1 has provided an idea of the variations of growth rates of small initial perturbations about a rest state and of the actual steady-state temperature difference and updraft velocity in Asai's convection cell for various geometric proportions, entrainment intensities, and stability ratios. It is also instructive to study the effect of initial conditions upon the manner of approach to the steady state (in admissible cases). If dimensionless potential temperature difference, updraft velocity, and time are defined by

$$\Delta\theta = \Delta\theta^*/\Delta\theta^*_{ss} \tag{14}$$

$$W = W^*/W^*_{ss} \tag{15}$$

$$t = t^*/\tau^* \tag{16}$$

the steady-state values of both $\Delta\theta$ and W are unity. The nondimensionalized forms of equations (1) and (2) are

$$\frac{d\Delta\theta}{dt} = \frac{1}{R}(W - W\Delta\theta) \tag{17}$$

$$\frac{dW}{dt} = R(\Delta\theta - W^2) \tag{18}$$

where R is a number which depends only upon the dissipative parameters k_2 and k_4:

$$R = \sqrt{k_2/k_4} \tag{19}$$

The quantity R does not depend explicitly on the stability ratio, since k_3 is the only one of the four parameters in equations (1) and (2) involving δ. However, k_2 and k_4 depend on a/d and σ, and the larger the value of δ, the greater the cut-off value σ_c.

Table 2 displays the variation of R as a function of σ and a/d for weak, moderate, and strong entrainment as indicated. Again μ is assumed to be 0.5, while δ is unspecified in order to make the three parts of the table fully comparable. Over the tabulated range of a/d, R increases with σ somewhat more slowly than σ for large a/d and very little for small a/d; R can assume larger values as the conditional instability and hence σ_c are increased. Some other features concerning R can be noted in Table 2:

1. For each value of α^2, the smallest values of R occur in updrafts whose depth and radius are comparable and which are narrow compared to the whole cell. In plume-shaped updrafts (those in which a is much smaller than d), R is slightly smaller than one, approaching that value from below with increasing entrainment intensity. The largest values of R shown correspond to wide cells whose updrafts occupy a considerable fraction of the total radius (or area). Such cells require relatively large values of σ and therefore relatively great conditional instability, and could exist only at sufficiently low altitudes for the moist-adiabatic lapse rate to be well below the environmental lapse rate.

2. R increases with α^2 for each tabulated combination of σ and a/d. For a/d around 10, R increases nearly proportionally to α but more slowly as a/d increases, until R is almost independent of α when a/d is about one-tenth.

Since R depends on entrainment intensity as well as on cell geometry, any rigid or complete classification of convection modes in terms of R is difficult. Certain tendencies may be inferred nevertheless from a comparison of Table 2 with Table 1 and Figure 2:

1. Values of R much below one are favored by weak entrainment, radius-to-height ratios of order unity, high updraft speed, and large areas of descending motion.

2. Values of R substantially greater than one are favored by strong entrainment, large radius-to-height ratios (wide updrafts), large values of σ (and, in turn, considerable instability), and low updraft velocity. Small initial perturbations grow slowly.

3. Apart from transitional modes between those described in items 1 and 2, values of R slightly below one occur in cells having plume-like updrafts. The magnitudes of α^2, σ, and δ are of little importance. Small initial

TABLE 2

Dimensionless Parameter R in Asai Model as a Function of σ and a/d, with $\mu = 0.5$

a/d \ σ	$\alpha^2 = 0.1$			
	0.086	0.157	0.333	0.607
11.59	0.41	0.65	1.06	1.29
2.86	0.20	0.32	0.51	0.62
1.00	0.14	0.20	0.30	0.36
0.350	0.32	0.35	0.41	0.51
0.086	0.71	0.72	0.74	0.80
0.021	0.91	0.91	0.92	0.94

a/d \ σ	$\alpha^2 = 0.4$			
	0.086	0.157	0.333	0.607
11.59	0.81	1.28	2.08	2.54
2.86	0.38	0.60	0.97	1.14
1.00	0.25	0.36	0.53	0.61
0.350	0.50	0.54	0.62	0.73
0.086	0.88	0.88	0.90	0.93
0.021	0.97	0.97	0.98	0.98

a/d \ σ	$\alpha^2 = 1.0$			
	0.086	0.157	0.333	0.607
11.59	1.25	1.97	3.21	3.87
2.86	0.55	0.87	1.40	1.60
1.00	0.34	0.47	0.69	0.76
0.350	0.59	0.64	0.72	0.82
0.086	0.93	0.94	0.95	0.97
0.021	0.99	0.99	0.99	0.99

perturbations grow rapidly, although the steady-state rising motion is only weak to moderate.

Let us now examine the behavior of the nondimensional variables $\Delta\theta$ and W in the vicinity of the steady states of rest ($\Delta\theta = W = 0$) and cellular convection ($\Delta\theta = W = 1$). Considering first perturbations θ' and W' about the state of rest, the linearized equations

$$\frac{d}{dt}(\Delta\theta') = \frac{1}{R} W' \tag{20}$$

$$\frac{dW'}{dt} = R\Delta\theta' \tag{21}$$

together with initial perturbation states $\Delta\theta_0'$ and W_0' give the solutions

$$\begin{pmatrix}\Delta\theta' \\ W\end{pmatrix} = \left(\frac{\Delta\theta_0'R + W_0'}{2R}\right)\begin{pmatrix}1 \\ R\end{pmatrix} e^{t} + \left(\frac{\Delta\theta_0'R - W_0'}{2R}\right)\begin{pmatrix}1 \\ -R\end{pmatrix} e^{-t} \tag{22}$$

Interestingly, certain initial states exclude the unstable growth generally implied by the first term on the right-hand side of equation (22). For example, when the buoyancy has the negative value $\Delta\theta_0' = \frac{-1}{R} W_0' < 0$, the solutions are simply decaying perturbations toward the state of rest:

$$\begin{pmatrix}\Delta\theta' \\ W'\end{pmatrix} = \Delta\theta_0' \begin{pmatrix}1 \\ -R\end{pmatrix} e^{-t} \tag{23}$$

(When $R = 1$ it can be readily verified that a similar decay is followed even in the case of finite perturbations in the nonlinear stages.)

If the initial buoyancy is even more negative ($\Delta\theta_0' < -\frac{1}{R} W_0'$), the in-cloud upward motion decreases to zero in a time equal to

$$t = \ln\left(\frac{\Delta\theta_0'R - W_0'}{\Delta\theta_0'R + W_0'}\right)^{1/2}$$

Subsequent times correspond to downward motion in the cloud ($W' < 0$), in which case the assumption of pseudo-adiabatic motions in the cloudy region is not physically realistic. It then appears that steady convection can never develop from a sufficiently unfavorable thermal field $\Delta\theta_0' < -\frac{1}{R} W_0'$.

When the initial state exhibits positive buoyancy, the final state would always appear to be one of steady, finite amplitude convection. This is especially suggested in the case $\Delta\theta_0' = \frac{W_0'}{R}$ when only the amplifying perturbation is present:

$$\begin{pmatrix} \Delta\theta' \\ W' \end{pmatrix} = \Delta\theta_0' \begin{pmatrix} 1 \\ R \end{pmatrix} e^{t} \tag{24}$$

As all such unstable disturbances grow toward the final state, the nonlinear dissipative terms play a relatively more important role, and the above linear equations do not hold. To understand the approach to steady convection from any nearby state of motion, let us now consider the perturbations $\Delta\hat{\theta}$ and $\hat{W}$ about the steady state $\Delta\theta = W = 1$. They are governed by the linearized equations

$$\frac{d}{dt}(\Delta\hat{\theta}) = -\frac{1}{R}\Delta\hat{\theta} \tag{25}$$

$$\frac{d}{dt}(\hat{W}) = R(\Delta\hat{\theta} - 2\hat{W}) \tag{26}$$

whose solutions for $R \neq \frac{\sqrt{2}}{2}$ are:

$$\begin{pmatrix} \Delta\hat{\theta} \\ \hat{W} \end{pmatrix} = \frac{R^2\Delta\hat{\theta}_0}{2R^2-1}\begin{pmatrix} 2-\frac{1}{R^2} \\ 1 \end{pmatrix} e^{-\frac{1}{R}t} + \left(\hat{W}_0 - \frac{R^2\Delta\hat{\theta}_0}{2R^2-1}\right)\begin{pmatrix} 0 \\ 1 \end{pmatrix} e^{-2Rt} \tag{27}$$

$\Delta\hat{\theta}_0$ and $\hat{W}_0$ represent the initial perturbations. When $R = \frac{\sqrt{2}}{2}$, the solutions become

$$\begin{pmatrix} \Delta\hat{\theta} \\ \hat{W} \end{pmatrix} = \begin{pmatrix} \Delta\hat{\theta}_0 \\ \hat{W}_0 + \frac{\Delta\hat{\theta}_0}{\sqrt{2}}t \end{pmatrix} e^{-\sqrt{2}t} \tag{28}$$

Since all perturbation modes are seen to decay, the steady convection cell is approached from nearly all states and for all values of R. When $R << \frac{\sqrt{2}}{2}$, W dies later than $\Delta\hat{\theta}$ (i.e., the thermal field is the first to approach its steady value). When $R >> \frac{\sqrt{2}}{2}$, the fields of motion and temperature slowly approach the steady state together:

$$\begin{pmatrix} \Delta\hat{\theta} \\ \hat{W} \end{pmatrix} = \Delta\hat{\theta}_0 \begin{pmatrix} 1 \\ 1/2 \end{pmatrix} e^{-\frac{1}{R}t} \tag{29}$$

Taken together, these two sets of linear results suggest interesting differences in the evolution of convection cells for different values of R. For example, when $R << 1$, small perturbations rapidly develop their steady thermal state, followed by a slower approach of the field of motion to its final form. When $R >> 1$, the W field develops quickly, after which W and $\Delta\theta$ evolve together to the mature state.

Finally, when $R = 1$ and with initial positive buoyancy $\Delta\theta_0' = W'$, we

have the linear results:

$$\Delta\theta' = \Delta\theta_0' e^{t} \qquad W' = W_0' e^{t} \tag{30}$$

which conceivably lead to

$$\Delta\hat{\theta} = \Delta\hat{\theta}_0 e^{-t} \qquad \hat{W} = \hat{W}_0 e^{-t} \tag{31}$$

when $\Delta\hat{\theta}_0 = \hat{W}_0 < 0$, suggesting that W and $\Delta\theta$ grow together at the same rate. This may be verified for the full nonlinear equations in the special case when $W = \Delta\theta$ for all time. The governing equations then reduce to

$$\frac{dW}{dt} = W - W^2 \tag{32}$$

which gives the solution

$$W(t) = \frac{W_0 e^{t}}{(1-W_0) + W_0 e^{t}} = \Delta\theta(t) \tag{33}$$

This solution exhibits initial exponential growth of W and $\Delta\theta$ together, followed by their transition to the final asymptotic approach to steady convection.

NUMERICAL SOLUTIONS

In the preceding section, linear theory was used to predict the qualitative features of the initial and final stages of convection. Nonlinear results were obtained for a single, special case only. In order to extend the results in the nonlinear cases we consider now the approximate solution of equations (17) and (18) using the 4-step Runge-Kutta scheme with time steps $\Delta t = 0.1$. The results are obtained for a variety of initial states in the $\Delta\theta$ - W plane.

In the first four of the eight cases considered, the combinations of $\Delta\theta_0$ and W_0 represent small perturbations from rest, lying on a circle of radius 0.1 in the $\Delta\theta$ - W plane. In the other combinations, large perturbations are represented by placing the initial point on a circle of radius two, so that at least one of $\Delta\theta_0$ and W_0 is appreciably greater than the steady-state value of unity. The inner cylinder of the cell is assumed to be initially colder than its surroundings in two cases so that the possibility of steady-state convection under such a condition may be explored. (In all cases, W_0 is non-negative since descending motion in the inner cylinder is not of physical interest.) The sets of initial conditions are as follows:

Figure	Case	$\Delta\theta_0$	W_0
4	1	0.1000	0.0000
5	2	0.0707	0.0707
6	3	0.0000	0.1000
7	4	-0.0707	0.0707
8	5	2.0000	0.0000
9	6	1.4142	1.4142
10	7	0.0000	2.0000
11	8	-1.4142	1.4142

The results appear in Figures 3 through 11 as plots of the solution in the phase plane. Figure 3 allows comparison of the solution curves for various values of R. We see that the agreement of the curves with the results predicted in the preceding section is good.

Figures 4 through 11 show how the convection is affected by changes in R when the initial state is held fixed. The different rates of evolution are apparent from the isolines of time indicated in each figure.

In the first three cases, steady-state convection develops for the range of R considered (from 0.15 to 2.40). The thermal development is generally ahead of the kinematic development when $R < 1$ and lags behind the kinematic development when $R > 1$. As has been noted, values of R much below unity are associated mostly with very strong steady-state upward motion; the graphs show that such updrafts develop little of their speed until "thermal equilibrium" is nearly achieved. On the other hand, those updrafts which attain only a low velocity have gained about two-thirds of their speed by the time the potential temperature gradient is half established. After some adjustment, the plume-like updrafts (R close to one) approach the steady-state temperature excess and upward velocity practically in phase. In Case 2, where $\Delta\theta_0 = W_0$, $\Delta\theta$ and W remain equal for all time for $R = 1$ as predicted.

The early development of convection is markedly different in cases 1 and 3. In the first case, with a small temperature difference but no wind initially, the rate of change of temperature difference with t is nearly independent of R, while the updraft develops in proportion to R. In Case 3, with initial upward motion but no temperature contrast, the acceleration of the updraft for t less than approximately 2 depends very little on R, but the temperature gradient is nearly proportional to R. The shift of the initial impetus from thermal to kinematic from Case 1 to Case 3 quickens the overall convective development for small R and retards it for large R, with little effect for R near one. This suggests, in turn, that wide updrafts with small steady-state velocities (large R) develop more rapidly from small thermal perturbations than from a slight upward push; narrow updrafts with high velocities (small R) grow faster from a

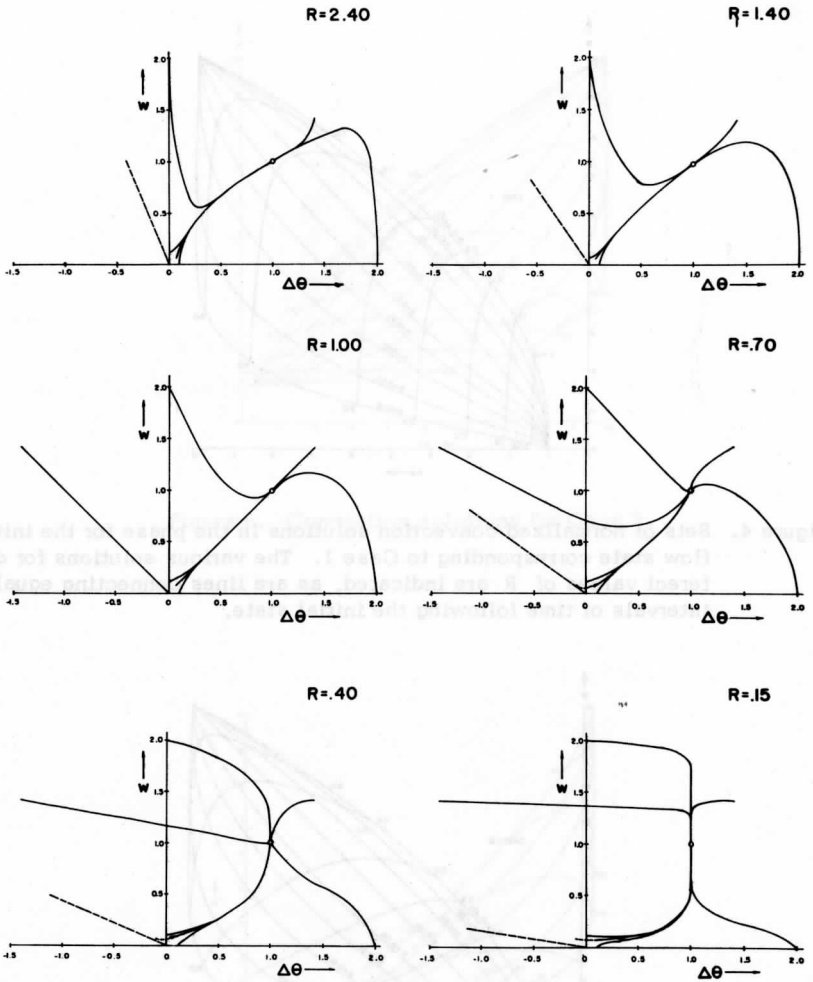

Figure 3. Sets of normalized convection solutions in the phase plane for various values of the parameter R. The state of steady cellular convection is denoted by a circle. The curves show the approach toward the steady state from various initial conditions represented by the free ends.

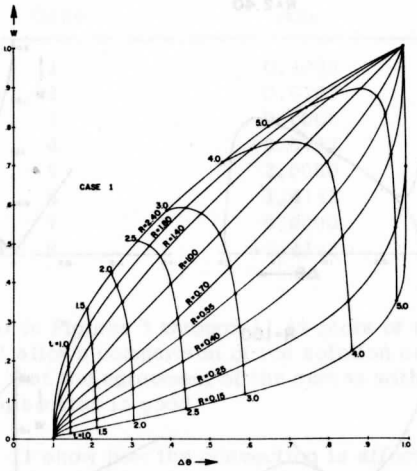

Figure 4. Sets of normalized convection solutions in the phase for the initial flow state corresponding to Case 1. The various solutions for different values of R are indicated, as are lines connecting equal intervals of time following the initial state.

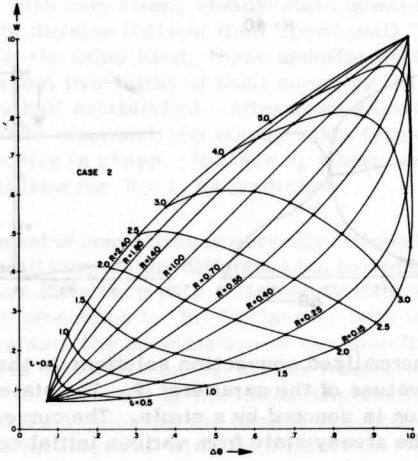

Figure 5. Convection solutions for Case 2.

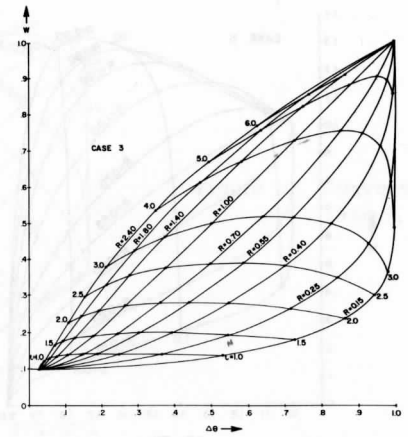

Figure 6. Convection solutions for Case 3.

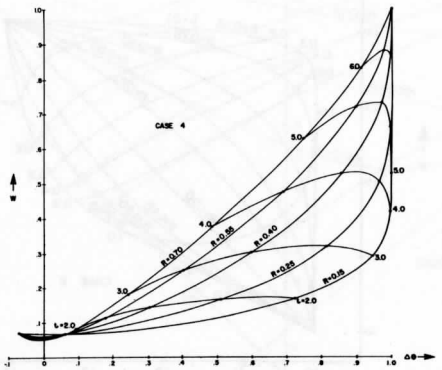

Figure 7. Convection solutions for Case 4.

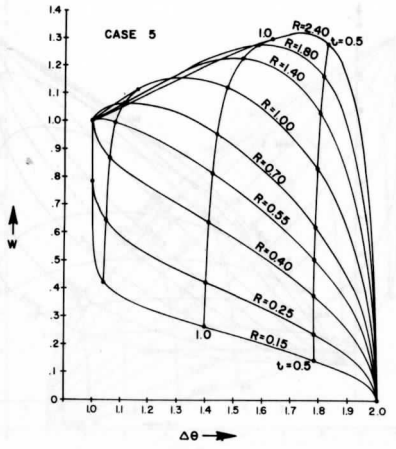

Figure 8. Convection solutions for Case 5.

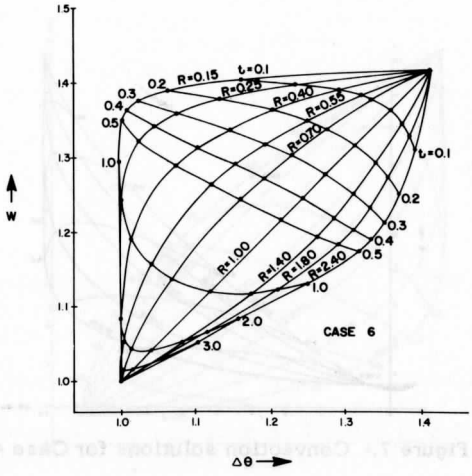

Figure 9. Convection solutions for Case 6.

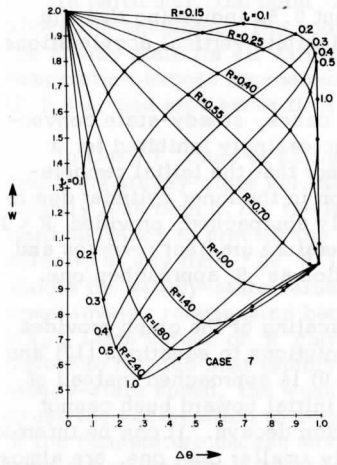

Figure 10. Convection solutions for Case 7.

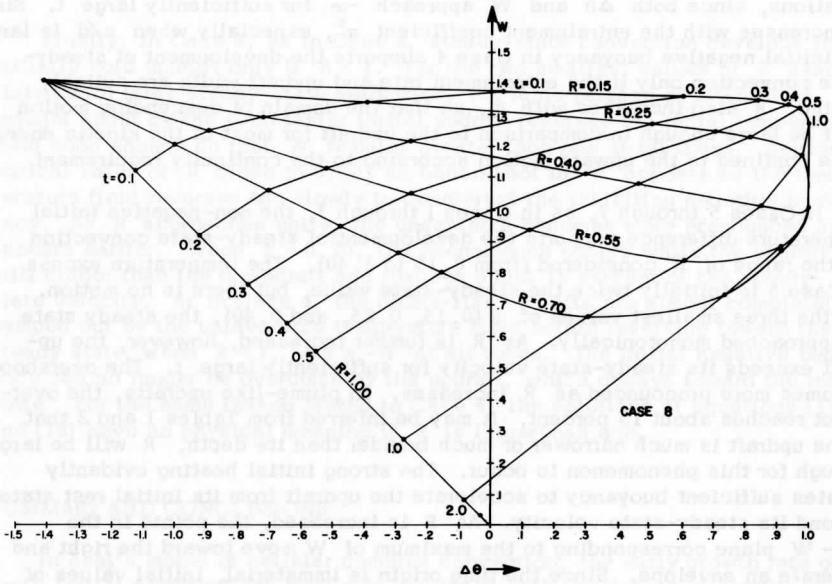

Figure 11. Convection solutions for Case 8.

slight upward velocity than from thermal buoyancy. All the curves in Case 3 are virtually horizontal for values of t under about 0.5, indicating that the lack of an initial temperature excess temporarily inhibits vertical accelerations, as would be expected from buoyancy arguments.

In Case 4, in contrast to the preceding three cases, steady-state convection develops only if $R < 1$. Updraft growth is increasingly inhibited for t smaller than about 2 as R is increased. It is clear that the initial temperature distribution tends to discourage upward motion in the inner cylinder due to negative buoyancy. The steady state is eventually approached, provided $R < 1$, but the updraft does not accelerate until the temperature gradient reverses and shows an increasingly pronounced early deceleration as R approaches one.

The curve for $R = 1$ is not shown since the scaling of the graph provides too little room to include isolines of t, but the solutions to equations (17) and (18) become singular. The rest state ($\Delta\theta = W = 0$) is approached instead of the steady state($\Delta\theta = W = 1$). At this point, the initial upward push cannot overcome the negative buoyancy, and the convection decays. It can be inferred that the plume-like updrafts, with R only slightly smaller than one, are almost completely damped before reversing and approaching the steady state. Values of R larger than one correspond to physically meaningless solutions of the equations, since both $\Delta\theta$ and W approach $-\infty$ for sufficiently large t. Since R increases with the entrainment coefficient α^2, especially when a/d is large, the initial negative buoyancy in Case 4 supports the development of steady-state convection only if the entrainment rate and updraft width are suitably limited. R also increases with σ, so that the domain of descending motion must be large enough in comparison to the updraft for most of the kinetic energy to be confined to the upward motion according to the continuity requirement.

In Cases 5 through 7, as in Cases 1 through 3, the non-negative initial temperature difference supports the development of steady-state convection for the range of R considered (from 0.15 to 2.40). The temperature excess in Case 5 is initially twice the steady-state value, but there is no motion. For the three smallest values of R (0.15, 0.25, and 0.40), the steady state is approached monotonically. As R is further increased, however, the updraft exceeds its steady-state velocity for sufficiently large t. The overshoot becomes more pronounced as R increases. In plume-like updrafts, the overshoot reaches about 15 percent. It may be inferred from Tables 1 and 2 that if the updraft is much narrower or much broader than its depth, R will be large enough for this phenomenon to occur. The strong initial heating evidently creates sufficient buoyancy to accelerate the updraft from its initial rest state beyond its steady-state velocity. As R is increased, the points in the $\Delta\theta$ - W plane corresponding to the maximum of W move toward the right and generate an envelope. Since the time origin is immaterial, initial values of $\Delta\theta$ and W situated above this envelope would not be expected to lead to the unstable acceleration just described.

In particular, the point $\Delta\theta = W = 1.4142$, the initial point in Case 6, lies above the envelope. The convection weakens monotonically with time toward the steady state for all values of R in Case 6. As in Case 2, the potential temperature excess approaches the steady state earlier than the updraft velocity if $R < 1$, and vice versa if $R > 1$.

In Case 7, there is no initial temperature gradient, but an updraft having twice the steady-state velocity is assumed. Below a critical value of R slightly less than 0.70, the released heat of condensation creates enough upward buoyancy to prevent the current from decelerating below the steady-state velocity at any time. As R increases beyond the critical value, W undershoots the steady-state value more and more pronouncedly. In view of the rough inverse relationship between R and the actual steady-state velocity W^*_{ss}, large values of R correspond to weak currents which would not be expected to release heat rapidly. When the decelerating current passes its steady-state speed, the weakness of the upward buoyancy together with inertia cause the deceleration to persist. The plume-like updrafts have generated most of the temperature excess when this phenomenon appears, and the undershoot does not exceed about 10 percent. When $R = 2.40$, the undershoot already appears before the temperature difference has attained 15 percent of the steady-state value, and reaches close to 50 percent.

Finally, in Case 8, as in Case 4, steady-state convection develops in the initially cold updraft only if $R < 1$. For the two smallest values of R associated with large steady-state velocities, the rapid release of latent heat brought about by the even faster initial updraft reverses the radial temperature field soon enough so that W remains greater than one at all times. Beyond a critical value of R close to 0.40, an undershoot in W appears as the temperature field reverses too slowly to counteract the inhibiting negative buoyancy. As R approaches unity, the undershoot becomes more pronounced and appears earlier. When $R = 0.70$, the phenomenon occurs while the updraft is still colder than the downdraft and reaches about 35 percent of the steady-state velocity. As in Case 4, the plume-like updrafts are almost completely damped out by the unfavorable temperature field before reversing toward the steady state; when $R = 1$, $\Delta\theta = -W$ at all times. The initial negative buoyancy can no longer be overcome by the updraft, which decays toward the rest state. For the same reason stated in Case 4, the solutions of equations (17) and (18) have no physical meaning if R is larger than one.

SUMMARY AND CONCLUSIONS

In Asai's model of cellular cumulus convection, the early growth rate of small initial perturbations from rest increases with the degree of conditional instability and shows a rough direct variation with the steady-state upward heat transport if the horizontal scale of the updraft is comparable to or larger

than its vertical scale. Plume-like updrafts within cells of small horizontal scale grow the most rapidly.

For either small or large initial perturbations (relative to steady-state values), it appears that steady-state convection always develops under any of the following initial conditions:

1. Temperature excess with no vertical motion.
2. Both upward motion and temperature excess.
3. Upward motion with no temperature excess.

Beyond the early growth states, the mode of approach toward steady-state for small initial perturbations is nearly independent of the initial conditions for a given combination of cell geometry, entrainment rate, and conditional instability. In broad updrafts with low steady-state velocities, the temperature excess lags behind the velocity, while the opposite holds for narrow updrafts with high steady-state velocities. When the horizontal and vertical scales of the updraft are strongly different, large initial heating without vertical motion creates sufficient buoyancy to accelerate the updraft temporarily beyond the steady-state speed. On the other hand, with no initial heating but upward motion faster than the steady state, currents with low absolute velocities temporarily undershoot the equilibrium velocity due to the small thermal buoyancy.

Initial upward motion with a negative temperature perturbation supports the development of steady-state convection provided the entrainment rate and updraft width (relative to the total cell width) are sufficiently small. Horizontal mixing is then small, so that the latent heat release resulting from the initial upward push can overcome the negative buoyancy. If these conditions are not satisfied, there is either no physically meaningful convection, or singular damping to the rest state occurs.

REFERENCE

Asai, T., 1967: "On the characteristics of cellular cumulus convection," J. Meteor. Soc. Japan, 45, 251-260.

MEASUREMENTS OF SOLAR RADIATION ABSORPTION IN THE TROPICAL ATMOSPHERE: PRELIMINARY RESULTS

T. H. Vonder Haar, S. K. Cox, and K. J. Hanson

ABSTRACT

The first results from a continuing observational program show that absorption of solar radiation in the lower, moist "clear" tropical troposphere may be greater than would be computed theoretically. Vertical profiles of upward and downward solar energy measured from an aircraft yield warming rates of 0.26° C/hr near local noon in the lowest 200-mb layer but only one-half that value in the regions above.

INTRODUCTION

Solar radiation absorption is an energy source for the atmosphere. The magnitude and importance of this absorption for atmospheric energetics varies with location, season, altitude, and time of day. Particularly in the tropics, with exceedingly large amounts of energy available, solar radiation can provide rapid energy input required to drive atmospheric motions. In addition, selective spatial and vertical absorption may affect local atmospheric conditions and thus, indirectly, the larger scale features.

There have been relatively few measurements of the absorption of solar radiation in the atmosphere. This is in contrast to the number of stations that measure the solar energy arriving at the surface. When coupled with satellite observations of energy reflected space, surface measurements can be used to derive values of absorption in an entire atmospheric column (Fritz et al., 1964; Hanson et al., 1967). Vonder Haar and Hanson (1969) used such a technique to study "total" absorption in the tropics. Based on satellite measurements and data from only two surface stations in the tropics, they noted that, although more solar energy is absorbed in the tropical earth-atmosphere system than previously believed, most of this extra energy is added to that absorbed by the oceans.

While more information on total atmospheric absorption should be obtained, two even more important questions deserve attention: (1) What is the normal range of spatial and vertical absorption ? and (2) How does this energy input directly affect tropical energetics ? Answers to these questions will not only add to our rapidly expanding understanding of tropical meteorology; they are of immediate importance to the developing numerical models that simulate the atmosphere's circulation.

Clouds, of course, are the principal modulators of the incoming solar energy. However, most absorption occurs in atmospheric regions and levels well-saturated with water vapor. In the tropics most of the water vapor is located under the "trade inversion." Thus, in a vastly oversimplified context, studies of solar energy absorption in the tropical atmosphere must be concerned with (1) the magnitude of energy absorbed below the trade inversion and (2) the effect of clouds (either well above the inversion or with tops at the inversion level) in regulating the amount of incident energy which is exposed to low-level absorption.

Improvement of the simplified approach may be attained by including (1) knowledge of absorption in the upper troposphere and (2) absorption and reflection characteristics of common cloud types. The complexity of the problem is increased further by considering turbid atmosphere (at high levels, low levels, or both), spectral and angular effects on absorption, and the effect of multiple scattering between cloud layers and/or the surface.

The total complexity of this atmospheric absorption problem has precluded theoretical and empirical solutions on most space and time scales except the mean annual zonal. Thus, we are unable to assess the effect of direct solar absorption, and its variation, over spatial and temporal scales common to meteorological phenomena in the tropics.

In this paper we present preliminary results of an observational program aimed at improving our understanding of solar energy absorption in the tropical atmosphere. It will follow the simplified context outlined above. It uses aircraft-mounted pyranometers to measure the vertical variation of solar radiation in the atmosphere during typical tropical conditions. It will eventually employ satellite observations of cloud conditions to extrapolate the limited range of aircraft measurements to a broader geographical area. We hope that the observational approach will lay a solid foundation, to which they may be coupled, that will allow accurate parameterization of solar energy absorption in space and time.

THE 1968 BARBADOS PROGRAM

Aside from satellite experiments and some surface measurements of solar energy during the Line Islands experiment, the Wisconsin observational program

for shortwave radiation convergence began with a modest effort during the 1968 Barbados experiment. This program was coordinated by Florida State University with the participation of NCAR and several government and university groups.

Florida State maintained a small surface radiation network on land and from a ship. Wisconsin supervised nocturnal radiometersonde ascents and solar radiation pyranometers on NCAR's Queen Air aircraft. The aircraft flights were primarily in support of low-level island effect research (Garstang and La Seur, 1968), but five special flights obtained measurements of the vertical variation of solar radiation. One of these flights, the first output of our data reduction sequence, will be discussed in this paper.

The Queen Air carried a pair of Kipp and Zohnen (Moll-Gorczynski) pyranometers. Robinson (1966) gives a general description of this thermopile instrument. The pyranometers were mounted diametrically opposed on the tip and bottom of the aircraft fuselage, aft of the wing centerline. Thus the upward mounted instrument measured the downward solar irradiance and vice versa.

The manufacturer provided a calibration relating total solar energy received to voltage output of the pyranometers. This output was accepted by NCAR's ARIS data-logging system and converted to digital form. An ARIS system calibration allowed conversion between incident energy and ARIS digital counts. In addition to pre- and post-flight checks on the system, the pyranometers were calibrated against secondary standards (Eppley pyranometers) during the Barbados experiment. Based on these results we know that both pyranometers yield good relative values of incident solar energy. Only relative values, quite adequate for studying solar radiation divergence, are discussed in these preliminary results. Further study of the calibration records, temperature dependence of the instruments, and the "cosine" effect is underway.

FIRST RESULTS FROM A VERTICAL SOUNDING

A Queen Air flight to measure the vertical variation of solar radiation began at 1459 GMT (1100 local time) on 31 August 1968. As planned with reference to a satellite APT photograph earlier that day, the aircraft located a relatively cloud-free region 100 miles south of Barbados, near 11° N 59° W. The entire sounding was obtained within a 6 × 15 nm rectangle, noted on the ATS-III photograph in Figure 1. An observer on the aircraft reported thin cirrus above the sounding area and small scattered tropical cumulus over the ocean. During the flight, the aircraft measured the vertical temperature and moisture profile shown in Figure 2. Selected Doppler winds are also plotted at the prime measurement levels.

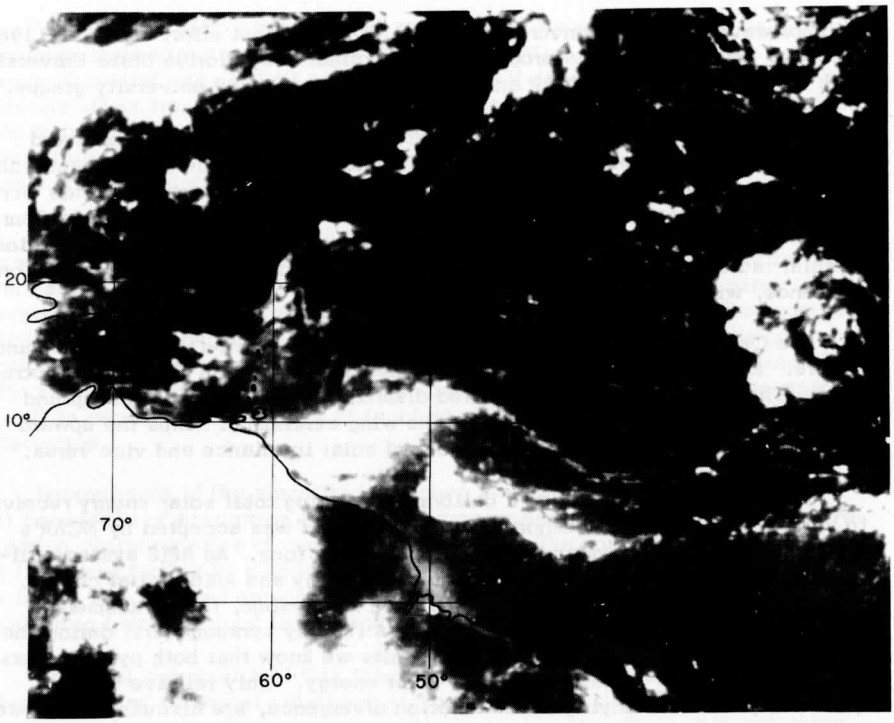

Figure 1. Enlarged portion of ATS-III photograph obtained at 1456Z on 31 August 1968. The arrow notes the area of the aircraft sounding considered in this paper.

These weather observations depict a normal situation in the deep tropics. The moist "trade inversion" extends to approximately 5000 ft (850 mb). The region is nearly saturated with an average mixing ratio of 15 gm/kg. Above the inversion water vapor content falls off rapidly. Forty-two percent of the total atmospheric precipitable water (approximately 3.7 cm) was in the lowest 100-mb layer.

In the upper part of Figure 3, static pressure measured from the aircraft is plotted against time. This shows the sounding pattern of the aircraft, with level flight near 20, 16, 12, 8, 4 and 2 thousand feet and a "surface" run comprising the measurements levels. The figure does not show the ground track that was within the rectangle noted above.

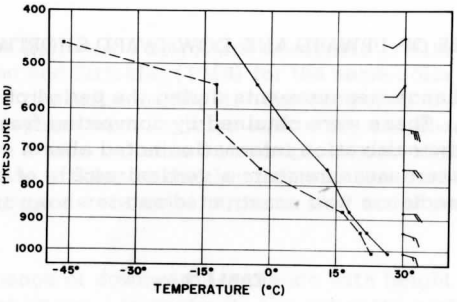

Figure 2. Vertical profiles of temperature and dewpoint, and wind measurements obtained during the aircraft sounding.

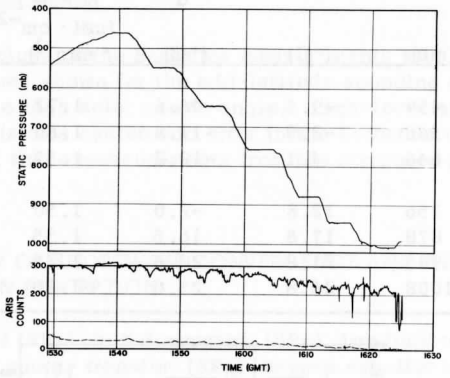

Figure 3. Static pressure at aircraft altitude during the sounding flight (upper portion) and the output of the upward and downward pyranometers (lower portion).

Measurements from the upward and downward pyranometers are shown against the same time scale in Figure 3. Upward irradiance, reflected mostly from the ocean, is very stable throughout the period of record. It decreases slightly as the aircraft reaches lower altitudes and atmospheric back-scattering diminishes. Small fluctuations in the upward trace (and in the measurements of downward irradiance as well) occur as the aircraft departs from straight and level flight. The overall signal from downward irradiance decreases slowly from 20,000 ft to below 8,000 ft and then more rapidly through the moist layer below. Energy drops as large as 10 percent that occur during level flight are caused by the scattered high cirrus clouds reported by the observer.

VERTICAL PROFILES OF UPWARD AND DOWNWARD SHORTWAVE IRRADIANCE

Average irradiance measurements during the period of level flights are shown in Table 1. These were obtained by converting from ARIS counts to irradiance using the calibration information noted above. From the aircraft altimeter and pressure measurements a vertical profile of the upward and downward shortwave irradiance was constructed and is shown in Figure 4.

TABLE 1

"Clear" Solar Radiation Sounding of 31 August 1968

Time (GMT)	P (mb)	T (°C)	T_d (°C)	SR_D (cal · cm^{-2} · min^{-1})	SR_U (cal · cm^{-2} · min^{-1})	H (K ft)
1539-41	459	-9.5	-46.6	1.72	0.17	20
1546-48	546	-2.9	-11.8	1.60	0.14	16
1554-56 (local noon)	646	4.1	-12.2	1.57	0.11	12
1601-04	756	12.8	-2.0	1.50	0.11	8
1609-11	878	17.8	16.5	1.35	0.07	4
1614-16	943	21.8	20.5	1.26	0.05	2
1622-24	1008	26.8	23.0	1.20	0.04	0

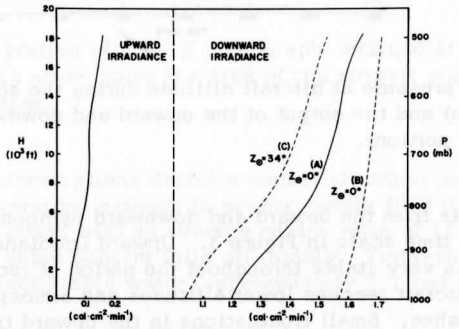

Figure 4. Upward irradiance measured on 31 August 1968 near Barbados and downward irradiance (A) measured on 31 August 1968, (B) computed for the conditions of the measurements near Barbados, and (C) measured on 19 July 1963 in west central U. S. S. R.

The same figure includes a downward irradiance profile computed using the technique of Manabe and Strickler (1964) for the same solar altitude and water vapor distribution of the Barbados flight. The computation was performed for a perfectly clear atmosphere with Rayleigh scattering and absorption due to water vapor only.[1] Figure 4 also includes an example of one of the few available measurements of solar irradiance profiles. It was obtained by Kondratyev and Nikolsky (1968) through a very moist air mass (4.7 cm of precipitable water) at mid-latitudes.

The relative change of downward irradiance with height is very similar for the two measurement cases. In contrast, the computed profile does not show the same strong absorption in the lowest 6,000 to 8,000 feet. This difference deserves further study and requires additional observations. A plausible explanation may be a simple departure from pure gaseous conditions in the lower, significant absorption region.

The absolute values of the Barbados measurements are, as mentioned, uncertain. Lower values shown for the mid-latitude sounding are due to the reduced insolation at a high solar zenith angle. High-level attenuation of solar energy by thin clouds or a systematic error in the Barbados data may account for the difference of these measurements from the computed profile above the moist layer.

VERTICAL VARIATION OF SHORTWAVE CONVERGENCE AND HEATING RATES DUE TO SOLAR RADIATION ABSORPTION

From the upward (SR_U) and downward (SR_D) irradiance measurements we derive the net solar energy transfer (SR_N) across specific levels in the atmosphere, P:

$$SR_N(P) = SR_D(P) - SR_U(P) \qquad (1)$$

and the net convergence of solar radiation $C(\Delta p)$ for 100-mb layers:

$$E(\Delta p) = SR_N(P) - SR_N(P - 100) \qquad (2)$$

Table 2 contains these data from the 31 August 1968 Barbados flight. The sounding lacks high vertical resolution but shows a simple two-layer convergence pattern.

---

[1] Manabe and Strickler (1964) and also Yamamoto (1962) show that water vapor accounts for almost 90 percent of the absorption of solar radiation below 500 mb in a clear atmosphere.

TABLE 2

Results from 31 August 1968 Flight

P (mb)	Δp	$SR_N(P)$ (cal·cm^{-2}·min^{-1})	E(Δp) (cal·cm^{-2}·min^{-1})	dT/dt (°C/hr)
500		1.50		
	500 - 600		0.05	0.13
600		1.45		
	600 - 700		0.05	0.13
700		1.40		
	700 - 800		0.05	0.13
800		1.35		
	800 - 900		0.10	0.26
900		1.25		
	900 - 1000		0.10	0.26
1000		1.15		
	800 - 1000		0.20	0.26
	500 - 1000		0.35	0.18

Instantaneous heating rates, $\Delta T/\Delta t$, may be computed from the $E(\Delta p)$ values by:

$$\frac{\Delta T}{\Delta t} = \frac{g \cdot E(\Delta p)}{p \cdot c_p} \qquad (3)$$

Values of $\Delta T/\Delta t$ in degrees Centigrade per hour, valid for the sounding time near local noon, are shown in Table 2 for various atmospheric layers. Warming is twice as large in the moist layer (1000 - 800 mb) than in the layers above (800 - 500 mb). From these preliminary results, it appears that absorption of solar radiation in clear tropical regions may cause layer destabilization of at least 0.1°C/hr per kilometer across the trade inversion level.

Equivalent 24-hour warming rates are useful to compare with other energy budget parameters. Assuming that the relative vertical variation of shortwave convergence is maintained over nearly all the daylight hours and accounting for reduced insolation at lower sun angles, 24-hour warming rates for this Barbados sounding are: 1000 - 8000 mb, 1.0°C/day; 800 - 500 mb, 0.5°C/day; 100 - 500 mb, 0.7°C/day. Allowing absorption above 500 mb in the troposphere to equal about 10 percent of that below the level yields a tropospheric mean warming rate (1000 - 100 mb) of 0.4°C/day for the case studied.

This is equivalent to the absorption of 175 cal per cm^2 of a clear column during the daytime hours. Total daily insolation at 10° N on 31 August is 915 cal · cm^{-2}; thus 19 percent of the incident solar energy was absorbed in the troposphere. Vonder Haar and Hanson (1969) used satellite and surface measurements to estimate that 14 percent is absorbed in this latitude zone on a mean annual basis; earlier studies based on climatology estimated 15 percent annual absorption with average cloudiness.

SUMMARY

This paper contains only preliminary results of an observational program now underway. However, based on only one aircraft sounding, the vertical variation of solar radiation absorption appears to differ significantly in the lower, moist troposphere from a rate computed with a contemporary technique. More measurements will prove or disprove this preliminary result and make possible a proper study of the effects of solar energy absorption on the tropical atmosphere. Both clear and cloudy cases must be studied and the solar radiation must be considered simultaneously with other energy transfer processes.

The results of the observation program will be coupled with theory to provide a proper parameterization of solar energy absorption. The field program continues near Barbados with improved pyranometers on several aircraft as part of BOMEX.

ACKNOWLEDGMENTS

Dr. Ed Zipser and Mr. Cleon Biter of NCAR, as well as other flight facility personnel, made the aircraft soundings possible.

REFERENCES

Fritz, S., P. Rao, and M. Weinstein, 1964: "Satellite measurements of reflected solar energy and the energy received at the ground," J. Atmos. Sci., 21: 2, 141-151.

Garstang, M., and N. La Seur, 1968: "The 1968 Barbados experiment," Bull. Am. Meteor. Soc., 49: 6, 627-635.

Hanson, K., T. Vonder Haar, and V. Suomi, 1967: "Reflection of sunlight to space and absorption by the earth and atmosphere over the United States during Spring 1962," Mon. Weather Rev., 95: 6, 354-361.

Kondratyev, K., and G. Nikolsky, 1968: "Direct solar radiation and aerosol structure of the atmosphere from balloon measurements in the period of IQSY," Sveriges Met. arch Hydrol. Inst. Meddel.,Ser. B, No. 28.

Manabe, S., and R. Strickler, 1964: "Thermal equilibrium of the atmosphere with a convective adjustment," J. Atmos. Sci., 21:4, 361-385.

Robinson, N. (ed.), 1966: Solar Radiation, Elsevier Publ. Co., New York, 255-261.

Vonder Haar, T., and K. Hanson, 1969: "Absorption of solar radiation in tropical regions" (to be published in J. Atmos. Sci.).

Yamamoto, G., 1962: "Direct absorption of solar radiation by atmospheric water vapor, carbon dioxide and molecular oxygen," J. Atmos. Sci., 19: 2, 182-188.

PROTOTYPE ALIGNMENT JIG FOR USE IN REGISTERING ATS PICTURES

T. Schwalenberg

INTRODUCTION

One of the biggest problems associated with using the cloud cover pictures generated by the ATS-I and ATS-III satellites is to align or register the pictures. For any use requiring comparative measurement from one picture to another, such as for wind measurement, cloud deformation measurement, or the production of cloud cover movies, it is absolutely imperative that the pictures be registered. To date, the most effective means of alignment consisted in (1) securing transparencies of the pictures to be registered, (2) superimposing the pictures on a light box, and (3) moving the pictures by hand until the visible land masses appeared to superimpose. It is the purpose of this document to describe a "system," based upon these techniques which will allow a relatively untrained operator to align pictures to a high degree of accuracy.

SYSTEM DESCRIPTION

The system design of the alignment jig is based upon the following observations: (1) The need for corrections to bring the two pictures into registration is due to the satellite's spin axis not being parallel to the spin axis of the earth and to the drift of the satellite; (2) The necessary corrections are in the form of three independent movements—two orthogonal lateral motions and a rotation about the subsatellite point; and (3) The human perception is more adept at sensing movement than it is at superimposing two edges. The alignment jig consists of five subsystems as shown in Figure 1.

MOVABLE PLATFORM

The movable platform allows the operator to remotely move the picture to be aligned relative to the reference picture. The platform allows for the necessary motions—lateral and rotation—to be executed smoothly and precisely as well as completely independently. This means that the operator need only correct one error at a time.

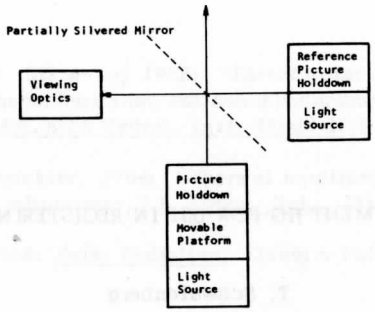

Figure 1. ATS alignment jig block diagram.

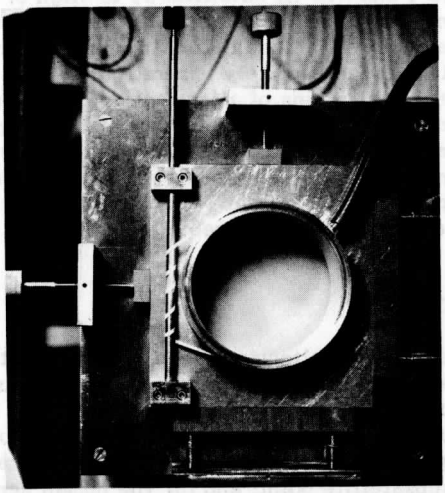

Figure 2. Prototype of movable platform.

A photograph of the prototype movable platform is shown in Figure 2. This subsystem is essentially a ring, which holds the picture and allows for the rotational movement, mounted on a flat base, which allows for the two lateral movements. The ring is belt driven, and the base is spring loaded to insure zero backlash as well as smooth operation.

In this prototype system, the picture is held to the ring utilizing a vacuum technique. The vacuum is useful for small pictures, but it allows larger pictures to "sag" in the center and thus adds distortions to the system. The

operational alignment jig will have to handle pictures with a 10-inch-diameter earth, and, for this system, the picture will be sandwiched between two pieces of glass resting on the movable platform.

REFERENCE PICTURE MOUNT

The reference picture must be mounted at right angles to the movable picture, because of requirements imposed by the superposition optics. The reference picture is sandwiched between two pieces of plate glass to insure flatness.

In the operational system, the reference picture will be punched to provide a positional reference, and these punched holes will mate with pegs which will be part of the reference picture mount. The operational system is designed so as to punch the pictures once they are aligned. By punching the pictures, the alignment is retained for all future use of the picture. The operational system is also designed so that when viewing the two pictures through the superposition optics, the pegs which hold the reference picture and the dies which punch the pictures will also superimpose. This insures that any previously punched picture can be used as a reference and that the resulting punched pictures will be compatible with all other punched pictures made with the same reference image.

SUPERPOSITION OPTICS

A partially silvered mirror is used to superimpose the two images. (See Figure 3.) By using the mirror instead of lenses, all the problems associated with lenses, such as distortion, limited resolution, focus, and magnification adjustment, have been eliminated. Consequently, the system is easier to align and keep in alignment. Because the human is involved, it is not absolutely necessary that the mirror be optically flat or uniformly plated. For the prototype, we made our own mirror using plate glass and the technique of vacuum deposition of aluminum with very satisfactory results.

LIGHT SOURCE

The light source is a very important part of the alignment jig because it allows the operator to use his perception of motion to see misalignment. If both pictures were illuminated continuously, the operator would have to judge alignment by looking for the best fit of land mass edges and features. However, the pictures are not illuminated continuously nor ever simultaneously. The light source consists of two Xenon flash lamps—one for each picture—which are alternately flashed 20 times per second. Because of the high flash rate, the pictures appear to be continuously illuminated. However, because the

Scanner's note:

This page is blank.

APPENDIX

List of Serial Numbers By Which Figures Can Be Ordered

Following is a list of figures (titles abbreviated) appearing in this report and the corresponding photo serial number. Copies of each photograph are available for purchase at a cost of one dollar ($1.00) per print from The University of Wisconsin, Space Science and Engineering Center, Madison, Wisconsin 53706. Orders should cite the appropriate serial numbers.

Page	Figure	Serial Number
	D. Sikdar and V. Suomi	
3	1. Schematic diagram for the proposed convection model	87422-C-1
10	2. Schematic diagram of a convective complex	87423-C-1
10	3. Plot of corrected brightness values	203-A
12	4. Plot of digital signal across a convective ensemble	203-B
13	5. ATS-I photograph of April 19, 1967	87427-C-1
13	6. Enlargement of cloud field around Palmyra	87426-C-1
14	7. Enlargement of cloud field at 10° S on the ITCZ	87432-C-1
	8. ATS digital displays corresponding to Figure 6	
15	a	87436-C-1
16	b	87429-C-1
17	c	87437-C-1
	9. ATS digital displays corresponding to Figure 7	
18	a	87435-C-1
19	b	87433-C-1
20	c	87431-C-1
25	10. Mean upper air sounding	87428-C-1
26	11. Radar pictures around Palmyra	
	a	87434-C-1
	b	87430-C-1
	c	87425-C-1
27	12. Mean profile of heat content of air	87424-C-1
28	13. Plot of mass upward flux	(None)

T. Vonder Haar

E. Remsberg and J. Weinman

J. Bennett and J. Young